WIRELESS TAGGING AND ACTUATION WITH SHAPED MAGNETOELASTIC TRANSDUCERS

by

Jun Tang

A dissertation submitted in partial fulfillment
of the requirements for the degree of
Doctor Philosophy
(Mechanical Engineering)
in the University of Michigan
2014

Doctoral Committee:

Professor Yogesh B. Gianchandani, Chair
Assistant Research Scientist Scott R. Green
Professor Khalil Najafi
Associate Professor Kenn Oldham

ACKNOWLEDGMENTS

The work described by this dissertation was funded in part by the University of Michigan, Defense Advanced Research Projects Agency (DARPA). Samples for this work were provided by Metglas, Inc. The fabrication was done in Lurie Nano Fabrication Facility (LNF) operated by the Solid-State Electronics Laboratory (SSEL) and the University of Michigan. I appreciate the help from all staff members.

I would like to thank the committee members for their constructive suggestions on this research and dissertation. I was benefited from envision of the potential applications of this work by Prof. Najafi. I also gained deeper understanding of the advantage and disadvantage of this work under the guidance from Prof. Oldham. Dr. Scott Green, who is more like a co-advisor, always provides precious suggestions in all aspects, from the concept to the experiments. He also offered a lot of help in completion of this dissertation. Professor Yogesh Gianchandani, as Chair of my committee and the advisor of my doctoral research, provided me well-defined projects and profound research resource. Along my four years of study, he can always guide me with a clear direction and efficient approaches, which leads to the achievements in this work. Besides the research, he also taught me to put family at the first place.

I would like to thank my group members, lab mates, 2001 office colleges. Thank you all for the support in both study and personal life. Xin Luo, a group member and close friend, shared all the relaxed and stressed time during these four years study. Venkatram Pepakayala, was always here for discussion on the magnetoelastic related

theory and simulations. I always enjoy the collaboration moment with Jiangfeng Wu, Jihun Choi, Jinhong Qu on magnetoelastic tag, and DARPA projects.

I was also very grateful about the support from my family. My grandpa, who suffered from diabetes, is always proud of any small achievement I obtained. I am lucky to be in a family who never gave me pressure on my study. I believe that is one reason I can as far as I want to explore my potential. My parents always supported me mentally and financially. I cannot finish any of this without their support.

Finally, I am very lucky to have Yuayuan Wang as my wife, who supports me all the time. She took the most responsibility of the family while I could not always be there for her. I am looking forward to enjoy the life with her and coming baby together in the future.

TABLE OF CONTENTS

LIST OF FIGURES

LIST OF TABLES

Table

LIST OF APPENDICES

Appendix

LIST OF SYMBOLS

F_x – tangential force

F_z – normal force

ε – permittivity

a – length

b – width

V – voltage

z – gap between two plates of a capacitor

T – stress vector

c – stiffness vector

s – strain vector

E – electric field

D – electric displacement

u_s – displacement of a standing wave

A – amplitude

k – mode shape factor

ω – angular frequency

t – time

u_t – displacement of a traveling wave

λ – wave length

f – frequency

m – mass

ρ_s – density of the sensor

ρ_m – density of the surrounding medium

η – viscosity of the surrounding medium

$\vec{\sigma}$– stress vector

[C] – stiffness matrix

$\vec{\varepsilon}$ – strain vector

[d] – magnetostrictivity matrix

μ_0 – permeability of free space

μ_r – relative permeability

$\vec{H}$ – magnetic field strength vector

$\vec{B}$ – magnetic flux density vector

I – moment of inertia

τ – torque

α – angular acceleration

r_1 – inner radius of the rotor

r_2 – outer radius of the rotor

θ – angle

Δf – frequency difference of two mode shapes

Chapter 1

Introduction

More and more novel materials with unique material properties have been utilized for microelectromechanical systems (MEMS). Among these materials, magnetoelastic material is of interest because it builds a bridge between the magnetic field and the stress and the strain of the material. Magnetoelastic material exhibits strain under an applied magnetic field, while the stress also generates a magnetic flux simultaneously. This bi-directional coupling is especially preferred for a wireless microsystem, which is a very attractive topic because of the potential biomedical, structural monitoring, and remote monitoring applications. This work explores the possibility of utilizing magnetoelastic material for miniature wireless actuators and sensors.

Rotary micromotors are a classic type of MEMS actuators researched since the 1980s, from which many applications would benefit. Furthermore, such motors are a good demonstration of the capability of a material to be used as an actuator because the rotary motor is typically a relatively complex device requiring precise structural design and dimensional control to operate. Thus, magnetoelastic rotary motors are studied in this work. The advantages of magnetoelastic rotary motors include wireless actuation, high payload carrying capability, simple passive architectures, and so on. The wireless and passive properties of this magnetoelastic motors allow simplification of the design by avoiding integration of the control electrodes and circuits alongside the device. This simplification provides enough space for integration of a capacitive sensor for real time speed measurements. With this advantage, one application is demonstrated by utilizing a

magnetoelastic rotary motor for providing rotational stimulus for *in situ* calibration of a gyroscope.

Magnetoelastic materials are also attractive for sensing or tagging systems. One of the most commercially successful applications involves utilizing magnetoelastic resonators as anti-theft tags; this application takes specific advantage of the low cost and good resonant performance of the material. Despite the great progresses made in this field, miniaturization of the magnetoelastic tags remains a challenge due to the loss of signal strength as the size of the tag decreases. Another effort for this work is devoted to making advances on the challenges of magnetoelastic tag miniaturization.

In section 1.1, the motivations for developing micromotors are described and different types of micromotor are compared. In section 1.2, the motivation for a tagging system is presented, as well as the advantages and disadvantages of different types of tags. Section 1.3 describes the previous work in magnetoelastic sensors and actuators. Section 1.4 gives the goals and structure of this dissertation.

1.1 Motivation and Previous Efforts in Micromotors

1.1.1 Motivation for Micromotors

Chip-scale rotary motors have been of interest since the 1980s. With the ongoing progress in microsystem miniaturization, there are a number of emerging microsystem applications that would benefit from micromotors including medical, laboratory equipment, microbotics, automation, optics, photonics, aerospace, defense, and so on. For example, endoscopes equipped with a video camera, light source and remotely controlled surgical tools are likely to conduct minimally-invasive surgeries within human body. This would benefit patients by reducing trauma and recovery time. However, a breakthrough in this field would be difficult without development of 'practical'

micromotors [Wat10]. Similar technology is potentially able to conduct in-situ monitoring and repair of large-scale complex machines such as engines, rather than requiring disassembling. Another example of micromotor application involves actuation of optical elements in microsystems for communication or microanalytical applications.

Among various applications, one practical and worthwhile effort is to develop a rotary stage for in-situ calibration of inertial sensors by providing a desired physical stimulus, as shown in Fig. 1-1. Inertial sensors, such as accelerometers and MEMS gyros, are usually integrated into electronic systems. Such systems are becoming more and more commonplace in our daily lives, including navigation in cell phones, and motion sensing for video games. These systems also play crucial roles in military applications. For example, MEMS-based gyros can offer precision navigation aids that are essential for aviation and smart munitions, as well as in autonomous land vehicles, robotics, personal locators, and so on. Although focusing on different applications, these systems all benefit from long-term accuracy. However, for inertial sensors, the bias and scale factor drift due to aging, particle buildup, and temperature. These errors are typically more troublesome in MEMS inertial sensors in comparison to macro-scale sensors. Calibration typically requires sensors to be taken out of service or be replaced. On-chip *in situ* calibration potentially provides a more efficient solution. For example, miniature rotary stages can provide sensors with a desired physical stimulus for on-chip calibration (i.e., rotation or displacement, angular rate or velocity, and acceleration).

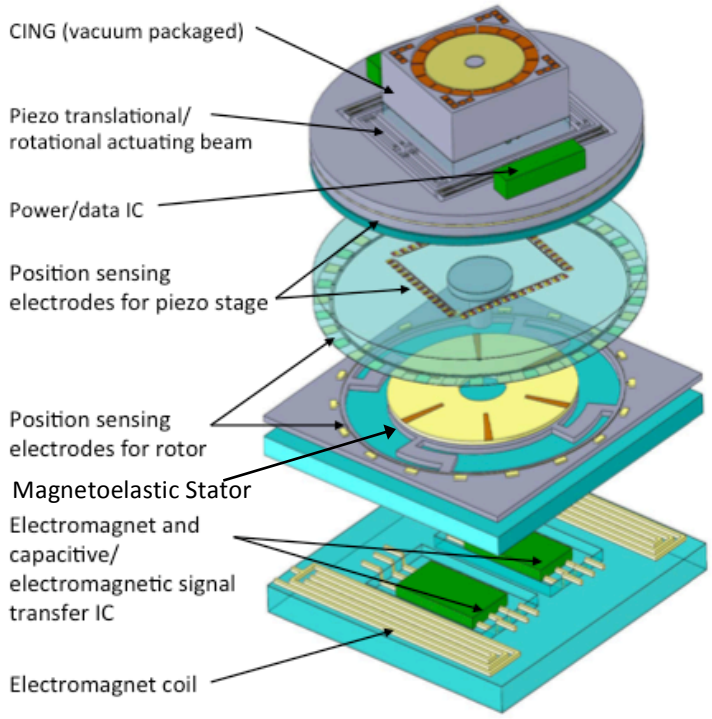

Fig. 1-1: Potential application of magnetoelastic motor in an *in-situ* micro-gyroscope calibration system. The motor is utilized to generate accurate stimulus, such as rotation rate or acceleration. [Najafi, Private Communication, May 2012]

Another motivation for developing a magnetoelastic rotary motor is wireless actuation. The main advantage of wireless actuation is the capability of operation in an environment that makes integration of power supply a challenge, such as minimally invasive surgery as mentioned previously. Other advantages include simplified device architecture and reduced total cost through reutilization of an external driving setup for multiple devices.

Although there are promising applications, micromotors still require profound development and demonstration in performance – such as torque, speed, precision, payload and miniaturization – to meet practical requirements. Thus, there have been efforts on miniaturization of motors and development of different actuation methods.

1.1.2 Efforts on Developing Different Types of Miniature Motors

Rotary motor actuation methods include electrostatic, electromagnetic, piezoelectric, and so on. In this section, characteristics of three major miniature motor technologies, as just mentioned, are described in aspects of history, working principle, category, advantage and disadvantage, and potential performance improvement. Then, brief discussions on other less studied motor technologies, such as electrothermal, optical, and Marangoni-flow-driven, are given.

1.1.2.1 Electrostatic Motors

In the 1750s, the first electrostatic motors were developed by Benjamin Franklin and Andrew Gordon. These motors utilize the attraction and repulsion of electric charge to drive the rotor. For example, the electrostatic force between two parallel plate capacitor with opposite charges can be expressed as (the fringe effect of the capacitor is not considered here and applied voltage is smaller than breakdown voltage):

$$F_x = -\frac{1}{2}\varepsilon a\frac{V^2}{z} \tag{1-1}$$

$$F_z = -\frac{1}{2}\varepsilon ab\frac{V^2}{z^2} \tag{1-2}$$

where F_x and F_z are the tangential force and normal force, respectively; ε is permittivity; a, b, are length and width, and z is the gap between two plates. The equations show that the electrostatic force is proportional to a/z, b/z and V^2. In macro world, a/z and b/z is typically less than 10^1 and motors require large force. Consequently, electrostatic motors in large scales typically require a high voltage power supply, which has limited their application. However, in MEMS systems, a/z and b/z can be as high as

10^3, and required driving forces can be as low as 10^{-6} Newton. This allows the operation voltage to be reduced to below 100 V and has drawn attention of researchers from both academic and industrial areas. Electrostatic micromotors were first considered in the MEMS field in 1987 [Tri87] and fabricated and characterized by Tai et al [Tai88, Fan88], and Mehregany et al [Meh90]. Electrostatic micromotors are considered as one of the milestones in MEMS history and there have been many efforts on performance improvement since then.

Broadly speaking, there are two types of electrostatic micromotors: VCMs (variable-capacitance motors) and electric induction motors. VCMs are synchronous systems and the rotors are driven by torque generated by spatial misalignment of electrodes on the stator and rotor. Typically, the stators and rotors are patterned into a structure with periodic electrode with a fixed spacing between them. The electrodes on the stator are connected in several groups and are typically driven by a three-phase or six-phase signal. The torque is a function of rotor position. VCMs can be further classified as side-drive, top-drive and bottom-drive with respect to positions of driving electrodes. Most VCMs are side-drive because the top-drive suffers from a "rotor clamping" phenomenon. Recently, bottom-drive has been developed that is based on a miniature ball-bearing system [Gha08].

Electric induction motors are asynchronous systems. The stators are typically patterned with an array of radial electrodes that are excited with ac voltages to create a traveling wave of potential around the stator surface. The rotors are coated with a slightly conducting layer, in which image charges are induced by electric potential on the stators. The image charges follow the travelling wave of potential on the stators, but with a lag behind the excitation due to the slightly conductive property of the rotor.

Tangential electric fields are generated between the rotors and stators, which drive rotors tangentially. This type of motors is intensively studied in [Bar89, Liv04, Nag05].

Generally speaking, electrostatic micromotors operate at very high rotation rate and the surface micromachining processes are compatible with IC processes. The disadvantages include low torque and small payload. However, there have been many efforts on increasing the torque and payload capacity by utilizing different bearing systems. For example, Ghalichechian et al. use miniature ball-bearings to reduce the friction and allow a bottom drive configuration that increases the effective area of capacitors. A 5.6 μN·m torque is achieved while the rotation rate is still maintained as high as 517 rpm [Gha08]. The electric induction motor, developed by Nagle et al., has a torque of 3.5 μN·m at rotation of 55000 rpm [Nag05]. By utilizing liquid a ring bearing, the latest electrostatically driven rotary motor can carry a 700 mg payload [Sun12].

1.1.2.2 Electromagnetic Motors

Macro-scale electromagnetic motors are very mature but efforts toward their miniaturization have resulted in landmark accomplishments for the microsystems research community. H. Guckel et al. demonstrated a first functional planar electromagnetic micromotor [Guc91, Guc93]. H. Ahn et al. made a planar electromagnetic micromotor with fully integrated stator and coils [Ahn93]. In 2006, permanent magnets were utilized in the electromagnetic micromotors to improve performance on torque and rotation rate [Ach06, Arn06]. Other latest electromagnetic micromotors reports include [Mer11, Cha12].

In general, the main types of electromagnetic motors are DC and AC motors. In MEMS, according to working principles, these motors can be generally categorized as variable reluctance magnetic (VRM) motors and magnetic induction motors. VRMs

[Guc93, Ahn93, Mer11] are very similar to that of electrostatic VCMs. VRMs are also synchronous systems and the rotors are driven by torque generated by spatial misalignment of salient poles on the stators and rotors. Salient poles are typically arranged in one or several sets with different phases. When the rotors rotate and align with the excited stator poles to minimize the reluctance, the excited phase is switched off and the next phase is switched on to maintain continuous rotation. Instead of electrostatic force, magnetic force is used in this case.

Magnetic induction motors utilize a similar driving mechanism as that of electric induction micromotors [Arn06, Kos06, Cro06]. Instead, the stators of magnetic induction motors have symmetrically-patterned permanent magnetic cores that are surrounded by exciting planar coils. By exciting the coils in different phases, a travelling magnetic wave can be generated between stators and rotors, and an eddy current is induced in the rotors. The eddy current interacts with the travelling magnetic wave, and generates an attractive force between rotors and stators, which drives the rotors tangentially.

More research has been focused on electrostatic micromotors compared to that on electromagnetic micromotors, partly because fabrication technologies for coils and usage of permanent magnets are not well known in the traditional microfabrication field. Regardless, current results sill showed very good performance on rotation rate (up to 200 krpm) and torque (most in 1-100 μN·m scale). If developments on integrating fabrication processes continually occur, electromagnetic micromotors are one of the most promising technologies.

1.1.2.3 Piezoelectric Motors

Another successful and well-studied technology is piezoelectric motors. The first practical ultrasonic piezoelectric motor was proposed by Barth of IBM in 1973 [Bar73].

Since the 1980s, along with improvements on the fabrication and assembling technologies on piezoelectric materials, these motors have always been one of most interesting topic in the MEMS community. Every few of years, there is a review paper summarizing the latest developments in this area [Uch98, Mor03, Wat09]. The basic fundamental actuation behind these complicated structures is illustrated in constitutive equations (stress-charge form) [IEEE88] for piezoelectric materials:

$$\begin{aligned} T_{ij} &= c_{ijkl}^{E} S_{kl} - e_{kij} E_k, \\ D_i &= e_{ikl} S_{kl} + \varepsilon_{ij}^{S} E_k, \end{aligned} \tag{1-3}$$

where T is mechanical stress; c is the stiffness of the material measured at zero electric field; S is the mechanical strain; e is the piezoelectric constants; E is the electric field; D is the electric displacement; and ε is the dielectric permittivity of the material measured at zero mechanical stress. It can be seen from this equation that piezoelectric rotary motors – such as ultrasonic motors – typically transfer electric energy to mechanical vibration energy that drives rotor rotation. From a vibration characteristic viewpoint, piezoelectric motors can be categorized as standing-wave type and traveling-wave type.

The standing-wave type motors typically utilize the elliptical motion of tips in the stator to drive the rotor. A simple 1-D standing wave is expressed by:

$$u_s(x,t) = A \cos kx \cos \omega t \tag{1-4}$$

where u_s is the displacement at location x; A is the amplitude; k is determined by the mode shape; ω is the frequency and t is the time. The stators are designed to ensure the elliptical motion of the stator-rotor contacting tips. For example, as shown in Fig. 1-2 (a), Iino *et al* achieved elliptical motion of teeth by arranging them offset from the antinodes of a ring-shaped disk [Iin00]. Suzuki *et al* developed a "windmill" stator so

that the tips of three flexible cantilevers move elliptically (Fig. 1-2 (b)) [Suz00]. Other approaches such as utilizing elastic fins [Dub98] and a pre-twisted beam [Waj08] have also been studied.

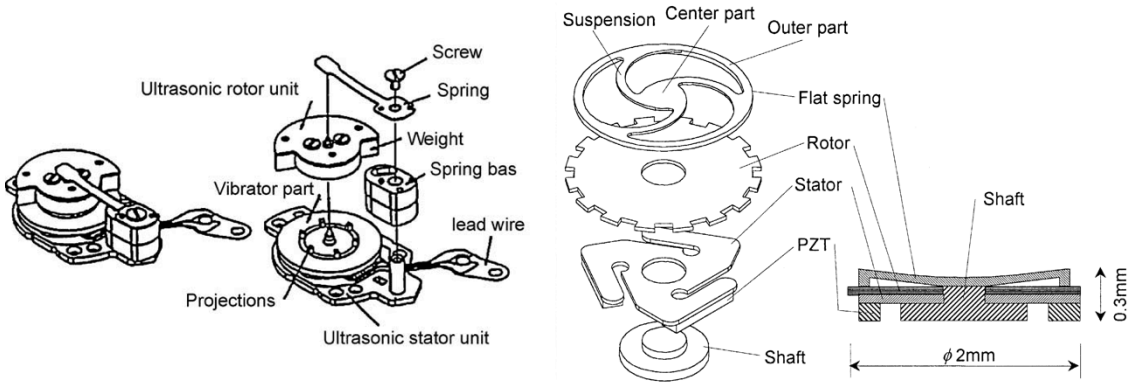

(a) (b)

Fig. 1-2: Examples of standing wave piezoelectric miniature motors. (a) A disc-shaped stator with projections located offset from antinodes drives rotor. The large torque allows practical application in a commercial watch [Iin00]. (b) A "windmill" stator design facilitates elliptical motion of the tip that drives rotor rotating [Suz00].

By comparison, the traveling wave type motors typically utilize the elliptical motion of every point on the surface of the stator, rather than using only elliptical motion of tips on the stators for the standing wave type. A simple 1-D traveling wave is expressed by:

$$u_t(x,t) = A\cos(kx - \omega t) \tag{1-5}$$

$$u_t(x,t) = A\cos kx\cos\omega t + A\cos(kx - \pi/2)\cos(\omega t - \pi/2) \tag{1-6}$$

where the parameters have the same definition as the standing wave equation. As shown in the equation, the traveling wave is combined by two standing waves with 90˚ phase difference both in space and time. The first miniature traveling wave ultrasonic motor is reported by Sashida in 1983 [Sas85]. The traveling elastic wave is induced by a thin piezoelectric ring that is divided into 16 positively and negatively poled regions. The positively and negatively poled regions provide 90˚ phase difference in time for two standing waves. 90˚ phase difference in space is achieved by locating reversely poled

piezoelectric material regions with $\lambda/2$ distance from each other (Fig. 1-3 (a)). This famous and successful design has still been studied lately in [Rud12]. A similar idea has been utilized in a cylindrical structure in order to maintain the performance while decreasing the diameter of the motor [Mor00, Koc02, Kan06] (Fig. 1-3 (b)). After noticing that the traveling wave is limited in vibration amplitude of the stator, Kaajakari used a piezoelectric plate to generate a traveling wave of air between the rotor and the stator [Kaa07].

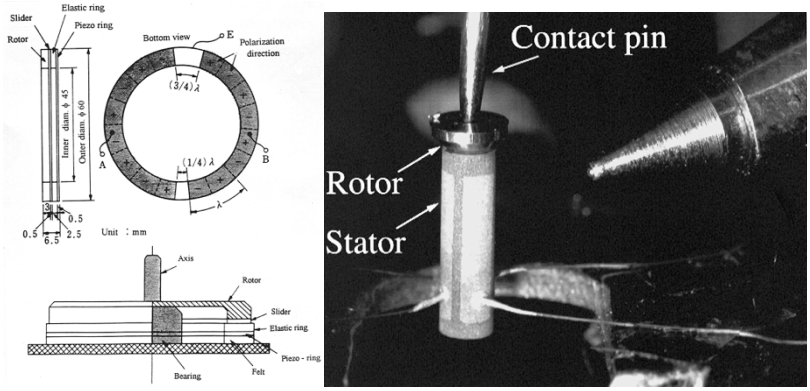

(a) (b)

Fig. 1-3: Examples of travelling wave piezoelectric miniature motors. (a) A disc-shaped stator driven by two AC signals with 90˚ phase difference. Such designs are utilized in commercial digital cameras for lens auto focus [Rud12]. b) Similar designs are studied in cylindrical stators to decrease the diameter [Mor00].

Among all the motor technologies, piezoelectric motors have outstanding performance on torque. Thus, most practical motors applications prefer to use piezoelectric actuation. The standing-wave motors have been used in commercialized watches [Iin00] and the traveling-wave motors have been utilized in digital cameras for lens auto focusing [Uch98]. Compare to traveling-wave type, the standing-wave type reduces the cost and the complexity of circuit design. Traveling-wave type typically has advantage on bi-directional rotation and payload ability. Overall, piezoelectric motors have been the most successful miniature motors in practical applications.

1.1.2.4 Other Types of Micromotors

Besides the three types of motor described above, different actuation methods have been reported. Thermally actuated rotary motors can be used for applications requiring large forces [Par01]. Han et al reported a light-powered micromotor [Han10]. A Marangoni-flow-driven micromotor allows operation in liquid medium [Hen12]. A variety of actuation methods offer more options for different motor applications.

1.2 Motivation and Previous Efforts in Electronic Surveillance Articles

One of the most successful applications utilizes magnetoelastic tags for electronic article surveillance (EAS) systems [Kim96, Her03]. A typical magnetoelastic EAS system – firstly patented in [And85] – consists of a magnetoelastic tag, power source, transmitter, receiver and an alarm (Fig. 1-4 (a)). A simple magnetoelastic tag design should at least include a magnetoelastic resonator, a magnetizable sheet that provides a DC magnetic field, and a package that allows the vibration of the resonator (Fig. 1-4 (b)).

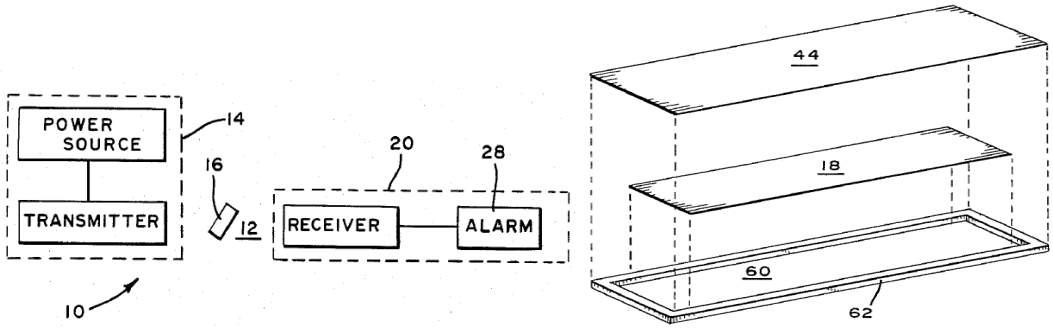

(a) (b)

Fig. 1-4 (a) A typical magnetoelastic EAS tagging system consists of a power source, a transmitter, a magnetoelastic tag, a receiver and an alarm. (b) The basic mangetoelastic tag includes a magnetoelastic resonator (as marked as 18), a magnetic sheet (as marked as 60), and the packages (as marked as 44 and 62) providing a space for its vibration [And85].

There are three types of EAS tags commonly used for theft deterrence in libraries, supermarkets, retail stores, etc. One type of EAS tag, the radiofrequency (RF) label,

consists of an inductor-capacitor (LC) tank circuit that absorbs an RF signal at its resonant frequency [Mon88, Cha92]. The presence of an RF label can be detected by measuring the reduction in the received signal while sweeping the frequency of the transmitted signal near the resonant frequency of the LC circuit.

Another type of EAS tag, the magneto-harmonic tag, consists of a ferromagnetic material strip with moderate magnetic permeability, and another ferromagnetic strip that has higher coercivity. When interrogated by an AC magnetic field that spans a predetermined range of frequencies, the tag generates a harmonic signal that is then detected by a receive coil, indicating the presence of the tag [Bla90, Bru92].

The third type of EAS tag, the magnetoelastic or acousto-magnetic tag, utilizes a magnetoelastic strip, a hard ferromagnetic strip to provide magnetic bias, and a package to provide space for vibration [And85, Her00]. In acousto-magnetic systems, magnetoelastic strips oscillate mechanically at a resonant frequency when interrogated, and generate an AC magnetic flux that can be detected wirelessly by a receive coil. Amongst the three types of EAS tags, magnetoelastic tags provide an attractive price/performance ratio, and hence have gained wide commercial acceptance. In addition, magnetoelastic resonators – with appropriate design and packaging – can be used for a variety of sensing applications.

Despite great improvements in signal strength and detection range provided by advances in material properties and detection approaches, the miniaturization of magnetoelastic tags remains a challenge. Challenges resulting from miniaturization include signal loss and compromises in dimensional tolerances [Her02, Fab06]. Many applications would benefit from miniaturization of magnetoelastic tags. For example, a much smaller magnetoelastic tag would be less conspicuous for anti-theft systems. Miniaturized tags could be helpful in the management of inventories. New applications

can be envisioned, including some in medical sectors. For example, tagging of surgical supplies and instruments could reduce procedural errors and allow tracking of items. Tags with different resonant signatures would provide more granularity. Miniaturization also brings other benefits, such as reducing material costs and increasing the resonant frequency. Higher resonant frequencies generally permit smaller antenna dimensions, and can also be helpful in evading 1/f noise in interface electronics.

The main concerns for miniaturization include diminished signal and fabrication challenges. Signal strength is directly related to the effective volume of the magnetoelastic material. The typical commercial magnetoelastic tags operating at 58 kHz are about 38 mm long, 12.7 mm or 6 mm wide and 27 μm thick [And85]. Smaller tags operating at 120 kHz, with adequate signal strength for commercial use, still have a length of about 20 mm and width of 6 mm, as shown in Fig. 1-5 [Fab06]. These magnetoelastic tags are usually strips or ribbons and the length-to-width ratio is normally larger than 3:1.

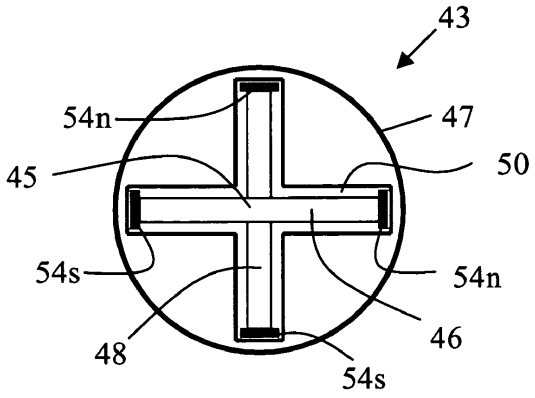

Fig. 1-5: A miniature magnetoelastic tag that includes two magnetoelastic strip resonators with size of 20 mm x 6 mm x 26 μm (45 and 48), four magnets (54s and 54n), and a package. Two magnetoelastic resonators are arranged perpendicular to each other to reduce the sensitivity to the orientation of the interrogation field [Fab06].

1.3 Magnetoelastic Sensors and Actuators

Magnetoelastic coupling represents the interaction between the material conditions of strain, stress and magnetization. Magnetoelastic materials exhibit strains under external magnetic fields due to the field-directed rotation and alignment of tightly-coupled, elongated structural and magnetic domains in the materials (magnetostrictive effect). The strain induces stress in the material, which, in turn, alters the magnetization (inverse magnetostrictive effect or Villari effect). When excited with oscillatory magnetic fields, these two simultaneously existing effects make magnetoelastic materials attractive for wireless resonant sensing. Further, the magnetostrictive effect, comparable to the reverse piezoelectric effect (the internal generation of a mechanical strain resulting from an applied electrical field), can be used for actuators. In this section, magnetoelastic sensor systems are first briefly reviewed, and magnetoelastic or so-called magnetostrictive actuators in microsystems are discussed.

1.3.1 Magnetoelastic Sensors

As mentioned above, magnetoelastic coupling is attractive for wireless resonant sensing because it offers bi-directional wireless communication between magnetic field and the mechanical stress or strain. Although a variety of wireless magnetoelastic sensing systems have been studied, they can be summarized as a system concept as shown in Fig. 1-6 [Gri11]. When excited by a magnetic field, the magnetoelastic sensors vibrate at their mechanical resonant frequency. Simultaneously, the sensors generate a magnetic field due to induced stress. The resonant frequency shift, due to the change of mass and environment, is detected acoustically, optically or magnetically.

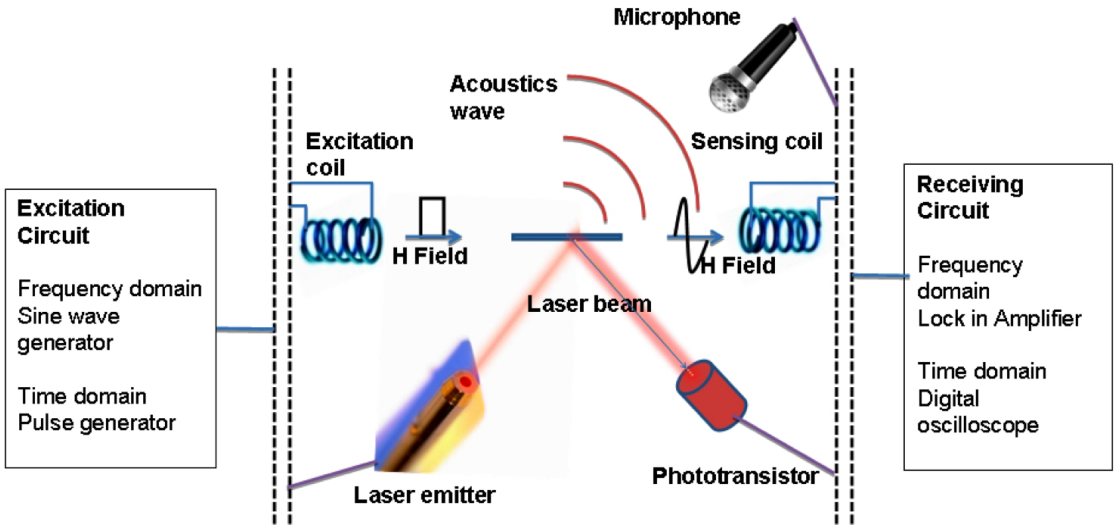

Fig. 1-6: A general configuration for magnetoelastic wireless sensing system. The strip sensor is actuated by magnetic field and its resonant frequency shift due to Young's modulus, mass load and environment changes. This frequency can be picked up optically, acoustically or magnetically [Gri11].

For example, the resonant frequency of a simple ribbon-like film sensor can be expressed by [Lan86]:

$$f = \frac{1}{2L}\sqrt{\frac{E}{\rho}} \tag{1-7}$$

where L is the length of the sensor; E is the young's modulus; and ρ is the density. Further, the frequency shift due to mass and damping coefficient in the environment can be expressed as [Sto00]:

$$\Delta f = -f_0 \frac{\Delta m}{2m_0} \tag{1-8}$$

$$\Delta f = \frac{\sqrt{\pi f_0}}{2\pi\rho_s d}\sqrt{\eta\rho_m} \tag{1-9}$$

where m is the mass; d is the thickness of the sensor; ρ_s is the density of the sensor; ρ_m and η are the density and viscosity of the surrounding medium. These relationships offer sensing capabilities for measurements including Young's modulus [Sch01],

pressure [Kou00], temperature and humidity [Jai00], liquid density and viscosity [Gri00], fluid flow velocity [Gri00'], chemical [Cai00, 04], biliary stent monitoring [Gre09, 10] and so on. With such various sensing capabilities, these systems no doubt have a promising future in practical applications.

1.3.2 Magnetoelastic Actuators

Although magnetoelastic materials have a large impact on sensing systems, utilizing magnetoelastic material for actuation of a miniature and micro-scale system remains an open challenge. In the macro world, magnetoelastic or so-called magnetostrictive alloys, especially giant magnetostrictive materials (GMM), have been used for actuating devices such as linear and rotary motors [Cla97]. In the micro world, there have been only a few actuators developed utilizing the magnetostrictive effect.

Quandt et al developed a micropump using 7.5-μm-thick sputtered giant magnetostrictive TbFe/FeCo multilayer [Qua00]. Magnetostrictive micro mirrors for an optical switch matrix have been studied. A 0.5 μm to 2 μm TbDyFe multilayer was sputtered on a 50 μm thick Si cantilever. A maximum deflection of about 330 μm has been achieved [Lee07]. A miniature rotary motor with 20 mm diameter was developed by utilizing bulk GMM Terfenol-D [Zho09]. The motor was driven by an ac current with 50 Hz and it exhibits a speed of 18 rpm. Another bulk magnetostrictive material – iron gallium alloy (Galfenol) – is used for a translating and bending microactuator [Uen10]. A wireless swimming microrobot driven by giant magnetostrictive thin film – TbDyFe/Polyimide (PI)/SmFe has been studied. It operates at 4.7 Hz and has 4.7 mm/s mean speed [Liu10].

The examples described above demonstrate the potential of the magnetostrictive actuators in microsystems. However, there are still some challenges including (a)

developing of microfabrication compatible machining techniques, (b) designing an efficient energy transfer mechanism, (c) seeking suitable applications, and so on. Further discussing these challenges: (a) There is no standard microfabrication process for magnetoelastic materials. Sputter technology offers a promising solution. But it is not accessible for many researchers; and the process has not been standardized yet. It also has high cost especially for robust actuation requiring thick magnetoelastic layers. Further, although the bulk magnetoelastic material – like GMM – has large magnetostrictivity, it is difficult to pattern using standard microfabrication. The actuators using bulk GMM, as mentioned above, require electrical discharge machining (EDM) or precision micro milling [Uen10]. Thus, magnetoelastic actuators would benefit greatly from fundamental research on magnetoelastic material deposition and bulk magnetoelastic material patterning and bonding. (b) Besides fabrication, magnetoelastic actuator designs require careful consideration. Successful designs should provide efficient transformation from excitation to intended motion, facilitate the integration of the microsystem, and offer performance comparable to other technologies. (c) Magnetoelastic actuators have a specific advantage over other actuation modalities because they can be wirelessly actuated. That is the same reason for such a success in magnetoelastic sensors. By exploring proper applications requiring wireless actuating, this technology will no doubt attract more resources from both academic and industry field.

1.4 Focus of This Work

1.4.1 Wireless Magnetoelastic Resonant Rotary Motor

One major focus of this work is to explore magnetoelastic resonant rotary motor. Along the path, it also seeks possible solutions for magnetoelastic actuation challenges.

First, lithographically patterned bulk-magnetoelastic-thin-films and Si-bulk-magnetoelastic-thin-films are used as actuators. The fabrication process employs photochemical machining (PCM) and Au-In transient liquid phase (TLP) bonding process, which are available and already mature technique compared to sputtering. Second, a 2-D ring-shaped stator design avoids the complex 3-D structures for magnetoelastic motors as presented in [Zho09, Uen10, Par13]. The stacked 2-D structure should also facilitate microsystem integration. Third, standing wave and traveling wave operation approaches are developed based on the stack of 2D structures. The capacitive sensing electrodes are also integrated for real time speed measurement. The performance of the magnetoelastic resonant rotary motors is evaluated.

Fig. 1-7 shows the history of miniaturization of magnetoelastic actuators. The smallest magnetoelastic rotary motor developed so far still have a size that much larger than 1 cm^3. The reported magnetoelastic rotary motors are typically constructed by magnetoelastic rods, requiring complicated 3D structures with relatively large sizes. Although actuators, such as miropump, micromirror can be achieved with less than 0.01 cm^3 volume by using 2D cantilever or diaphragm structure, they are limited to bending motion. In this work, 2D magnetoelastic structures are firstly investigated for achieving rotary actuation in a very small scale.

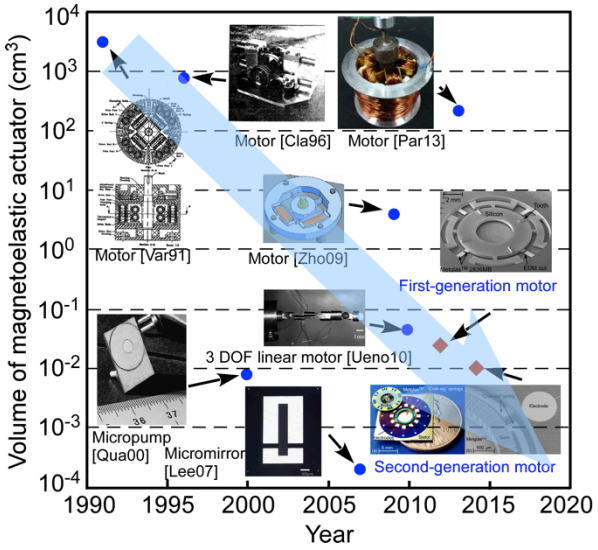

Fig. 1-7: The history of miniaturization of magnetoelastic actuators. The research described in this thesis is represented by the first-generation and the second generation motors.

1.4.2 Miniaturization of Magnetoelastic Tags

Another topic of this PhD work focus on miniaturizing magnetoelastic tags for detection purposes. For example, magnetoelastic tags are widely used for anti-theft system because of the low cost and high performance. However, miniaturization remains a challenge because of the signal loss due to reduce material. The typical sizes of commonly used different types of tags are compared in Fig. 1-8. Two approaches are investigated in order to maintain strong signal response while miniaturization. First, a frame-suspension is used for diminishing the interaction between the magnetoelastic resonator and substrate during the vibration. Second, the signal strength is further boosted by using multiple arrayed or clustered magnetoelastic tags.

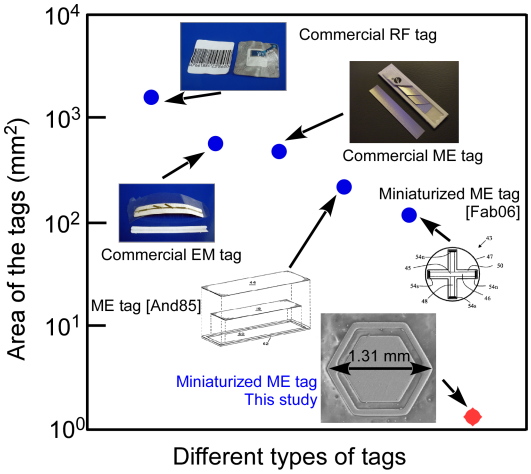

Fig. 1-8: Comparison of the sizes different types EAS tags.

1.5 Organization of this Dissertation

Chapter 2 of this work presents two types of the standing wave magnetoelastic resonant rotary motor, defined as first-generation wireless magnetoelastic motors. First prototype, defined as Design M, is actuated by a ø8 mm magnetoelastic stator lithographically micromachined from Metglas™ 2826MB-bulk-foil with 25 µm thick. It successfully demonstrates the working principle for a magnetoelastically-actuated standing wave resonant motor. Then, a hybrid-integrated silicon and magnetoelastic structure, defined as Design S, is invested for improving performance and realizing bi-directional rotation.

Chapter 3 describes the continuous development of the magnetoelastic resonant rotary motors. The new devices are called second-generation motors. Taking the advantage of the simple structure of the magnetoelastic motor, capacitive sensing electrodes are integrated for achieving real time measurement of the rotational rate. Further, a traveling wave actuation method is first investigated for a magnetoelastic motor.

Chapter 4 changes the focus from actuators and explores the methods to maintain signal strength while miniaturizing magnetoelastic tags for detection purposes. Two approaches are investigated. The first approach employs a frame-suspended magnetoelastic tag is used to increase the response signal strength by reducing the interaction of between the vibration portion and the substrate. The second approach focuses on achieving signal superposition from arrayed or cluster magnetoelastic tags with similar resonant frequencies.

Finally, Chapter 5 gives a summary of the performance for the motors and tags. Potential future work is also proposed for performance improvements.

Chapter 2

First-Generation Wireless Magnetoelastic Motor – Standing Wave Motor

This chapter[1] presents wireless, chip-scale magnetoelastic resonant motors based on standing wave actuation. Two designs are described and defined as first-generation magnetoelastic motors. Design M is actuated by a ø8 mm magnetoelastic stator lithographically micromachined from Metglas™ 2826MB-bulk-foil with 25 μm thick. Design M successfully demonstrates the working principle for a magnetoelastically-actuated standing wave resonant motor. Design S uses a stator with a bilayer of Si (ø8 mm diameter and 65 μm thick) and magnetoelastic foil (ø8 mm diameter and 25 μm thick) to tailor the stiffness. Design S provides a significant performance improvement compared to Design M, along with facile bi-directional rotation functionality. It is also a successful device-level demonstration of using a hybrid-integrated silicon and magnetoelastic structure, taking advantage of the mechanical properties and precision micromachining offered by silicon and the wireless actuation capability offered by magnetoelastic materials. More details on the architectures, fabrication, and characterization are given in the following sections.

2.1 Design

2.1.1 Theory

The rotary actuation mechanism in this effort is similar to that for piezoelectric ultrasonic rotary motors [Iio00]. A vibratory wave, which could be either standing wave

[1] Contents presented in journal paper form in [Tan13].
[2] Contents presented in journal paper form in [Tan14] and in patent form in [Gia14].

or travelling wave, is generated in the stator. In this case, the vibratory micro-motion is a standing flexural resonant wave and is generated magnetoelastically. The resulting vibratory mode shape of the stator has antinodes at which maximal out-of-plane deflection occurs. Teeth are located on the stator such that they are slightly offset from the antinodes, resulting in elliptical motion of the teeth tip and a contact force with a tangential component that causes the rotor to rotate (Fig. 2-1). By selecting resonant frequency of different mode shape of the stator, bi-directional rotation can be achieved. A rotor, which can contain other microsystem components, is then stacked above the stator.

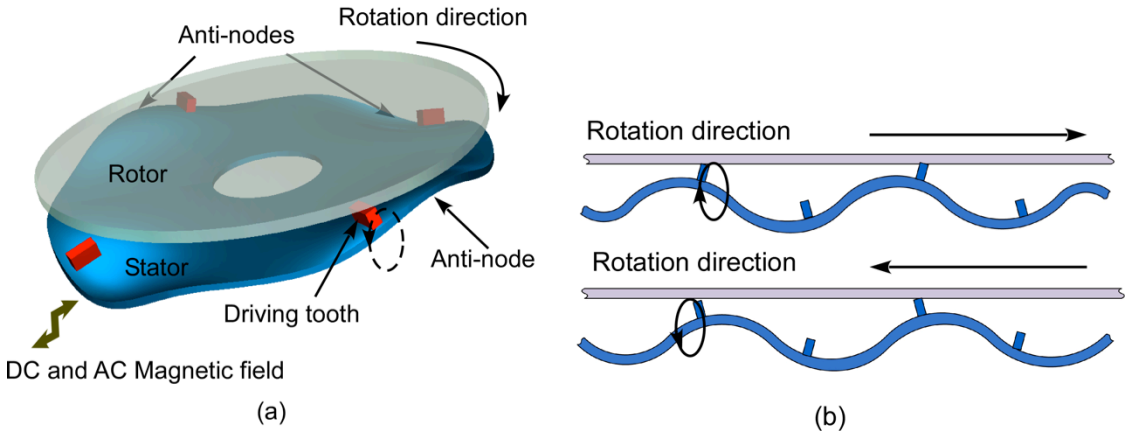

Fig. 2-1: Wireless magnetoelastic resonant rotary motor operation concept: (a) a standing wave in stator, (b) bi-directional rotation operation method.

Singular magnetoelastic material, which can either be the vibrating stator itself or the actuator for the stator, can be wirelessly driven by magnetic fields. The deformation is substantially enhanced if a proper DC magnetic field is superimposed on the AC magnetic field. Thus, both DC and AC magnetic field are required for rotary motor wireless actuation [Gri01].

2.1.2 Modeling

A custom magneto-mechanical harmonic finite element technique [Gre09] is used to estimate modal displacements, shapes, and frequencies for the magnetoelastic material. Although magnetoelastic materials are generally non-linear, it is appropriate to use linearized constitutive equations describing the coupling between magnetic flux density, magnetic field strength, stress, and strain in a magnetostrictive material:

$$\vec{\sigma} = [C]\vec{\varepsilon} - \frac{[C][d]^T}{\mu_0 \mu_r}\vec{B} \tag{2-1}$$

$$\vec{H} = -\frac{[d][C]}{\mu_0 \mu_r}\vec{\varepsilon} + \frac{1}{\mu_0 \mu_r}\vec{B} \tag{2-2}$$

where s is the stress vector, C is the stiffness matrix, e is the strain, d is the magnetostrictivity matrix, B is the magnetic flux density vector, H is the field strength vector, μ_0 is the permeability of free space, and μ_r is the relative permeability. Equations (1) and (2) are implemented in this work utilizing COMSOL Multiphysics and coupled time-harmonic induction current and stress-strain frequency response modes. A detailed look at a Finite Element Analysis (FEA) implementation for magnetostrictive materials is presented in [Ben05]; the approach used in this work is modified for application to resonant actuators. In this paper, two types of magnetoelastic rotary motor: Design M and Design S are modeled and investigated.

2.1.3 Design M

The Design M motor consists of a stator fashioned from magnetoelastic material – Metglas™ 2826MB – and two stainless steel bases (Fig. 2-2). The stacked architecture is modular, which significantly simplifies the fabrication process. Each layer can be easily fabricated utilizing photochemical machining (PCM) process, as described in the

fabrication section. Alignment pins ensure reasonable assembly accuracy. Two stainless steel bases provide a recess – allowing stator vibration – and initial positions for alignment pins and a hub. The ring-shaped stator is suspended with four crab-leg springs, which are stiff in the rotational direction but flexible in the out-of-plane direction – preventing stator rotation during rotor actuation while allowing large vertical deformation.

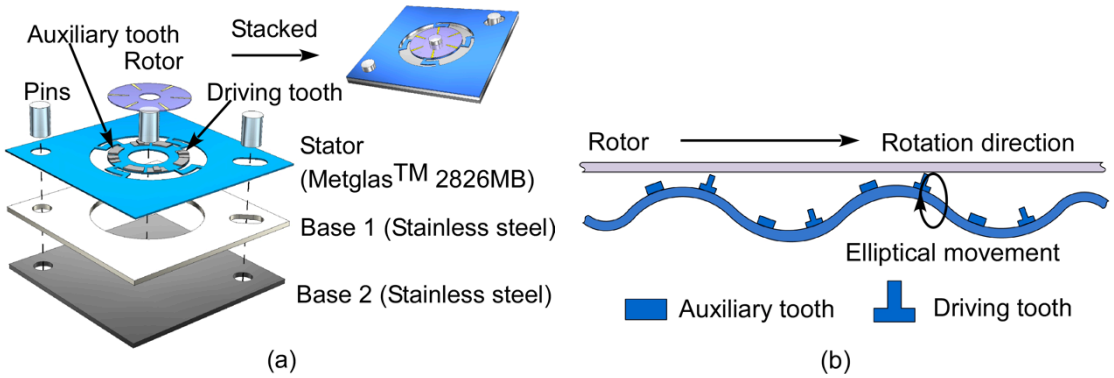

Fig. 2-2: Schematic of Design M geometry (a) and customized teeth design (b). In Design M, the stator is fabricated from magnetoelastic metal foil alone.

For a stator fabricated solely from Metglas™ 2826MB, careful consideration is required for the placement of the driving teeth. The number of driving teeth is usually the same as the number of antinodes in the desired mode shape for a standing wave resonant rotary motor [Iin00]. The driving teeth are typically offset from the location of the antinodes in order to ensure elliptical motion of the tooth tip. However, in the case of the extremely lightweight Metglas™ 2826MB stator, the mass loading added by the driving teeth causes the antinodes to shift to the same location as the teeth. Consequently, the teeth no longer move elliptically and no rotation is generated. Therefore, as shown in Fig. 2-2, a design employing 8 teeth is proposed to address the issue. There are still four sets of teeth, but one set of teeth is a combination of two teeth: an auxiliary tooth and a driving tooth, each separated slightly from each other. The

auxiliary teeth and driving teeth have the same mass so that the mass center and antinodes of the vibratory mode shape will be in the center between the two different teeth. However, the driving tooth is taller so only it will contact the rotor. As a result, the driving teeth can move in an elliptical manner, and drive the rotor tangentially.

The FEA results shown in Fig. 2-3 predict that a stator (4 mm inner diameter, 8 mm outer diameter and 25 μm thickness) has the desired mode shape at a resonant frequency of about 11.43 kHz, with 0.1 μm out-of-plane deformation under harmonic excitation with amplitude of 2 Oe. Due to the orientation and size of the teeth and spring suspension, slightly different performance is predicted for different directions of alternating magnetic excitation. Simulation results suggest that applying magnetic field between the suspension springs gives the largest out-of-plane displacement amplitude. As desired, the vibration mode shape demonstrates that the antinodes are located in the center between a driving tooth and an auxiliary tooth.

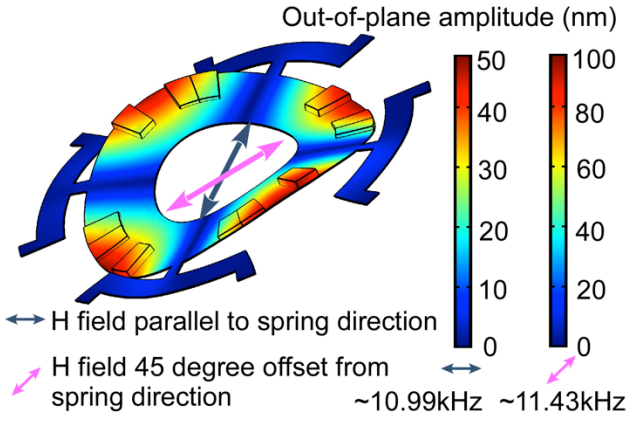

Fig. 2-3: FEA simulation results of frequency response of bulk-magnetoelastic-foil stator of Design M.

2.1.4 Design S

As shown in Fig. 2-4, the Design S has a stacked structure similar to that of Design M, but the stator is made of a silicon-Metglas sandwich instead of solely

Metglas™ 2826MB. The benefit of silicon is that it has better surface uniformity compared to magnetoelastic foil. Further, the higher resonant frequency and quality factor of the thicker silicon can potentially increase the rotation rate and improve the positioning resolution. Using standard micromachining processes, silicon should facilitate the direct integration of the driving teeth on the stator. The thicker silicon also means that no auxiliary teeth are required in this design, and the intended bi-directional rotation can be realized by switching the driving frequency and mode shapes. A ring-shaped Metglas™ 2826MB disc is attached to the Design S stator so that the motor is still wirelessly driven by magnetic fields. The rotor is patterned to have six radial segments so that the rotation rate can be measured visually or optically.

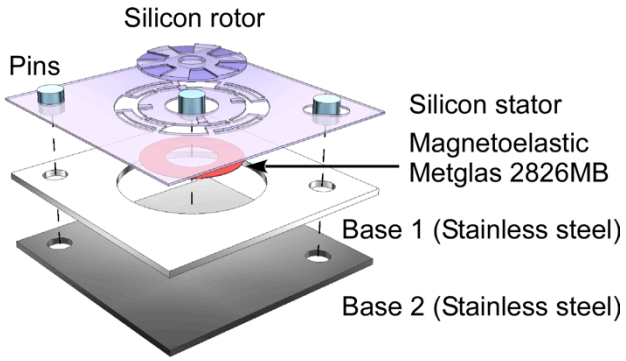

Fig. 2-4: Schematic of Design S geometry. In Design S, the stator is fabricated from a layer of magnetoelastic metal foil bonded to Si.

The FEA simulation results show that the design of the teeth can be simplified because the stator is thick and robust compared to the teeth. Additionally, bi-directional rotation can be achieved by switching the mode shapes of stator (Fig. 2-5). The intended CW vibration mode shape of a Design S stator with 4 mm inner diameter, 8 mm outer diameter and 65 μm thickness is simulated to be at 8 kHz with 3.2 μm amplitude; the CCW vibration mode shape exists at 11 kHz with 2.7 μm out-of-plane amplitude. A 6 Oe magnitude AC magnetic field is applied in the simulation.

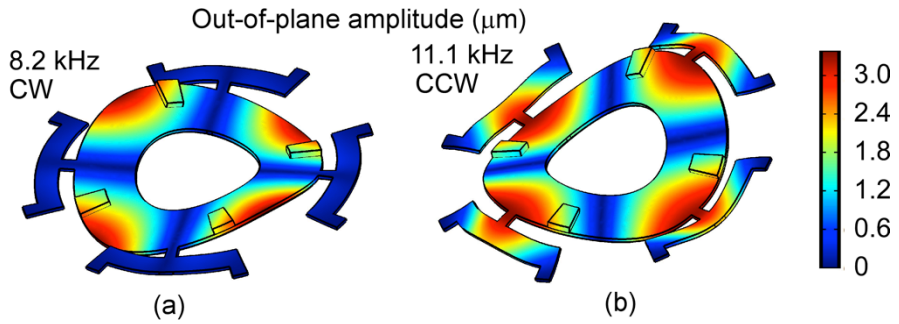

Fig. 2-5: FEA simulation results of frequency response of Design M stator with two mode shapes.

2.1.5 Material Selection

Metglas™ alloys provide excellent magnetostrictive properties as well as adequate mechanical properties. In this design, Metglas™ 2826MB, an amorphous NiFeMoB alloy, is used. Its saturation magnetostriction is 12 ppm and its DC permeability is larger than 50000 [Met08]. These materials are readily available in foils (≈25 μm thick) and are easy to pattern utilizing PCM. Relative to other Metglas™ alloys and magnetoelastic materials, 2826MB also requires a small DC bias (less than 10 Oe) and can be stimulated with a relatively small alternating field.

2.1.6 Driving Methods

In principle, an on board coil and permanent magnets can be implemented to provide the driving AC and DC magnetic fields. For example, inductive coils for generating AC magnetic fields can be patterned on an underlying silicon substrate using standard micromachining techniques. On the same substrate, permanent magnet materials such as permalloy or samarium cobalt can be deposited and used to provide the DC fields required to bias the magnetoelastic material. However, for the motors presented in this work, external coils are used.

2.2 Fabrication

2.2.1 Design M Fabrication

The fabrication process flow of a Design M motor is illustrated in Fig. 2-6 (a). First, the magnetoelastic stator is batch-patterned using PCM [ASM89] from the Metglas™ 2826MB foil. The ring-shaped stator is patterned with inner diameter of 4 mm and outer diameter of 8 mm, and with thickness of 25 µm. Other base layers are also fabricated using PCM from 0.5 mm thick stainless steel foils. The layers are stacked and aligned with pins, and bonded to each other with epoxy. The stainless steel auxiliary teeth (500-µm-wide and 300-µm-tall) and driving teeth (300-µm-wide and 500-µm-tall) are manually placed on the stator and fixed with epoxy. The rotor is micro-electro-discharge-machined (µEDM) from Metglas™ 2826MB foil; it has a total mass of about 9 mg. A hub with diameter of 2 mm is used to constrain the rotor. The overall size of the chip is 2 × 2 cm^2 (Fig. 2-6 (b)).

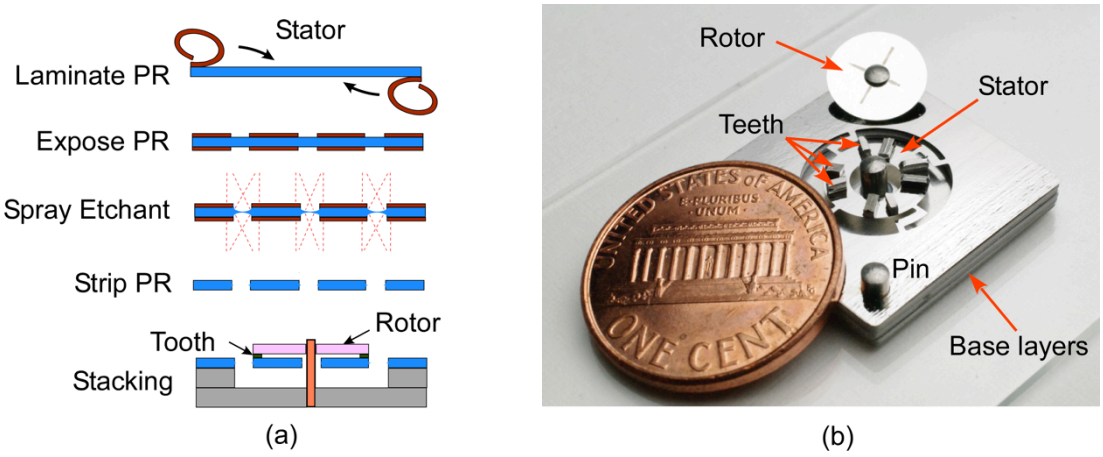

Fig. 2-6: Fabrication process flow of Design M (a) and optical image of assembled device (b).

2.2.2 Design S Fabrication

For Design S, the stator and the rotor are fabricated side-by-side using a two-mask deep reactive-ion etching (DRIE) process, as shown in Fig. 2-7 (a-d). The fabrication process starts with coating a layer of KMPR 1010 on the backside of a silicon wafer, to serve as an etch stop and support layer for through-wafer etching. Silicon oxide of 4 μm thickness is then deposited on the front side of the wafer by PECVD and is patterned using mask 1. The silicon oxide layer is wet etched in 5:1 BHF (buffered hydrofluoric acid) solution. Photoresist is used to mask the first DRIE step in which the ring-shaped stator is defined. Then, the PR is removed and remaining silicon oxide layer is used as a mask to etch with DRIE through the remainder of the wafer. At the end of this process, the ring-shaped stator is fully etched out along with the teeth that are located on the stator. After removing KMPR 1010 by immersing the wafer in Remover PG (MicroChem Corporation, Newton, MA) at 80 °C for 1 hour, the silicon rotor is ready for assembling. The silicon stator must be bonded to Metglas™ 2826MB as described in following steps.

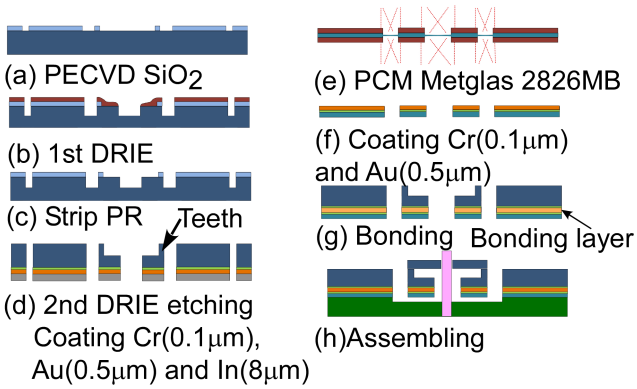

Fig. 2-7: Fabrication process flow of Design S.

2.2.3 Indium Rich Au-In Bond

An Au-In liquid transient phase bonding (TLP) is used because it can be performed at relatively low temperature, ensuring that magnetic properties of Metglas™

2826MB will not change. Additionally, gold and indium can be easily coated using standard microfabrication steps. The possible stages of TLP bonding for an indium rich bond layer are shown in Fig. 2-8 [Lee93, So00]. Liquid-solid inter-diffusion, stage 1, occurs when two substrates are brought into intimate contact while the temperature is above 157 ˚C, and the appropriate pressure is applied. Liquid indium dissolves gold layers on both the silicon substrate and the Metglas™ 2826MB substrate. Simultaneously, dissolved gold diffuses into the indium layer to form $AuIn_2$. Stage 2 occurs upon cooling; the final bonding layer is a mixture of solid indium and $AuIn_2$ because the quantity of gold is insufficient to react with all the indium.

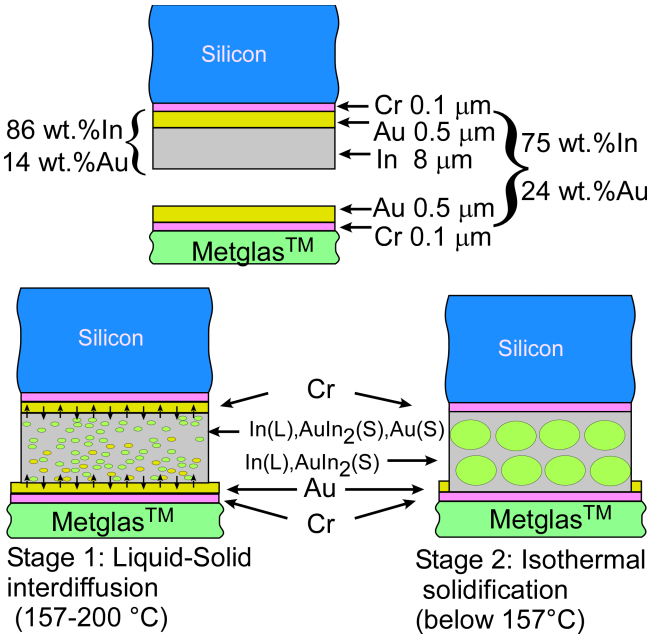

Fig. 2-8. Composition of Au-In TLP bonding and possible stages of bonding process: Stage 1 melting of In and liquid-solid interdiffusion at 157-200 °C, Stage 2 solidation of the mixture below 157 °C [Lee93, So00].

The use of this bonding step with the process sequence of the Design S motors is shown in Fig. 2-7 (d-g). Initially, chrome (0.1 μm) and gold (0.5 μm) is evaporated on both the Metglas™ 2826MB ring-shaped structure and the backside of the silicon stator. The step is followed by electroplating of ≈8 μm indium on the backside of the silicon

stator. The chosen indium thickness is sufficient to cover the bonding surface of the Metglas with a surface roughness of ≈1 μm and maximum peak-to-peak variations of ≈4 μm, which is measured by interferometer. The silicon stator and the Metglas™ 2826MB component are aligned and bonded. The bonding process is performed in a vacuum oven so that oxidation is prevented. The temperature is held at 200 °C for 1 hour during this step. After bonding, the connections between ring-shaped disc and frame in the Metglas™ 2826MB layer are cut using μEDM. An SEM image of the silicon stator with bonded ring-shaped Metglas™ 2826MB is shown in Fig. 2-9 (a).

As the final step before testing, the Design S stator, stainless steel bases, and a hub are aligned, stacked and fixed to each other with epoxy. The silicon rotor located directly above the stator is constrained by the hub and touches the stator only at the teeth. The optical image of assembled Design S motor is shown in Fig. 2-9 (b).

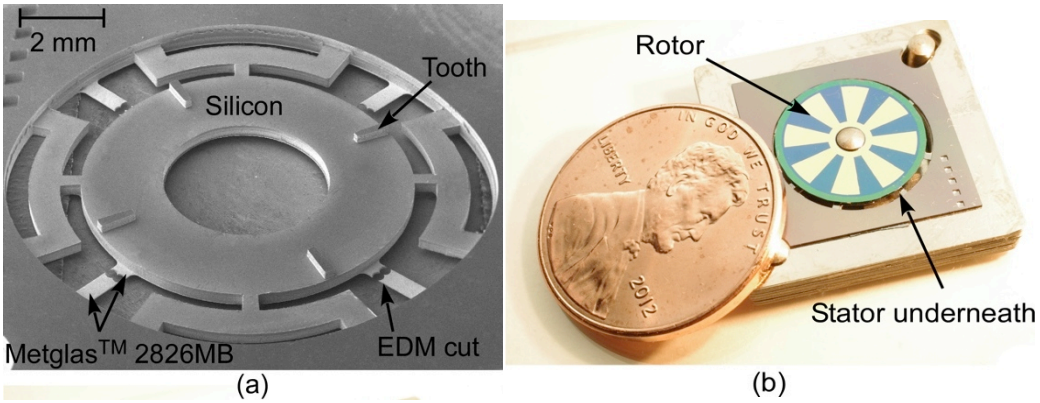

Fig. 2-9: SEM image of the Design S stator (a) and optical image of assembled device (b).

2.3 Experimental Methods and Results

2.3.1 Experimental Methods

The motors were actuated wirelessly using two sets of coils. Two coils with a diameter of 12.5 cm, shown in Fig. 2-10, were connected to a DC power supply providing constant current to provide DC magnetic field. This arrangement was used to

bias the magnetoelastic material into an operating region in which the strain is sensitive to magnetic field. For Design M, based on the relationship between the magnetostriction coefficient and the applied field for Metglas™ 2826MB [Kim99], the DC bias field was set to 3 Oe, with ±2 Oe AC field. However, the effective magnetostriction curve appears to be shifted for Design S, as suggested by the magnetic bias at which the rotation rate is highest. The cause of bias shift for Design S may be related to residual stresses from the bonding process; the reference curve was measured on a free-free sample. Thus, the DC bias field of Design S was set to 8 Oe to achieve a high rotation rate (Fig. 2-11).

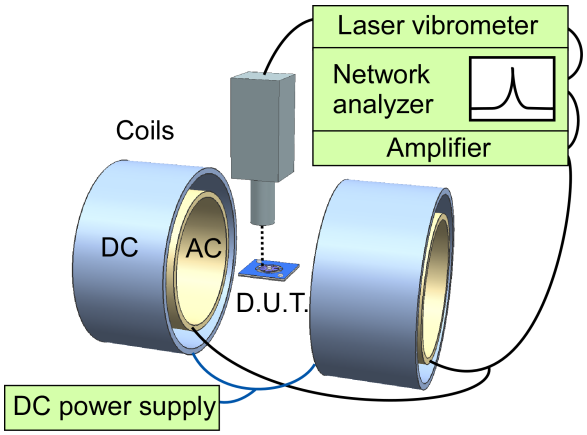

Fig. 2-10: Experimental set up for motor actuation and frequency response measurement.

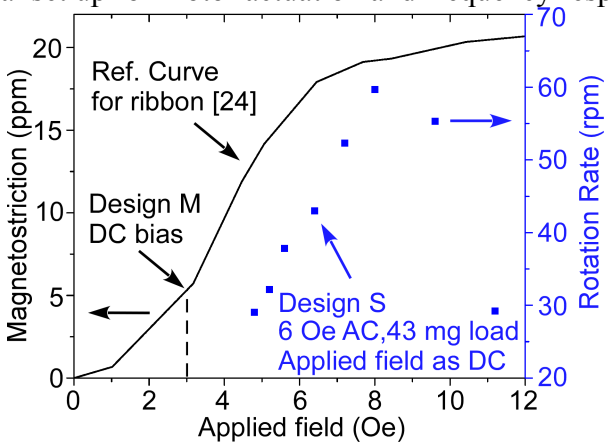

Fig. 2-11: Magnetostriction versus applied field for Metglas™ 2826MB (reproduced from [Kim99]) and rotation rate versus applied DC bias at fixed AC field. The derivative of the reference curve at a bias point leads to the magnetostrictivity ("*d*" in the constitutive equations in section 2.1.2) at that bias point. The effective magnetostriction curve appears to be shifted for Design S, as suggested by the magnetic bias at which the rotation rate is highest.

Another two coils with diameter of 11.5 cm were placed inside the DC coils; these smaller coils generated an alternating magnetic field with amplitude from 2 to 6 Oe, depending on the applied power. A DC current, equal to the measured AC current amplitude, was first applied on the AC coils. Subsequently, the DC magnetic field, equivalent to the AC magnetic field amplitude, was experimentally measured by a FW Bell 5180 Hall Effect Gaussmeter (Pacific Scientific OECO, Milwaukie, OR). The device under test (D.U.T.) was placed between the coils.

To measure the frequency response of the stator, a laser vibrometer and a network analyzer were used in conjunction (Fig. 2-10). The vibration mode shape can be determined by measuring a number of points along the rim of the stator; antinodes of a given mode shape exist at locations of strong response at a given frequency.

A video camera was used to record the motors from above, and the video is analyzed frame-by-frame to derive the rotation rate and initial acceleration. In addition to this method, a laser displacement sensor was used to monitor the patterned surface of the rotor. The frequency of the resulting square wave was used to calculate the rotation rate.

2.3.2 Design M Results

The desired mode shape with four antinodes was confirmed to exist at 11.35 kHz, with 0.2 μm unloaded out-of-plane deflection at the antinodes. As shown in Fig. 2-12, the frequency response is stable over at least 5 minutes of operation time. In preliminary tests, a typical rotation rate of approximately 44 rpm (4.6 rad/s) was obtained (Fig. 2-13). An angular driving step size of about 23 milli-degree is calculated from the measured angular velocity and resonant frequency. The angular velocities from different trials were calculated from the recordings and are shown in Fig. 2-14.

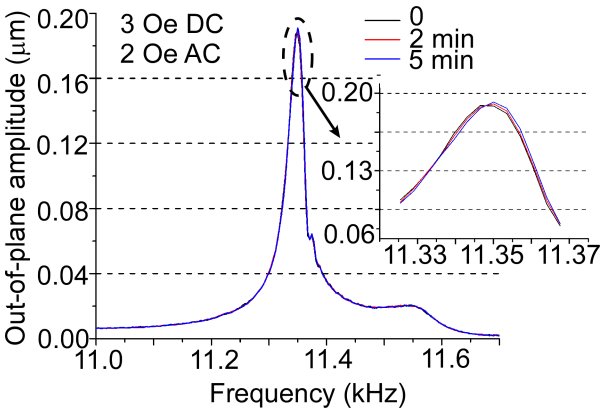

Fig. 2-12: Experimentally measured frequency response of bulk-magnetoelastic-foil stator of Design M, with 3 Oe DC, 2 Oe amplitude AC magnetic field.

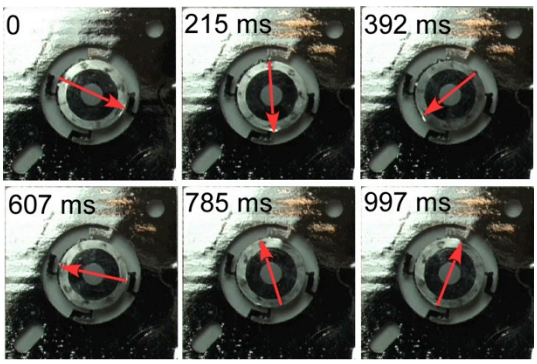

Fig. 2-13: Optical images of Design M rotating with 3 Oe DC, 2 Oe amplitude AC magnetic field at frequency of 11.35 kHz, and 9 mg payload.

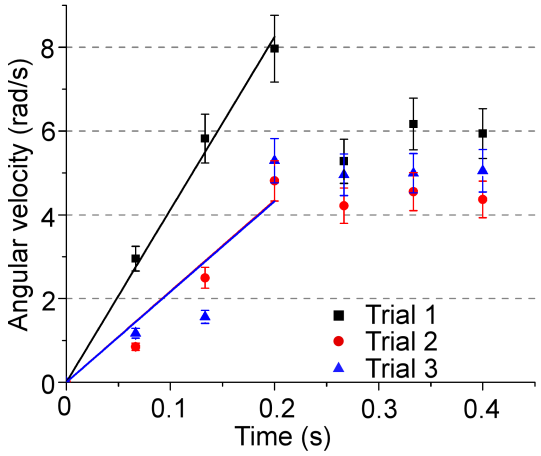

Fig. 2-14: Experimentally measured angular velocity of Design M as a function of time with 3 Oe DC and 2 Oe amplitude AC magnetic field at frequency of 11.35 kHz. Linear fits of different trials were used to calculate initial acceleration.

The associated start torque (i.e., the motor driving torque minus friction torque when rotation rate is approximately zero) is ≈2 nN·m. This is calculated by $\tau = \alpha I$, where τ is the start torque, α is the angular acceleration. The angular acceleration, before the angular velocity plateaus, was derived from the average of linear fit slopes from different trials. The moment of inertia, I, is further given by $I = \frac{1}{2} m(r_1^2 + r_2^2)$, where m is the mass of the rotor, and r_1 and r_2 are the inner and outer radii of the rotor, respectively.

2.3.3 Design S Results

The frequency response of Design S was also measured and it was confirmed that two mode shapes exist that can provide bi-directional operation. The CW mode shape was confirmed to exist at 6.08 kHz, with about 2 μm unloaded out-of-plane deflection at the antinodes (Fig. 2-15 (a)), whereas the CCW mode shape was confirmed to exist at 7.85 kHz, with about 1.8 μm unloaded out-of-plane deflection at the antinodes (Fig. 2-15 (b)). The frequencies are lower than FEA results. Further study is required to understand the reason for the lower-than-expected resonant frequencies.

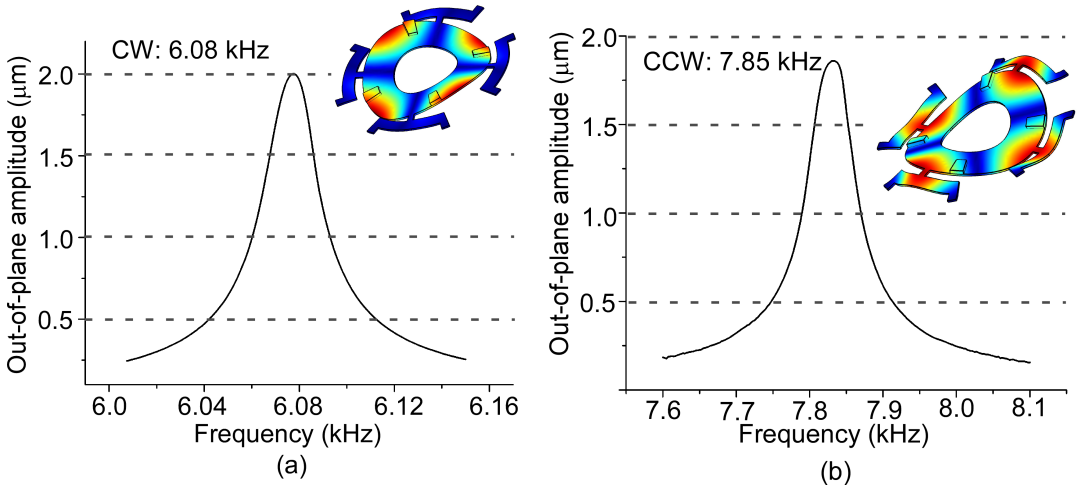

Fig. 2-15: Experimentally measured frequency response of Design S stator (65 μm thick) with no load, 8 Oe DC and a 6 Oe amplitude AC magnetic field. The quality factors of resonant response of CW mode and CCW are 150 and 79, respectively.

The bi-directional rotation was demonstrated at corresponding resonant frequencies. The typical rotation rates of CW and CCW directions are about 30 and 100 rpm when an 22 mg rotor was used, an AC magnetic field with about 6 Oe amplitude, and a DC magnetic field with 8 Oe amplitude was applied. However, the CW rotation rate is relatively slow and rotor wobbling was observed. This is possibly due to the fact that the tooth locations are too close to the antinodes of CW vibration mode shape. Consequently, vertical movement instead of tangential movement dominates the motion of the tooth tip so that the rotor is mainly pushed vertically rather than tangentially. This problem can be solved by placing the tooth equally far from the antinodes of both CW and CCW mode shapes in future designs. More characterization was performed on the CCW mode.

The effect of payload on CCW rotation rate was characterized by using rotors with different weight. For example, for the 43 mg rotor with six patterned segments used in this test, a square wave was obtained to calculate the rotation rate of about 60 rpm (Fig. 2-16). As shown in Fig. 2-17 (a), the rotation rate decreases when the payload increases in an approximate linear relationship. Design S showed at least 43 mg payload capability. The rotation rate was also closely related to applied power or applied AC magnetic field strength. The rotation rates were measured when the magnitude of the AC magnetic field increases from 3 Oe to 6 Oe. As shown in Fig. 2-17 (b), rotation rate increases with the increasing AC magnetic field in an approximately linear manner. This indicates that magnetoelastic material still operates in the intended linear region of magnetostriction versus applied field curve.

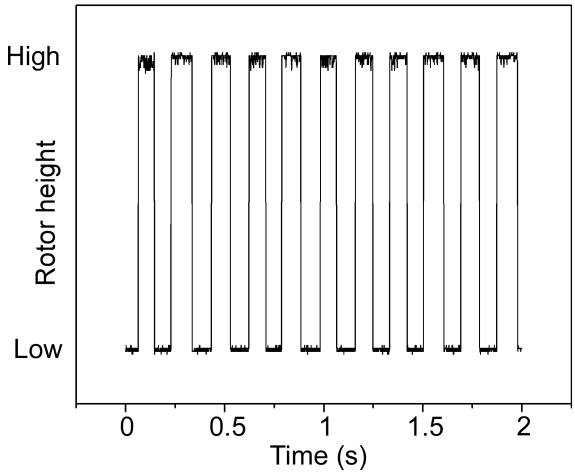

Fig. 2-16: Rotation rate measurement of Design S with 43 mg payload, 8 Oe DC and a 6 Oe amplitude AC magnetic field at frequency of 7.85 kHz.

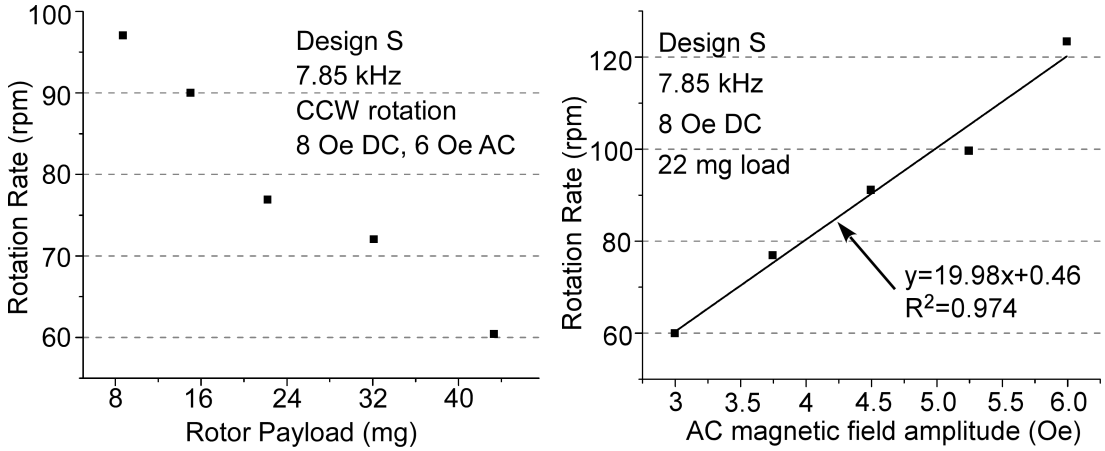

(a) (b)

Fig. 2-17: (a) Experimentally obtained effect of payload on rotation rate of Design S, with 8 Oe DC and a 6 Oe amplitude AC magnetic field at frequency of 7.85 kHz; (b) Experimentally obtained effect of applied AC magnetic field on rotation rate of Design S, with 8 Oe DC, 22 mg payload, and at frequency of 7.85 kHz.

The transient response of Design S was experimentally evaluated. Results obtained with a 22 mg payload are shown in Fig 2-18. This data was obtained by analyzing a slow-motion video. The typical performance achieved a rotation rate of about 100 rpm (10.5 rad/s), start torque of 30 nN·m, and step size of 74 milli-degree. The

start torque is calculated using the same method for Design M. The performance of the two designs is summarized and compared in Table 2-1.

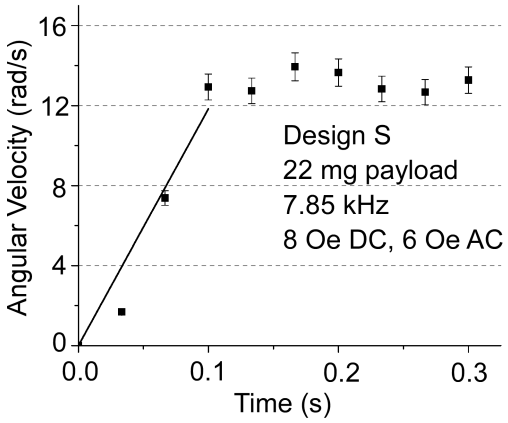

Fig. 2-18: Experimentally measured angular velocity of Design S as a function of time with 8 Oe DC and a 6 Oe amplitude AC magnetic field, at frequency of 7.85 kHz, and 22 mg payload. Linear fit was used to calculate initial acceleration.

Table 2-1: Typical rotation rate, driving step size, start torque, payload, and bi-directional rotation capability of Design M and Design S.

	Design M	Design S
Rotation rate (rpm)	44	100
Step size (milli-degree)	23	74
Start torque (n·Nm)	2	30
Payload (mg)	9	43
Bi-directional	No	Yes

For Design S, one advantage of utilizing silicon is the ability to tune the resonant frequency during fabrication by changing the thickness of the silicon stator. Different resonant frequencies can provide different performance according to application requirements. In general, a higher resonant frequency means a smaller step size of each push between the rotor and the teeth, resulting in a more precise rotation and slower speed. Table 2-2 summarizes the resonant frequencies and performance of Design S motors with different thickness of silicon stator.

Table 2-2: Resonant frequencies, rotational rate and average step size for Design S motors with 65 μm and 150 μm thick silicon stator. The rotational rates of two motors were measured when 22 mg payload was applied.

Thickness of silicon stator	CW Res. Res. Freq.	CCW Res. Freq.	Rotational Rate	Average Step size
65 μm	6.08 kHz	7.85 kHz	≈940˚/s	0.116˚
150 μm	12.3 KHz	18.2 kHz	≈500˚/s	0.008˚

2.4 Discussion

Design M demonstrated the concept of wireless magnetoelastic actuation, but the performance was compromised by two factors. First, the positioning and assembling of the teeth, which was performed manually, contributed to a loss of performance. Second, an uneven magnetoelastic stator surface resulted in unstable rotation rate. Further, because the customized teeth design limits vibration mode shapes of the stator, only CW rotation was achieved. Design S was designed based on the results of Design M. The thick silicon stator has better surface uniformity and simplifies the tooth design. This resulted in stable rotation rate and bi-directional operation capability. Design M also exhibited larger payload capability. The Au-In TLP bonding process was customized to attach magnetoelastic material to silicon. This bonding process has potential applications in other magnetoelastic actuation and sensing systems.

2.4.1 Advantages of Magnetoelastic Wireless Motor

The magnetoelastic wireless resonant motors demonstrate that the magnetoelastic material has significant potential for actuation in miniature and micro-scale devices. The main advantage – the wireless aspect of the actuation approach – allows miniaturization and eliminates lead transfer to the actuator, which is especially preferred for implantable applications.

In addition to being wireless, magnetoelastic resonant motors offer other

advantages shared by ultrasonic piezoelectric motors, such as high precision and high torque. Design S was able to move at least 100 mg payload. These capabilities will enable integration of inertial sensors on the rotor in the future. For example, it is demonstrated that Design S motor can provide a bi-directional rotational stimulus (≈360˚/s) for a commercial gyroscope with about 60 mg mass.

Compared to conventional electromagnetic motors, magnetoelastic micro-motors have very simple structures and only require a single AC excitation signal. The performance of rotation rate and step size can be potentially improved by increasing the resonant frequency of the silicon stator. This can be achieved by either increase the thickness of the stator or decrease the size of the stator. Additionally, a method for braking the motion of the rotor can be provided by exploiting bi-directional rotation capability. For example, CCW rotation can be stopped abruptly by switching the exciting frequency from CCW to CW with a calibrated AC magnetic field. Finally, as mentioned before, external coils can be potentially replaced by on-chip driving coils for short-range wireless operation.

2.4.2. Long-Term Performance and Passive Lock Down

Because the rotation results from the friction and collisions between the silicon teeth and rotor, the material in contact areas will be worn after long-term operation. This wear changes the contact area and friction coefficient during the contact, and results in a slightly different performance of the motor. This effect was characterized by monitoring the rotational rate when the motor is driving for 25 hours continuously, as shown in Fig. 2-19. The rotational rate varies at a range of 50±10 revolutions per second (RPM). This suggests that a real time speed measurement and a feedback control loop are necessary if an application requires accurate rotational rate output.

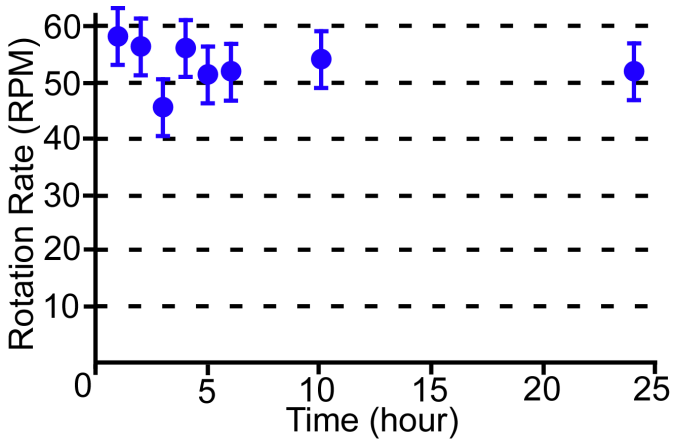

Fig. 2-19: Experimentally measured rotational rate of Design S motor with 65 μm thick silicon stator for 25 hours.

2.5 Summary

In summary, this chapter presents the analysis, fabrication, and experimental results of wirelessly actuated, chip-scale standing wave rotary motors. Two designs are described. Design M is actuated by a ø8 mm magnetoelastic stator lithographically micromachined from Metglas™ 2826MB-bulk-foil with 25 μm thick. It operates at a resonant frequency of 11.35 kHz while a 3 Oe DC and a 2 Oe-amplitude AC magnetic field are applied. The measured rotation speed, start torque, calculated driving step size, and payload are 44 rpm, 2 nN·m, ≈23 milli-degree and 9 mg, respectively. Design S uses a stator that is a sandwich of Si (ø8 mm diameter and 65 μm thick) and magnetoelastic foil (ø8 mm diameter and 25 μm thick) to tailor the stiffness. The typical resonant frequency of clockwise (CW) mode and counterclockwise (CCW) mode are 6.1 kHz and 7.9 kHz, respectively. The CCW mode provides a rotation rate of about 100 rpm, start torque of 30 nN·m, driving step size of 74 milli-degree, while a 8 Oe DC and a 6 Oe-amplitude AC magnetic field are applied. Bi-directional rotation is realized by switching the applied frequency, thereby exciting the stator in a slightly different mode shape. Design S shows at least 100 mg payload capability.

Chapter 3

Second-Generation Wireless Magnetoelastic Motor – Integrated with Capacitive Sensing for Real Time Rotation Rate Measurement

Chapter 2 described the successful demonstration of the magnetoelastic resonant motor with bi-directional rotation based on a standing wave. The utility of these motors could be improved through real time rotational rate measurement functionality provided by integrated on-chip capacitive sensors. Another potential avenue for improving the motor operation and sensing precision is the utilization of a traveling wave operation method for magnetoelastic motors. Because a traveling wave motor can potentially handle more preload between the rotor and the stator (and in some cases requires a preload for sufficient driving torque), such an architecture may result in a more constrained rotor less prone to wobble and lateral runout. As described in this chapter, both of these approaches are incorporated in second-generation motor designs. These second-generation motors utilize a bilayer of silicon and magnetoelastic material structures, similar to that incorporated in Design S of the first-generation motors. The second-generation motors are carefully designed and fabricated to provide better control of deformation induced by the AuIn bonding process due to the thermal expansion difference between silicon and Metglas^{TM}. This deformation is particularly important in these second-generation motors because it is one aspect defining the vertical gap between the capacitive sensing electrodes. The details of the architectures, fabrication, characterization and future plans are given in the following sections.

3.1 Design

3.1.1 Standing Wave Motor Design

The second-generation standing wave magnetoelastic motor also utilizes a bilayer of silicon and magnetoelastic material as a stator, which is similar to that of the first-generation magnetoelastic motor (Design S). The standing waver motor has teeth located offset from the "crab-leg" spring suspensions, and electrodes patterned on the stator frame. Completing the motor is a silicon rotor with patterned electrodes and open windows for optical measurements (Fig.3-1). The stator shape is changed slightly from that used in Design S: a thin silicon "ring" is used rather than the wider "donut". Additionally, the magnetoelastic layer is a full disc rather than the "donut" used previously. These shapes were used in order to reduce the resonant frequencies while obtaining a larger vibration amplitude.

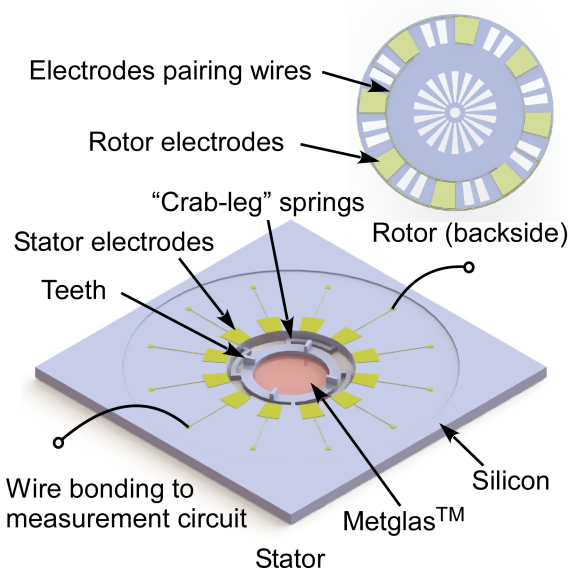

Fig. 3-1: 3D schematic of the standing wave motor.

Compared to the first-generation magnetoelastic motor, the second-generation motor requires a precise control of the deformation of the stator resulted from thermal expansion coefficient mismatch between the silicon and Metglas™ after the bonding.

The deformation of the stator can push the top surface of the teeth significantly above the plane of the electrodes, resulting in a large reduction in the nominal sensing capacitance. A smaller nominal sensing capacitance is inherently more difficult to measure. Thus, the dimensions of the "crab-leg" springs are specifically chosen to reduce the displacement of the top surface of the teeth, with the detailed description of the method given in next section.

3.1.1.1 "Crab-leg" Spring Design

There are two advantages of "crab-leg" springs for this specific issue. First, the "crab-leg" springs is tangential to the "ring" structure, leading to a small spring constant in radial directions. This facilitates stator expansion in radial direction, and radial expansion is one avenue for relieving stresses due to thermal expansion mismatch. Second, the "crab" springs also have a very small vertical spring constant, which allows a "downward" deformation of the stator rim that can compensate the "upward" deformation at the center of the stator that is a result of the bending stresses induced by thermal expansion mismatch.

For predictive design, COMSOL Multiphysics can calculate stresses and deformation due to thermal expansion mismatches and differences between the solidification temperature during bonding (157˚C) and normal operating (room) temperature. The FEA model used in this study is verified by comparing its output to the experimental results of the first-generation motor. The FEA generated results (72.4 μm deformation) matched very well with the fabricated and measured devices (70 μm deformation). Thus, the same model was used as a predictive tool to estimate the displacement of the teeth due to thermal expansion mismatch and to determine suitable

geometry for the "crab-leg" springs. The expected out-of-plane deformation of the stator is estimated using FEA simulation (Fig. 3-2 (a)).

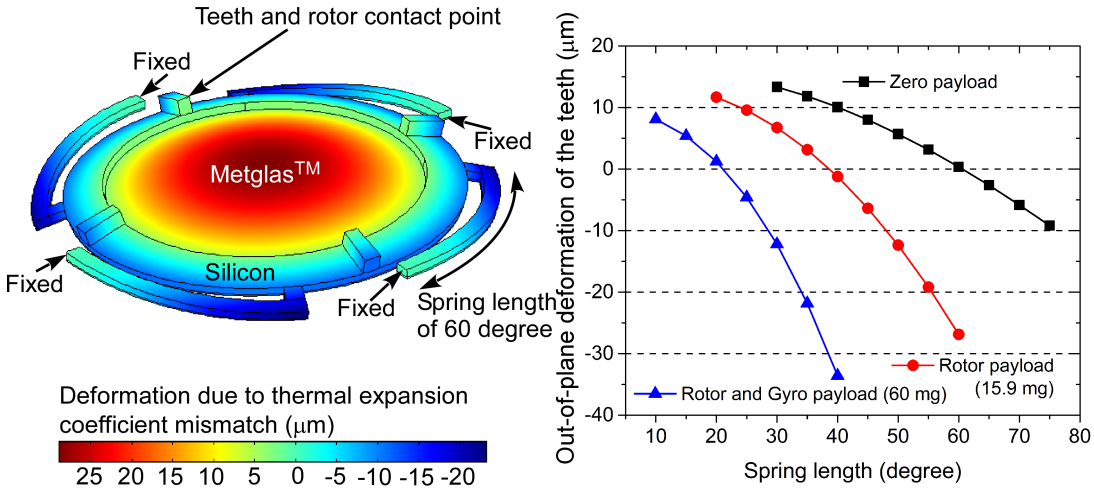

(a) (b)

Fig. 3-2: (a) FEA simulation result of deformation of the bilayer of silicon and magnetoelastic stator after bonding process. The flexible "crab-leg" springs allow "downward" deformation that compensates the "upward" deformation. (b) By changing the length of the "crab-leg" spring, a "zero" deformation of the teeth and rotor contact point can be achieved under different payloads.

The out-of-plane displacement of the teeth as a function of spring length is simulated when no payload is applied (Fig. 3-2 (b)). As expected, the displacement of the teeth changes from positive to negative values when the spring length increases. Thus, with proper design, it is theoretically possible to find a proper spring length that provides zero out-of-plane displacement of the teeth after bonding.

In this study, three payloads – corresponding to zero payload, the payload of the rotor, and the payload of the rotor and typical inertial sensors – are important for demonstration of the motor operation. Initial measurements can be carried out with zero payload; the real time rotational rate measurements can be carried out with only a rotor load (15.9 mg); finally, the motor needs to carry an inertial device for calibration, such as a gyroscope (60 mg). Utilizing similar methods, the preferred azimuthal spring lengths (resulting in a predicted zero tooth displacement after bonding and carrying the static

payload) for a 5 mm diameter stator are 21.5˚, 40˚ and 60˚ for payloads of 0 mg, 15.9 mg and 60 mg, respectively. These angles correspond to spring lengths of approximately 1.1 mm, 2.0 mm, and 2.9 mm.

3.1.1.2 Modal Analysis

FEA modal analysis was carried out for estimation of eigenfrequencies for the desired mode shapes of the standing wave stator. The crab-leg length of 21.5˚ and a silicon "ring" inner radius of 2 mm were used in the simulation. The deformation induced by thermal expansion coefficient mismatch was also included in the simulation model by using a pre-stressed eigenfrequency analysis in COMSOL multiphysics. The FEA simulation results showed that the eigenfrequencies of CCW mode and CW mode have an approximately linear relationship with the thickness of the silicon (Fig. 3-3).

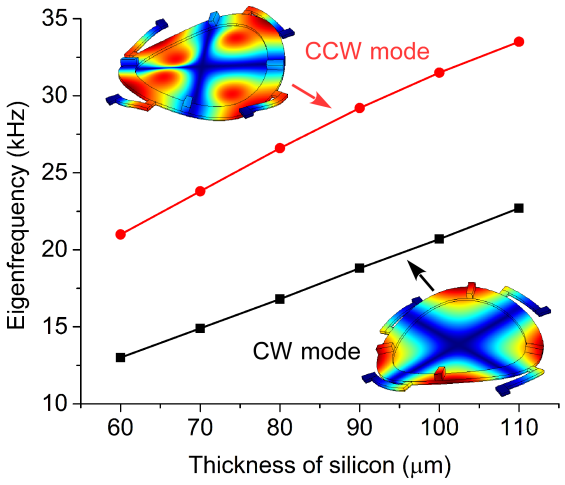

Fig. 3-3: FEA simulation result of eigenfrequencies of CW and CCW mode shapes as a function of thickness of the silicon.

3.1.2 Traveling Wave Motor Design

3.1.2.1 Concept

A traveling wave is initiated through an appropriate combination of two standing waves. These two standing waves are ideally at the same frequency and have a +/-π/2

phase difference both in time and in space. In order to excite the two standing waves with a spatial and temporal phase difference, two input excitation signals are required. These signals should be directed along lines of symmetry of the structure at which the antinodes of the two standing waves are generated. In order to achieve this, 8 "crab-leg" springs were used to provide a symmetrical structure so that two standing waves with 4 antinodes located at the connection between the spring and the "ring" will have mode shapes with a π/2 spatial phase difference (Fig.3-4 (a-b)).

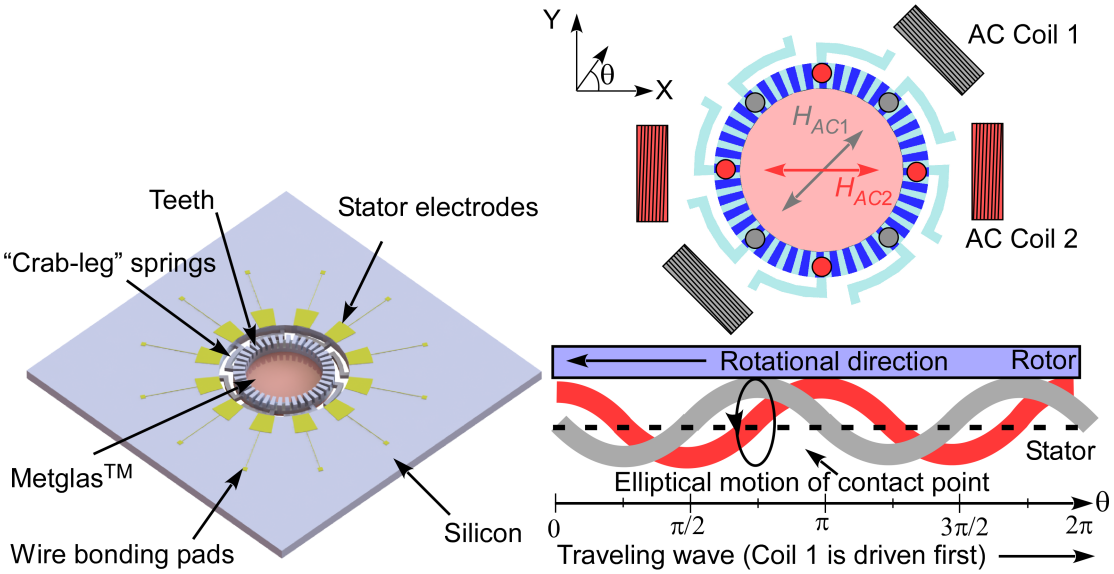

(a) (b)

Fig. 3-4: (a) 3D schematic of traveling wave stator with symmetrical springs suspensions. (b) 2D schematic of working principle of the traveling wave, which is generated as a combination of two standing waves with a π/2 spatial phase difference. These two standing waves are driven by AC magnetic fields with a π/2 phase difference in time.

In the traveling wave, the contact point between the rotor and the stator undergoes an elliptical motion that has an opposite direction compared to that of the traveling wave. The bidirectional rotation can be realized by changing the excitation order of each standing wave. As shown in Fig. 3-4(b), assuming two standing waves have the same out-of-plane amplitude and π/2 spatial difference in mode shapes, the two standing waves along the edge of the stator can be illustrated as a gray-colored wave and a red-colored

wave (excited at a π/2 temporal and spatial phase separation). The mathematical expressions describing the gray and red standing waves are given as:

$$A\sin(2\theta)\sin(\omega t) \tag{3-1}$$

$$A\cos(2\theta)\sin(\omega t - \pi/2) \tag{3-2}$$

The combination of these two standing waves is a traveling wave:

$$A\cos(2\theta - \omega t) \tag{3-3}$$

Thus, the peak of the wave occurs at $\theta = \omega t/2$, and the traveling wave moves in a positive direction. This results in a rotation in the negative direction due to the elliptical movement of the teeth. If instead the gray-colored wave is excited with a π/2 phase delay in time, the traveling wave is expressed as:

$$A\cos(2\theta + \omega t) \tag{3-4}$$

Accordingly, the peak of the wave occurs at $\theta = -\omega t/2$, and the wave traveling direction and the rotation direction reverses.

3.1.2.2 Modal Analysis

Modal analysis was carried out for estimation of eigenfrequencies with the desired mode shapes of the traveling wave stator. The FEA simulation results showed two desired mode shapes exist at 33.8 kHz and 34.4 kHz, respectively. The two mode shapes have a spatial phase difference of π/2, which means the antinodes of Mode 1 became the nodes of Mode 2, and vice versa. In the FEA simulation, the anisotropic material properties of silicon resulted in a Δf of 0.6 kHz between two mode shapes. Ideally, the mode shapes would have no frequency split (Δf of 0 Hz), but a small frequency split can be managed in practice as described later.

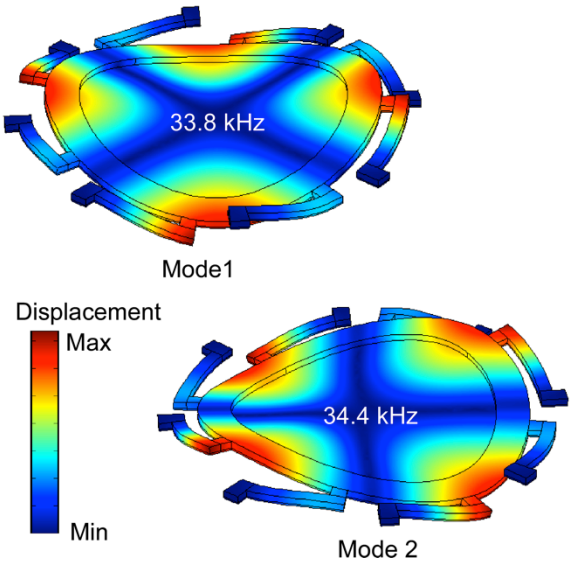

Fig. 3-5: The FEA simulation results of eigenfrequencies of two desired mode shapes with a $\pi/2$ spatial phase difference.

3.1.3 Capacitive Sensing Electrodes

3.1.3.1 Concept

Both standing wave motors and traveling wave motors include capacitive sensing electrodes for real time measurement of the rotational rate. For the capacitive sensing architecture, floating electrodes are implemented to avoid leads connecting the stator and rotor layers. The sensing capacitor consists of a pair of two stator electrodes (V^+ and V^-) and a pair of two rotor electrodes connected to each other (Fig. 3-6). The capacitance is approximately linearly related to the overlap area between the rotor electrodes and stator electrodes. The capacitance reaches a maximum when a pair of rotor electrodes is perfectly overlapping a pair of stator electrodes, as shown in Fig. 3-6. Thus, ideally, the capacitance across these electrodes should result in a triangle waveform during the rotation of the rotor, with the peak occurring when the electrodes are exactly overlapped. This information would then be used to reconstruct the rotor position and velocity during rotation.

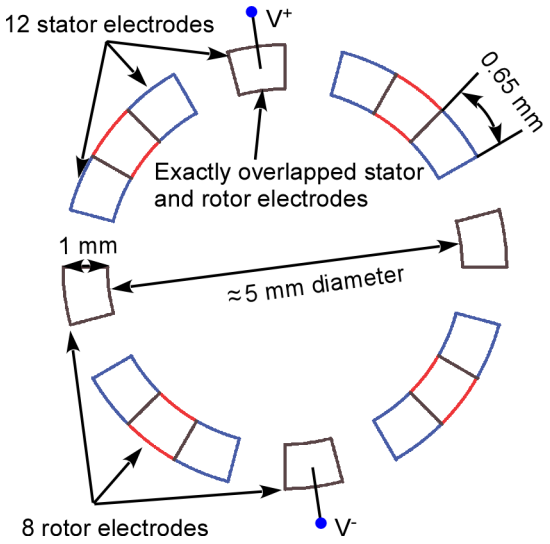

Fig. 3-6: Schematic of rotor and stator electrode positions when measuring capacitance reaches maximum.

3.1.3.1 Modeling

This detection scheme can be sensitive to parasitic capacitances, which, if large, could result in an obscured sensing capacitance or in undesired cross-talk between electrode pairs. To evaluate the relative size of the measured and parasitic capacitances, and the effect of the parasitic capacitances on the measured electrodes, a model is developed. The geometry of the model is established based on the geometry of the electrodes and the anticipated sensing gap. The modeled stator and rotor are oriented such that one pair of the rotor electrodes and the targeted pair of stator electrodes are fully overlapped, resulting in a maximum capacitance (Fig. 3-7). Consequently, along the clockwise path, the second rotor electrode set is misaligned with the stator electrodes underneath it, resulting in two very small fringe capacitors (Fig. 3-6). The third rotor electrode set fully overlaps with the above stator electrode set. The corresponding equivalent circuit is developed and simulated.

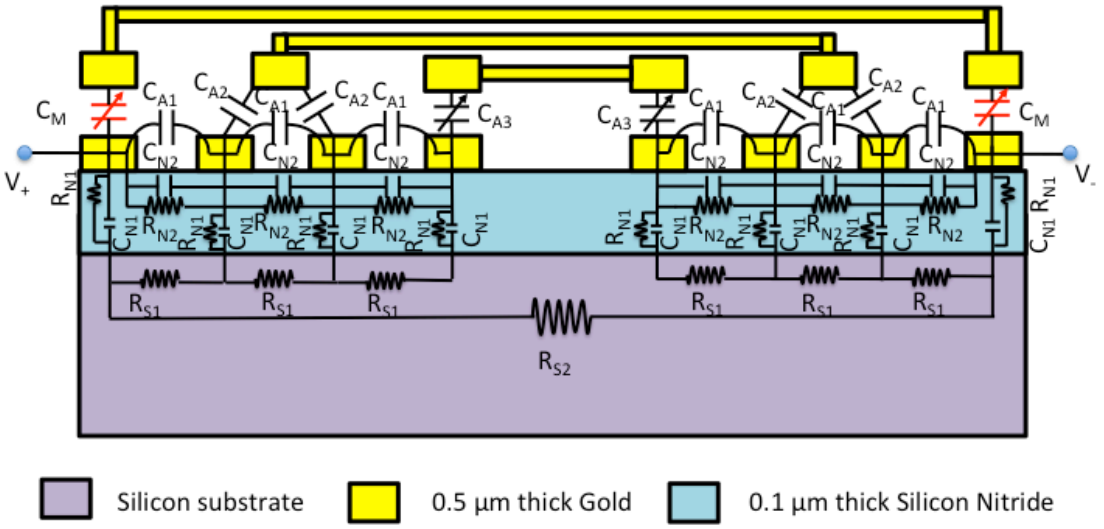

Fig. 3-7: An equivalent circuit model of the capacitive sensing components.

The equivalent circuit, as shown in Fig. 3-8, is established based on the model provided in Fig. 3-7. The definitions and estimates of each capacitor and each resistor are given in Table 3-1. The values of capacitance and resistance are estimated using practical fabrication parameters and the following standard equations:

$$C = \frac{\varepsilon_0 \varepsilon_r A_C}{d} \tag{3-4}$$

$$R = \frac{\rho l}{A_R} \tag{3-5}$$

where ε_0 is the permittivity of free space, ε_r is the relative permittivity of the intervening material, A_C is the area of the capacitive electrodes, ρ is the resistivity of the material forming the resistor, l is the length of the resistor, and A_R is the cross-sectional area of the resistor.

The equivalent circuit was built and simulated using PSPICE software Capture CIS. For comparison, the ideal circuit model simply included a measuring capacitor and a wire resistor, as shown in Fig. 3-8. Then, the ideal equivalent circuit was replaced by an equivalent circuit including all the parasitic capacitors and resistors, as shown in Fig.

3-9. The latter complicated equivalent circuit was then connected to the same external measurement circuit.

Table 3-1. Parameter definitions and estimated values.

C_M	Measuring capacitor consists of a rotor electrode and a stator electrode, with 10 μm air gap, and 0.8 mm^2 area (fully overlapped area). Estimated capacitance is 0.7 pF.
C_{N1}	Parasitic capacitor between the stator electrode and the silicon substrate, with 0.1 μm silicon nitride gap, and 0.8 mm^2 area. Estimated capacitance is 525 pF.
C_{N2}	Parasitic capacitor between two adjacent stator electrodes through ≈1.3 mm longitudinal silicon nitride gap, and 0.8 mm^2 area. Estimated capacitance is 0.04 pF.
R_{S1}	Silicon resistor across two adjacent stator electrodes with length of ≈1.3 mm and cross-section of ≈1 mm^2. Estimated resistance is 10^6 Ω.
R_{S2}	Silicon resistor across two furthest stator electrodes (connected to measurement circuit) with length of ≈10 mm and cross-section of ≈1 mm^2. Estimated resistance is 10^7 Ω.
R_{N1}	Vertical nitride resistor between the stator electrode and the silicon substrate, with 0.1 μm silicon nitride long, and 0.8 mm^2 cross-section area. Estimated resistance is 10^{15} Ω.
R_{N2}	Longitudinal nitride resistor between two adjacent stator electrodes with nitride length of ≈1.3 mm and cross-section of ≈1 mm^2. Estimated resistance is 10^{19} Ω.
C_{A1}	Capacitor between the stator electrodes through ≈1.3 mm longitudinal air gap, and 0.8 mm^2 area. Estimated capacitance is 0.0054 pF.
C_{A2}	Capacitor between a rotor electrode and a stator electrode with no overlapped area (only fringe effect is considered). The gap is 10 μm of air, and the effective capacitance is calculated to be 0.075 pF by using FEA.
C_{A3}	Capacitor consists of a rotor electrode and a stator electrode, with 10 μm air gap, and 0.8 mm^2 area (fully overlapped area). Estimated capacitance is 0.7 pF. This value is same as the measuring capacitance.

The external measurement circuit mainly included four components: a power source, a first amplifier stage, a signal mixer, and a second amplifier stage. The power source provides a square wave with frequency of 100 kHz and peak value of 3 V. The first amplifier stage served as a high pass filter. The mixer was used to obtain the absolute value of the output signal. The second amplifier stage was a low pass filter.

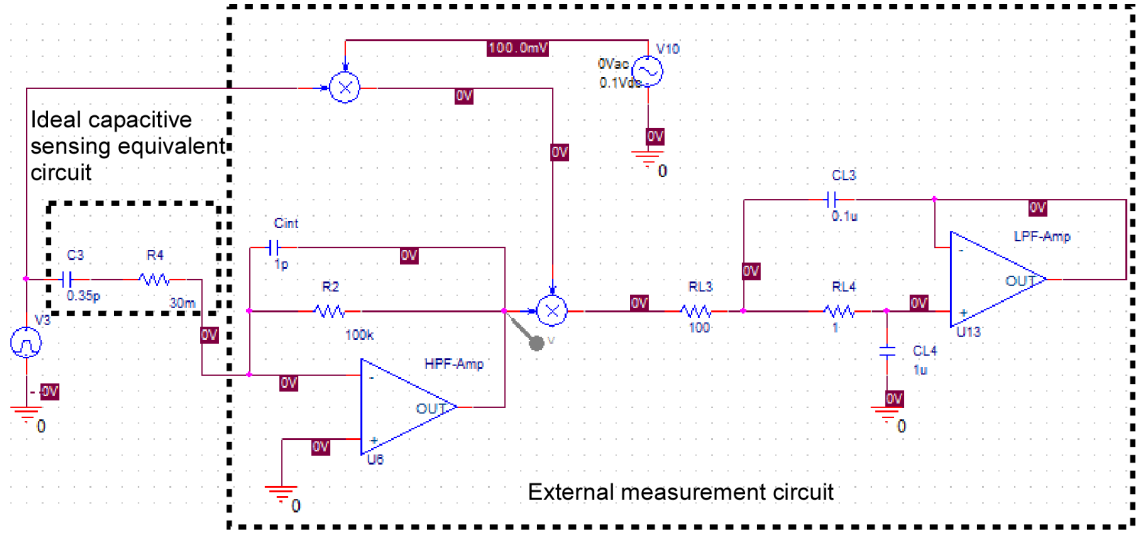

Fig. 3-8: An ideal equivalent capacitive sensing circuit model for the magnetoelastic motor and the external measurement circuit.

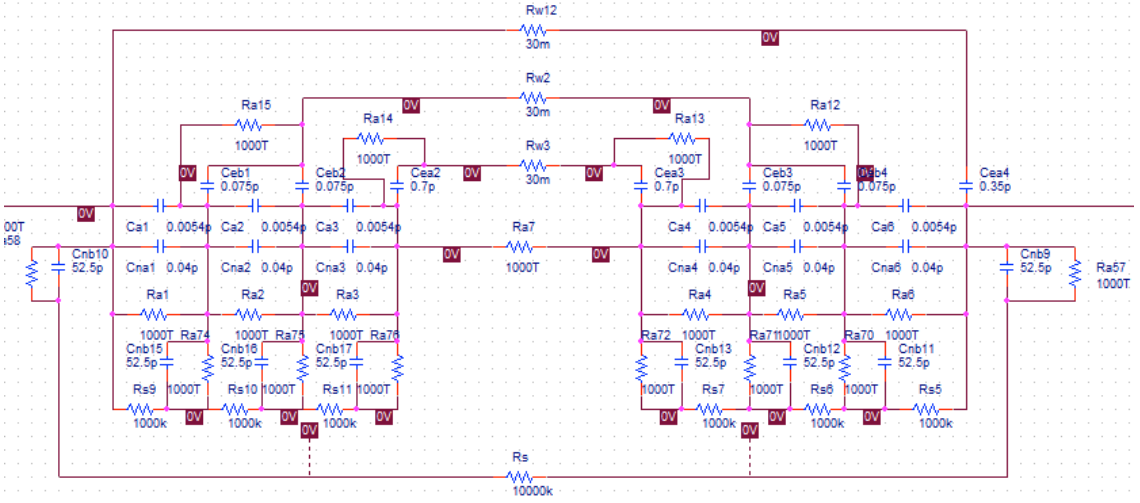

Fig. 3-9: An equivalent capacitive sensing circuit for magnetoelastic motor including the parasitic resistors and capacitors.

The output waves of two modeled circuits were compared (Fig. 3-10). The measuring capacitance is directly related to integration of the area of the decaying wave. According to the simulation results, there is a DC offset induced by the parasitic resistance and capacitance. However, this offset can be subtracted in post-processing of the data. Thus, the modeling indicates that parasitic capacitances will not present a practical limitation of the measurement scheme.

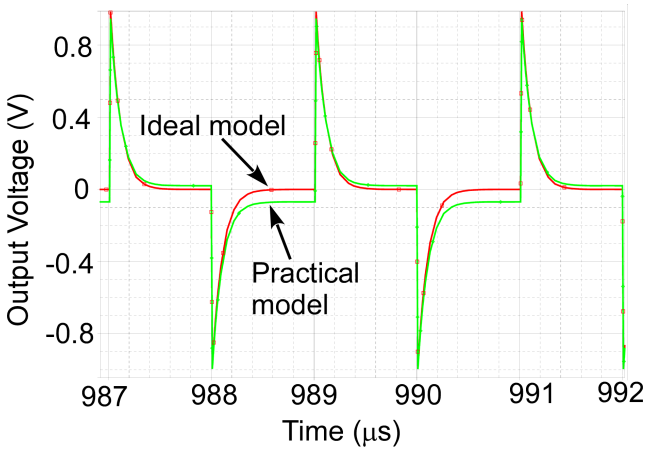

Fig. 3-10: Simulated transient response of the signal output for the ideal model (red) and the model (green) with parasitic parameters.

3.2 Fabrication

3.2.1 Process Flow

The second-generation motor is fabricated using a four mask process, as shown in Fig. 3-11. The process is developed based on the process used for first-generation motor. In addition, the fabrication process for the second-generation motor includes another DRIE step for defining the electrode gap, metal coating and patterning steps for capacitive sensing electrodes, as well as a XeF_2 etching step for removal of the residual silicon sidewalls resulting from the final DRIE step (Fig. 3-11(i)). For the second-generation motor, a more "anisotropic" DRIE with a well-balanced etch time and passivation time of each cycle of the BOSCH process is necessary to achieve intact profiles of the silicon springs and the "ring" structures. However, this more "anisotropic" DRIE induces thin silicon sidewalls resulting from the passivation layers – at locations with a height difference – as a DRIE mask. Thus, a XeF_2 etching step is used to quickly remove these thin residual silicon sidewalls without significantly attacking other structures. The first-generation motor did not have this issue because of its large feature size that allows using a less "anisotropic" DRIE with a large portion of etch time

compared to the passivation time. The full details of the fabrication processes are as follows.

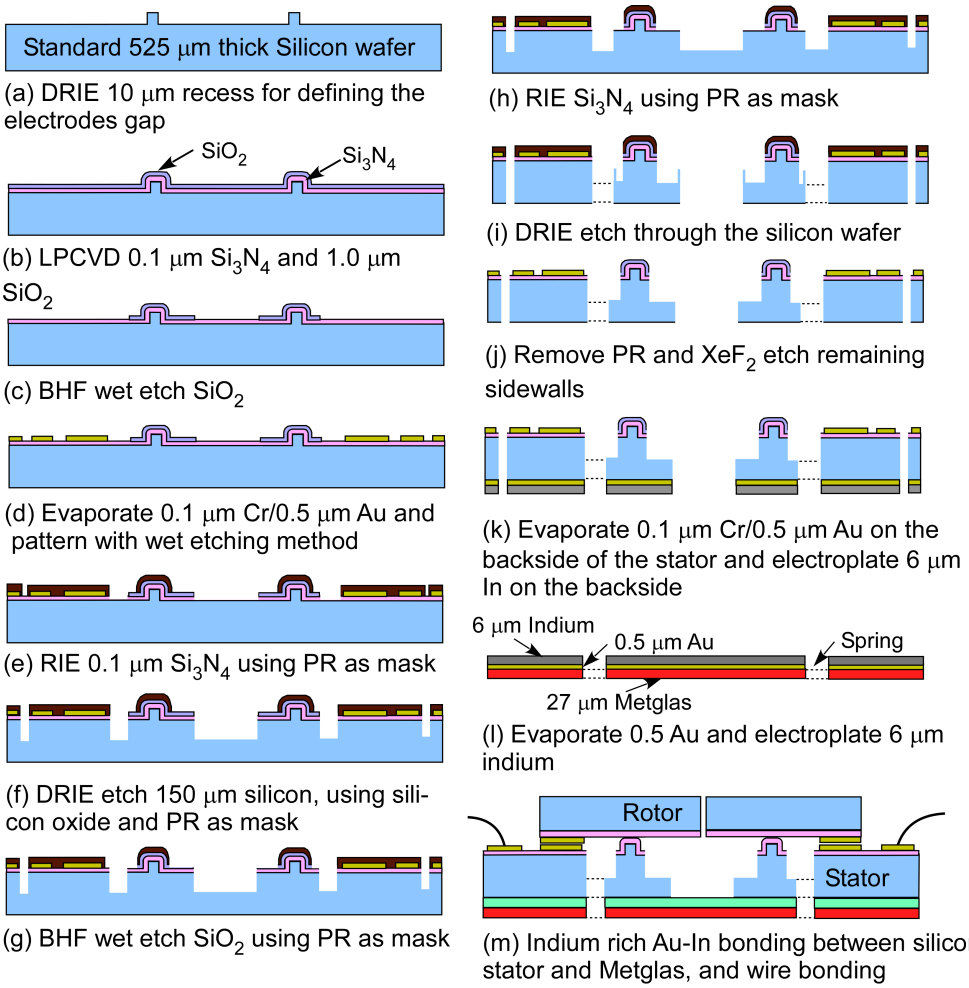

Fig. 3-11: Process flow for second-generation motor: (a) DRIE 10 μm (Mask 1); (b) Deposit 0.1 μm Si_3N_4 and 1 μm high temperature SiO_2 (HTO) using low-pressure chemical vapor deposition (LPCVD); (c) Wet etch HTO using buffered hydrofluoric acid (Mask 2); (d) Wet etch evaporated 0.1 μm thick Cr and 0.5 μm thick Au (Mask 3); (e) Reactive-ion etch (RIE) Si_3N_4 (Mask 4); (f) Deep reactive-ion etch (DRIE) 150 μm depth of silicon; (g) Wet etch HTO using BHF; (h) RIE Si_3N_4; (i) DRIE etch through silicon; (j) Remove PR and XeF_2 etch residual silicon sidewalls resulting from DRIE step; (k) Evaporated 0.1 μm Cr and 0.5 μm Au, and electroplate 6 μm indium layer for Au-In bonding; (l) Evaporated 0.1 μm thick Cr and thick 0.5 μm Au on PCM'd Metglas pieces; (m) Indium rich Au-In bonding and wire bonding.

The process starts with a standard silicon wafer with ≈525 μm thickness. The first step is to DRIE a 10 μm recess for defining of a gap between the stator electrodes and the rotor electrodes (Mask 1). An isolation layer of 0.1 μm thick silicon nitride and 1

μm thick silicon oxide (HTO) are deposited using LPCVD. The HTO is then wet etched using BHF (Mask 2). This is followed by an evaporation of 0.1 μm thick Cr and 0.5 μm thick Au for the electrodes. The metal layers are wet etched (Mask 3). A thick PR layer of ≈8 μm is coated and patterned (Mask 4). Then, 150 μm thick silicon is DRIE etched using PR and silicon oxide as the mask. The exposed silicon oxide is BHF wet etched and silicon nitride is etched using RIE. The last DRIE process is used to etch through the wafer and release the stator. After that, the PR is stripped. Another Cr/Au (0.1μm/0.5 μm) seed layer is evaporated on backside of the silicon wafer. An indium layer with thickness of ≈6 μm is electroplated on the backside of the silicon wafer for the indium rich Au-In bonding. This completes the fabrication of the silicon parts.

A Metglas™ 2826MB sheet is PCM'd into pieces with the same geometry as the silicon parts. These pieces are also coated with a Cr/Au (0.1μm/0.5 μm) layer via evaporation as required for the bonding. For the bonding process, about 1 MPa pressure is applied between the silicon parts and the Metglas™ pieces after manual alignment of the components under a microscope. The indium rich Au-In bonding is conducted in a vacuum oven (≈50 mTorr) at 200 ˚C for 1 hour, plus 30 minutes of ramping to the bonding temperature and several hours of cooling. The more detailed description of each fabrication process is given in Appendix C.

3.2.2 Fabrication Results

Typical optical and SEM images of the fabricated second-generation standing wave motors and traveling wave motors are given in Fig. 3-12, 13. The SEM images show a bilayer of silicon and Metglas™ with a good alignment after bonding. The profile of the fabricated motor is measured optically using a LEXT interferometer (Olympus Corporation, PA, USA), as shown in Fig. 14. The measurements show that the

height differences between the teeth and the stator frames are 14 µm, 22 µm and 25 µm for stators with spring lengths of 21.5˚, 40˚ and 60˚, respectively. Considering a pre-defined 10 µm height difference, the bonding induced out-of-plane displacements of the teeth are 4 µm, 12 µm and 15 µm, in good agreement with the FEA simulated displacements of the teeth – 0 µm, 10 µm and 15 µm – for the three spring length designs, as described in section 3.1.1.1. The thickness of the silicon is also measured to be ≈70 µm.

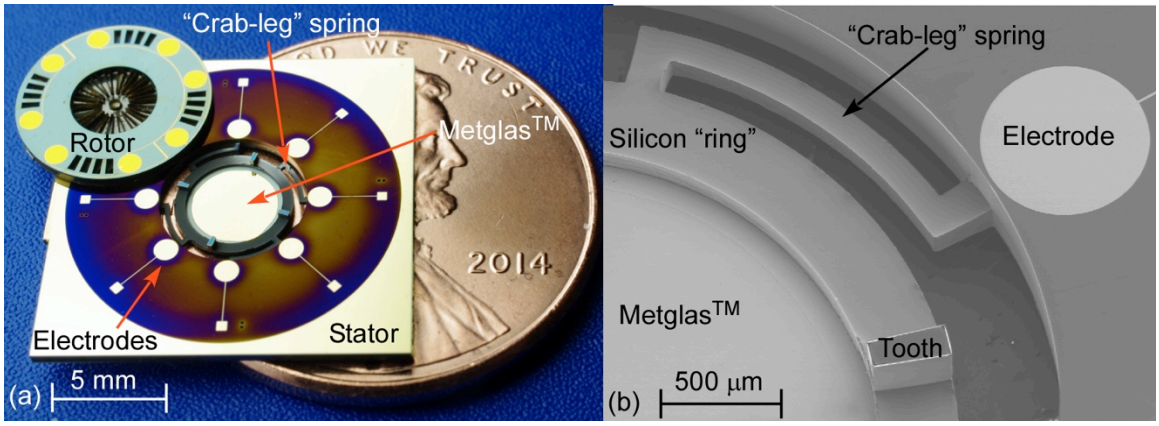

Fig. 3-12: Optical and SEM images of standing wave motor.

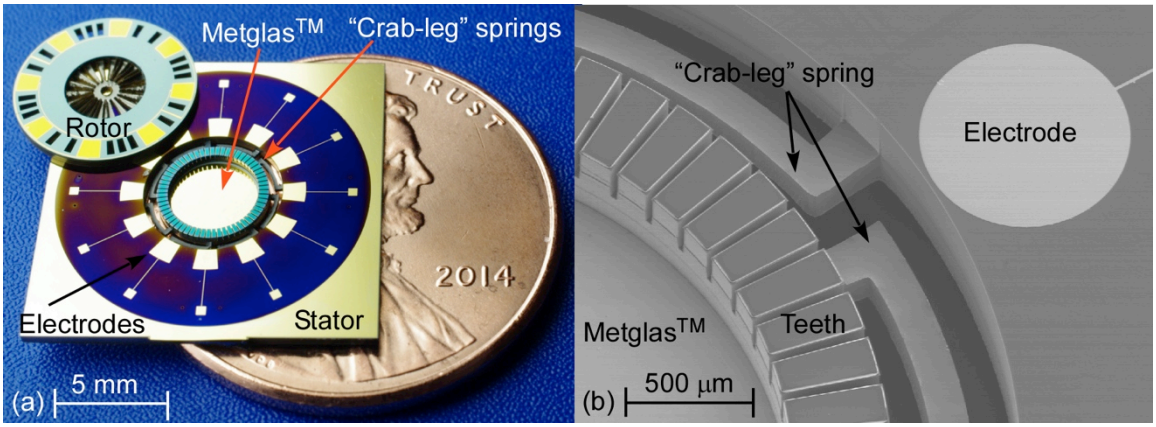

Fig. 3-13: Optical and SEM images of traveling wave motor.

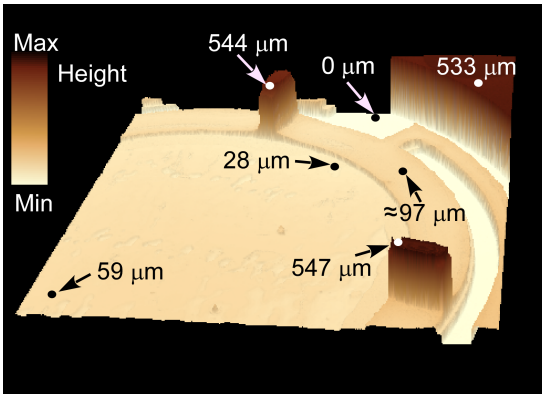

Fig. 3-14: Surface profile of a standing wave stator with 60˚ spring length, after the bonding process.

3.3 Experimental methods and results

3.3.1 Experimental Methods

The resonant responses of the stators were characterized using a laser vibrometer, while the mode shapes were confirmed by examining the displacement amplitudes of points along the rim of the "ring" stator. Similar to the first-generation motors, the second-generation motors were actuated by a combination of a DC and AC magnetic field. Two layers of miniaturized coils are used for providing two sets of DC and AC magnetic fields with 45 degree azimuthal separation, as required for the traveling wave motor actuation (Fig. 15(a)). Each layer consists of AC Helmholtz coils with 30 turns for each coil and a DC coil with 110 turns. All coils are wound with 36 AWG insulated magnet wire. The cores on which the coils are wound are each 6 layers of 100 μm thick 1018 low carbon steel, bonded together with polymeric adhesive. The magnetic field direction of a given layer of miniaturized coils is defined as along the long axis of the two extensions in the center of the layer. The tips of these extensions are about 6 mm apart. The extensions are bent upward out of plane slightly so that the strongest magnetic field

is in the plane of the magnetoelastic portion of the stator, which is placed on top of the coils.

The motors are assembled under a microscope. The stator is stacked on top of the miniaturized coils and the rotor rests on the stator. An adjustable probe stage is used to apply preload and to center the rotor on the stator during rotation.

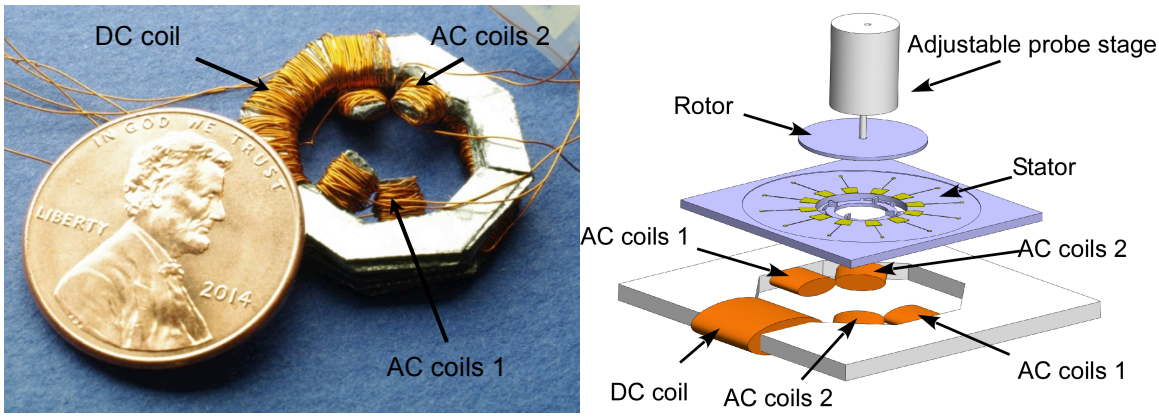

(a) (b)

Fig. 3-15: (a) Two stacked layers of miniaturized coils providing DC and AC magnetic field with 45 degree azimuthal separation, as required for traveling wave actuation. (b) 3D schematic of the assembly method for the second-generation motor.

3.3.2 Standing Wave Stator

The CW mode and CCW mode of second-generation stator were confirmed to exist at resonant frequencies of 12.1 kHz and 22.4 kHz respectively. Out-of-plane deflection amplitudes of 0.44 μm and 0.4 μm, respectively, existed near the antinodes (Fig. 3-16) of the modes when a ≈2 Oe amplitude AC magnetic field and a ≈6.5 Oe DC magnetic bias field were applied. The experimental results were similar to FEA simulation results eigenfrequencies of 15 kHz and 24.5 kHz for the CW mode and CCW mode, respectively, as described in section 3.1.1.2. The measured quality factors for the CW mode and CCW were 107 and 250, respectively.

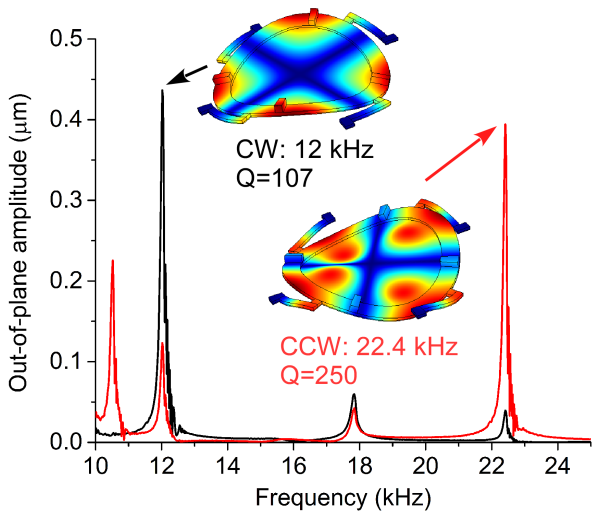

Fig. 3-16: Experimentally measured frequency response of a standing wave stator (≈70 μm thick) with no load, in response to a 6.5 Oe DC and a 2 Oe amplitude AC magnetic fields. The traces are measured while the interrogating fields are azimuthally aligned with the measured antinode.

3.3.3 Traveling Wave Stator

3.3.3.1 Frequency Response

The experimental results confirm that two desired mode shapes with π/2 spatial phase shift exist at frequencies of 28.4 kHz and 29.9 kHz, with out-of-plane deflection of 74 nm and 70 nm at the antinodes, respectively. For these measurements, an AC magnetic field with ≈6 Oe amplitude and a DC magnetic bias field of ≈3 Oe were applied along one antinodal diameter of the measured mode shape (Fig. 3-17). The quality factors for the two modes are 630 and 665, respectively. For the traveling wave stator, although the two mode shapes ideally should have an identical resonant frequency, it was expected that a Δf between two mode shapes would exist. This Δf resulted from anisotropic material properties of silicon (as demonstrated by FEA simulation that was described 3.1.2.2), non-symmetrical geometry from fabrication, small misalignment between the silicon and the Metglas™, non-uniform driving magnetic fields, and other factors. Because of this Δf, careful consideration of the driving approach is required.

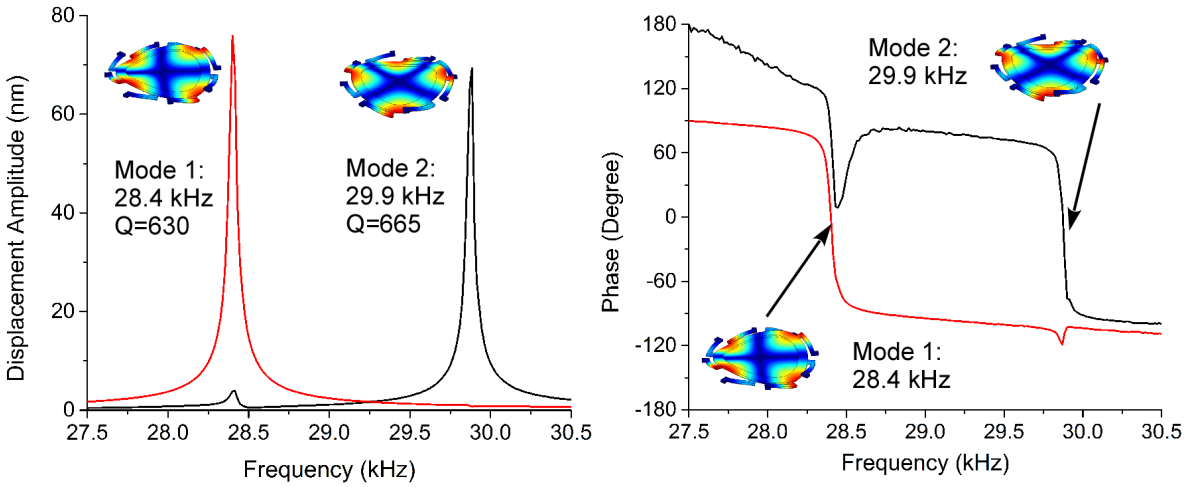

Fig. 3-17: Experimentally measured frequency response of a traveling wave stator (≈70 μm thick silicon) with no load, in response to a 3 Oe DC magnetic field and a 6 Oe amplitude AC magnetic field. The traces are measured while the interrogating fields are azimuthally aligned with the measured antinode.

3.3.3.2 Resonant Frequency Tuning

Initial experiments were carried out for reducing the frequency split. The resonant frequency of mode 2 was reduced by adding small amount of mass on the backside of the stator at antinodes locations. A total of ≈2 mg added mass consisted of four tungsten rods with diameter of 125 μm and length of 1 mm and the epoxy applied for attachment. As a result, the resonant frequency of mode 2 shifted from 29.9 kHz to 28.33 kHz, and the quality factors of mode 1 and 2 reduced to 450 and 300, as shown in Fig. 18. The frequency split was successfully reduced to 0.04 kHz. Near the resonant frequencies, the phases of the responses are separated by approximately 10˚; if no frequency split existed, the two responses would have zero phase separation.

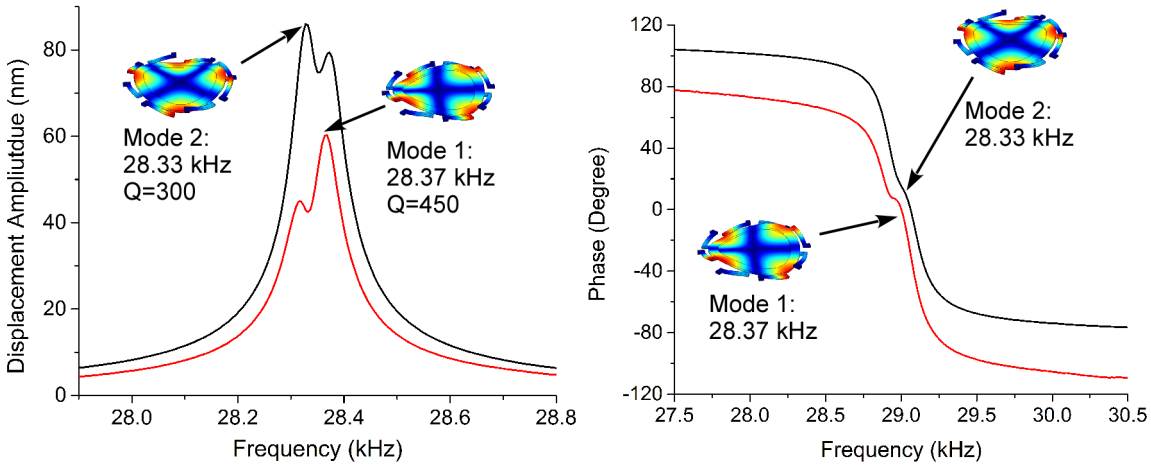

Fig. 3-18: Experimentally measured frequency response of a traveling wave stator (≈70 μm thick) with added mass (≈2 mg total) at the four antinodes of Mode 2, in response to a 3 Oe DC magnetic field and a 6 Oe amplitude AC magnetic field. The traces are measured while the interrogating fields are azimuthally aligned with the measured antinode.

3.3.3.3 Time Domain Response

In order to confirm the formation of the traveling waves in the stator, the time domain responses of the displacements of three points located between the antinodes of the two mode shapes were measured using an LDV (Fig. 3-19). During the measurement, the driving current was used as a time reference for synchronizing the LDV data for the three separately measured points.

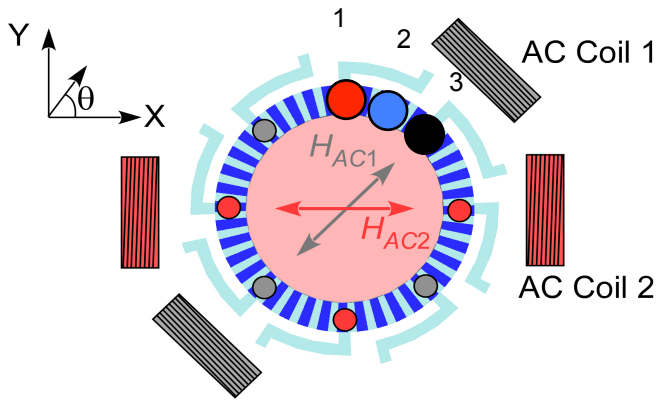

Fig. 3-19: Schematic of locations of three monitoring points.

First, the responses of the traveling wave stator with 1.5 kHz frequency split were obtained when the two mode shapes were driven by two AC magnetic fields (with 7.2 Gauss AC magnetic field amplitude at corresponding resonant frequencies of two mode shapes) with 90 degree phase difference, as shown in Fig. 3-20. A DC bias field of 3 Oe was applied along X-axis direction (Fig. 2-19) during these tests. Fig. 3-20 (a) shows that the amplitudes of displacement at the three points began to overlap from 0.4 millisecond to 0.6 millisecond, indicating the switch of the traveling wave direction. Fig. 3-20 (b) shows the crest of the wave travels in one direction (from point 1 to point 2, and then to point 3) over a time period of about 0.25 millisecond. A proper control system, which only energizes the vibration when the desired wave direction is occurring, would be required to achieve rotation in one direction with a stator exhibiting a resonant frequency split of 1.5 kHz.

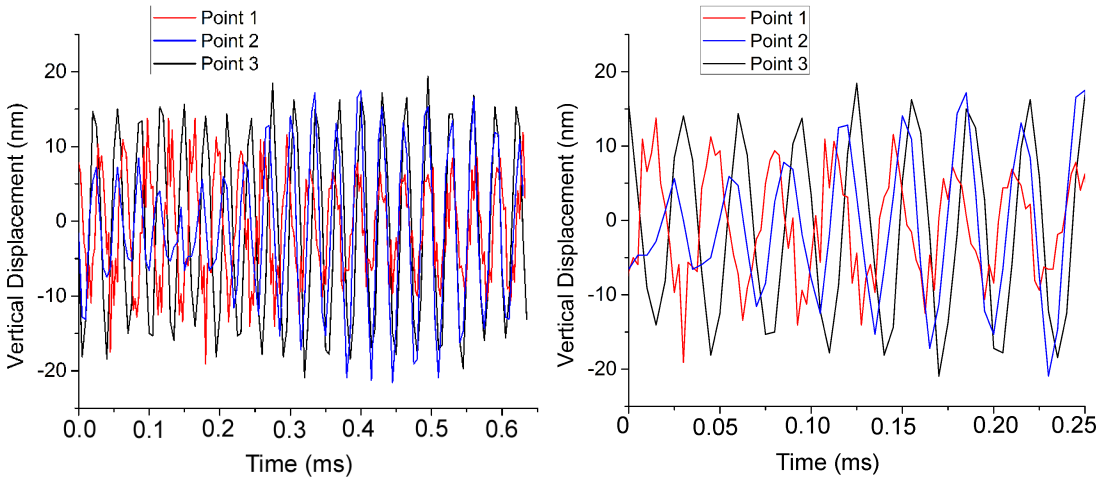

Fig. 3-20: LDV measured vertical displacement of monitoring points in the time domain. (a) Evidence of slowing and switching of the traveling wave direction. (b) Evidence of a traveling wave in one direction for short period of time.

Another approach for achieving a unidirectional traveling wave is to reduce the frequency split by tuning the resonant frequencies. As mentioned above, the frequency split was reduced to 0.04 kHz after adding mass at the locations of the antinodes of the

mode that had the higher as-fabricated resonant frequency. Thus, similar time domain responses of three points were obtained, when the two mode shapes were driven by two AC magnetic fields (with 5.1 Gauss and 7.2 Gauss AC magnetic field amplitudes for driving mode 1 and 2, respectively) with the same frequency of 28.435 kHz, and 100˚ phase difference. The maximum displacements occurred in a sequence from point 3 to point 2 and to point 1, confirming that the traveling wave was propagating in one direction (Fig. 3-21). A phase difference of 100˚, instead of 90˚, was used between the two driving AC magnetic fields because the extra 10˚ phase difference in the frequency responses for the two mode shapes at the driving frequency needs to be included, as suggested in Fig. 3-18.

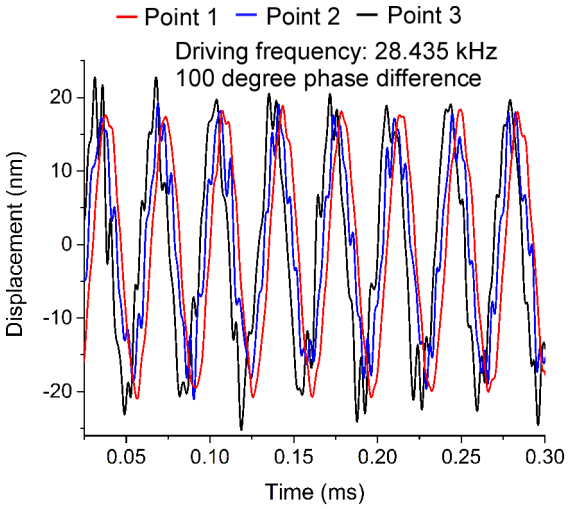

Fig. 3-21: LDV measured vertical displacement of three monitoring points after the frequency split was tuned to be 0.04 kHz.

3.3.4 Stationary Capacitance Measurement

The value of the capacitance between the sensing electrodes was measured while the rotor and stator were oriented in different positions (Fig. 3-22). The orientation of the positions was defined by the angle between a pair of rotor electrodes and the stator electrodes being measured. The capacitance was measured using an Agilent 4284A LCR

meter (Agilent Technologies, CA, USA), with a measurement frequency of 100 kHz, an applied voltage of 1 V and a measurement mode of C_p-D, while the stator electrodes were probed with a typical semiconductor probe station. An angle of 0˚ signifies that the rotor electrode pair is exactly aligned with the stator electrode pair. For the measured design, which uses the circular electrode geometry (as shown in Fig. 3-12 (a)), there is no overlap area when the angle is larger than ≈7.9˚. The differential capacitance ΔC was measured by subtracting the capacitance measured with the rotor on the top of the stator from the capacitance measured without a rotor on top of the stator. As expected from theory, the measured ΔC is maximum when the electrodes are aligned and decreases non-linearly as the angle between the electrodes increases. The theoretical curve was generated by the ratio of the overlap area of the rotor and the stator circular electrodes to its maximum value (exact overlap), superposed with the FEA calculated fringe capacitance as` used in the model of section 3.1.3.1 (0.075 pF).

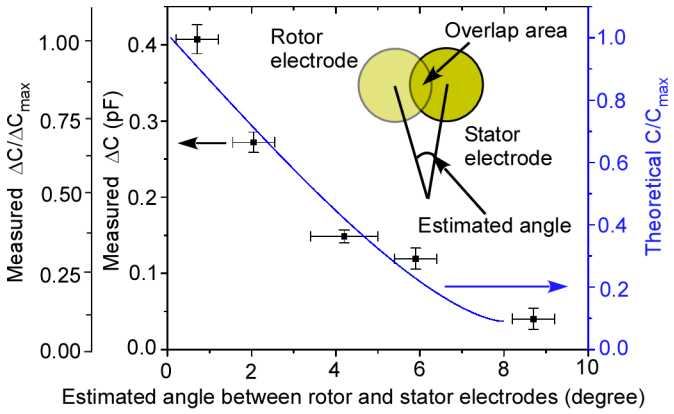

Fig. 3-22: Measured and theoretical stationary differential capacitance due to the rotor electrodes at different positions with respect to the stator electrodes.

3.4 Summary and Discussion

The intent of the second-generation motor design was to implement capacitive sensing electrodes while providing control over the capacitive gap, and to investigate the feasibility of a traveling wave motor. This chapter has presented the analysis, fabrication, and experimental results of wirelessly actuated, chip-scale standing wave and traveling wave magnetoelastic rotary motors with integrated capacitive sensing electrodes.

The capacitive sensing architecture was integrated in both standing wave and traveling wave motors. The floating electrode design allowed avoiding leads that connect to rotor. The initial tests of fabricated devices demonstrated an ability to control the sensing capacitor gaps between the rotor electrodes and the stator electrodes through design of the "crab-leg" stator suspension and compensation of the thermal expansion mismatch of the silicon and magnetoelastic layers. The stationary differential capacitance of the sensing electrodes was successfully measured as a function of the relative positions between the rotor and the stator. The real time rotational rate measurement under investigation could provide useful data for many applications, such using the measured rotation for an in-situ calibration of a gyroscope.

The second-generation designs also investigated the practical generation of traveling waves in a magnetoelastic resonant motor. Two mode shapes, spatially offset by 45º (half of a wavelength for these mode shapes), were identified in the fabricated devices. If driven by oscillating magnetic fields that are offset by $\pi/2$ in phase, a traveling wave should be generated. However, due to the anisotropic material properties of the stator, misalignment between the silicon and Metglas™ layers, and other factors, a 1.5 kHz frequency split existed between the modes. This frequency split results in a continuously switching of the direction of the traveling wave and compromises the traveling wave performance. The frequency split was successfully reduced to 0.04 kHz

by adding a total of ≈2 mg mass at the antinodes of the mode shape with the initially higher resonant frequency. This reduction in frequency split allowed the generation of a traveling wave with a consistent direction. This study represents the first measurements of magnetoelastically-generated traveling waves at this scale.

Chapter 4

Scalable, High-Performance Magnetoelastic Tags Using Frame-Suspended Hexagonal Resonators

This chapter[2] presents the analysis, design and experimental evaluation of miniaturized magnetoelastic tags using frame-suspended hexagonal resonators. Magnetoelastic tags – also known as acousto-magnetic or magnetomechanical tags – are used in wireless detection systems – for example, electronic article surveillance and location mapping systems – that electromagnetically query the resonant response of the tags. In order to obtain a strong resonant response for miniaturized tags, a frame-suspended configuration is utilized to diminish the interaction between the vibrating portion of the tag and the substrate. The signal strength can be boosted by utilizing signal superposition with arrayed or clustered magnetoelastic tags. The hexagonal tags with a diameter of 1.3 mm are batch fabricated by photochemical machining from 27 μm thick Metglas™ 2826MB. A preferred DC magnetic field bias for these tags is experimentally determined to be ≈31.5 Oe. A single frame-suspended magnetoelastic tag shows quality factors of 100-200. This design provides ≈75X improvement in signal amplitude compared to the non-linear signal superposition of the response has been experimentally measured for sets of frame-suspended tags that include as many as 500 units. Across 10 individual frame-suspended tags, the average resonant frequency is 2.13 MHz with a standard deviation of 0.44%, illustrating that this fabrication method provides repeatability.

[2] Contents presented in journal paper form in [Tan14] and in patent form in [Gia14].

4.1 Design

4.1.1 Concept

A typical magnetoelastic tagging system includes a transmit coil, a receive coil, magnetoelastic tags and DC bias magnets, as shown in Fig. 4-1. In the presence of a DC magnetic field, the magnetoelastic tags can be resonated by an applied AC magnetic field provided by a transmit coil. The magnetic flux resulting from the vibration can be detected inductively by a remotely positioned receive coil. The DC bias can be generated electromagnetically or provided by magnets packaged alongside the tags.

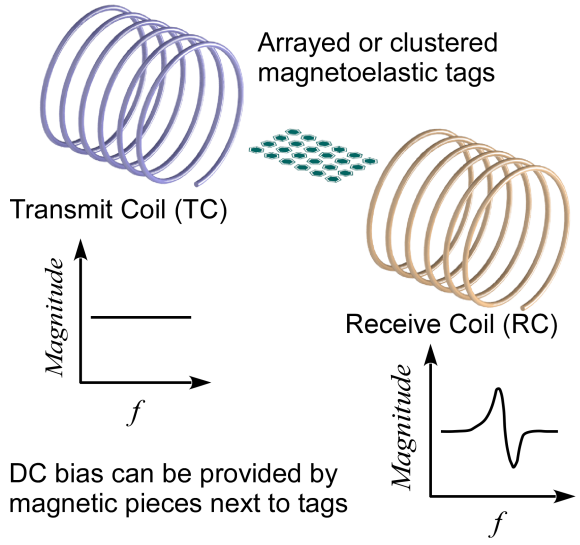

Fig. 4-1: Magnetoelastic tags resonate under an applied AC magnetic field generated by a transmit coil. The magnetic field resulting from the resonant vibration is detected by a receive coil, indicating the presence of the tags.

Magnetoelastic tagging systems are not limited to this configuration. The interrogating and detecting approaches can both be different for a variety of applications. For example, a pulsed signal – rather than a continuous wave signal – can be used for the interrogating magnetic field, and the receive coil can detect the signal generated during

the post-stimulation "ring-down" [Zen02, She10]. This allows temporal separation of the tag signal from that induced by the AC interrogating magnetic field. The detection can also be performed by acoustic or optical approaches [Jai01].

The frame-suspended resonator is designed to be attached to its package by its frame. Because the tags have a slight out-of-plane curvature that is an artifact of the casting and photochemical machining (PCM) process (described in in Section 4.2), the suspension is effective even when unpackaged tags are placed on a flat substrate. With the convex surface away from the substrate, only the perimeter frame of the tag contacts the substrate, allowing the central vibrating part to resonant with minimum interaction with the supporting substrate.

The hexagonal geometry is specifically chosen to allow maximum usage of material for a batch patterning process. The symmetrical geometry is also expected to reduce the signal strength sensitivity to orientations of applied magnetic field. Another benefit of the shape pertains to signal orientation. When excited by an applied AC field, the symmetrical hexagonal tag generates two major magnetic response components, with one parallel and the other orthogonal to the applied AC signal. Consequently, an orthogonally-oriented receive coil couples weakly with the applied signal and strongly with the response of the magnetoelastic tag. This interrogating and detecting approach is used in this study.

4.1.2 Modeling

4.1.2.1 Magnetic Field Strength

In order to estimate the applied AC magnetic field strength necessary for interrogating the tags, transmit coils were modeled in COMSOL Multiphysics. Because the size difference between the coils and the magnetoelastic tags is large, it is appropriate

to first calculate the magnetic field strength generated by the coils in a separate model and then use the calculated values as exciting conditions in the customized magneto-mechanical model that is spatially focused on a single magnetoelastic tag. In this work, two experimental setups were utilized – configurations A and B (Fig. 4-2). Detailed descriptions of these two configurations are given in section 4.3.1. Modeling results indicated that the applied AC fields per unit electrical current that are available at the locations of interest from configurations A and B are 2.69 Oe/A and 0.85 Oe/A, respectively.

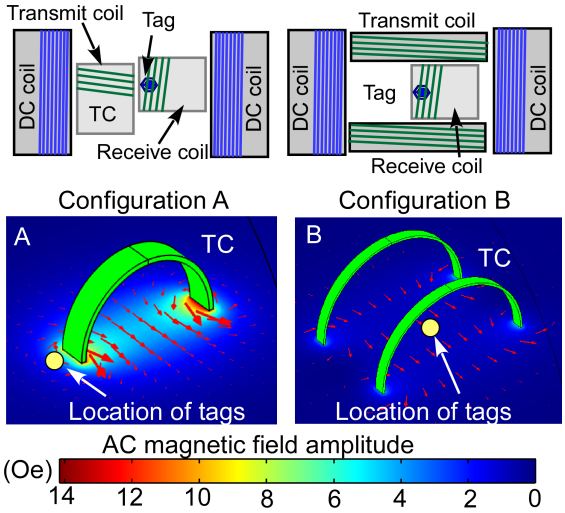

Fig. 4-2: Results of FEA simulations of signal strength generated by transmit coils for configurations A and B. The ratios of the AC magnetic field amplitude to the applied AC current amplitude for configurations A and B are 2.69 Oe/A and 0.85 Oe/A, respectively, at the locations of interest.

4.1.2.2 Mode Shapes, Resonant Frequencies of Hexagonal and Disc Magnetoelastic Tags

The pre-calculated AC magnetic field was used for modeling the resonant response of hexagonal and disc magnetoelastic tags in the magnetomechanical coupled FEA model described in Chapter 2. Fig. 4-3 shows the calculated mode shapes of hexagonal (1.4 mm circumscribed diameter) and disc tags (1 mm diameter) at resonant

frequencies of about 2.09 and 2.1 MHz, respectively. The desired mode shape – which exhibits both longitudinal and transverse motion – generates an oscillating magnetic field with one significant response component that is orthogonal to the applied AC field, facilitating the decoupling of the applied AC field from the received signal by orienting the transmit coil and receive coil orthogonally. Because it is difficult to estimate the interaction between the tag and the supporting substrate, the "free-standing" condition is used for both FEA models of hexagonal and disc-shaped tags. Accordingly, these two types of tags have similar theoretical performance without considering the interaction between the substrate and the tag. In practice, only the frame of the hexagonal tag interacts with the supporting substrate while the central resonator can vibrate freely. In contrast, the entire disc or disc perimeter interacts with the substrate. Therefore, a significant signal amplitude advantage for the frame-suspended tag is expected. The FEA simulations also show that the frame-suspended tag is sensitive to the azimuthal direction of applied AC magnetic field (Fig. 4-3).

In order to compare the azimuthal characteristics of the hexagonal tag with a conventionally-shaped rectangular strip, a strip design of 1 mm x 0.2 mm x 27 μm was also modeled. According to FEA simulations, under different orientations of applied AC magnetic field, the azimuthal variation in the response amplitude was 26.7:1 for the strip. In contrast, for the frame-suspended hexagonal tag, it was only 4:1, indicating that this shape presents an improvement.

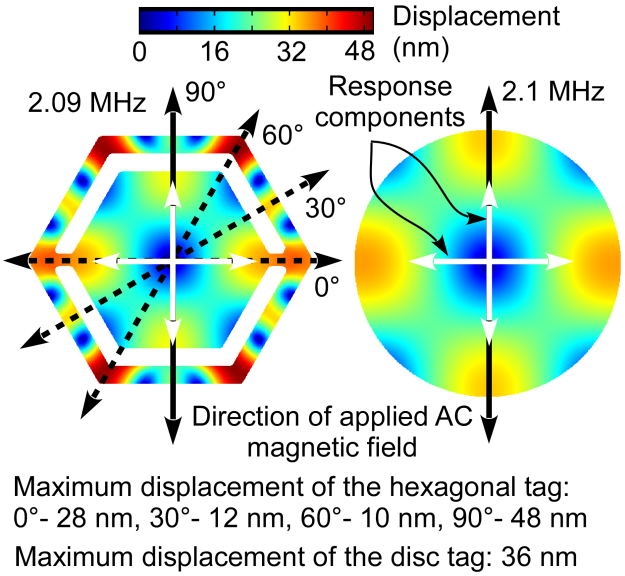

Fig. 4-3: FEA simulation results of hexagonal and disc tags. The hexagonal tag, with a size of ø1.3 mm x 27 µm, resonates at 2.09 MHz. Its response is sensitive to the orientation of the applied AC field. The disc tag, with a diameter of 1 mm, resonates at 2.1 MHz. These simulations do not account for contact with the substrate encountered in practice. Frame-suspended resonators contact the substrate only at the frame whereas the others do so over the entire surface.

4.2 Fabrication

In the PCM process, magnetoelastic tags are batch patterned from a ≈27 µm thick foil of as-cast Metglas™ 2826MB, an amorphous NiFeMoB alloy [Met08], utilizing a "tabless" approach. In this process, the Metglas™ thin foil is laminated with photoresist film on each side. The photoresist films are then lithographically patterned, resulting in the selective removal of portions of the films and revealing the metal beneath. The exposed metal is etched away by an acid spray, leaving the patterned Metglas™ structures. The etching process is isotropic. Normally, PCM fabricated devices have tabs that keep the devices connected to the foil throughout the etch process. However, the "tabless" process is utilized in this work because it allows hundreds of tags to "drop" from the Metglas™ foil automatically during the etching process, eliminating the extra time, cost, and geometrical variability resulting from an additional tab cutting process.

Approximately 500 disc tags (resonator only) and 1000 hexagonal tags (resonator and frame) were fabricated. As shown in Fig. 4-4, the lateral undercut for sidewalls of a hexagonal tag is 32 μm. This is small compared to the size of the tag, so predictability and consistency is expected in the resonant frequency across a batch of tags. The undercut can be further reduced by utilizing double-sided lithography and etching instead of the one-sided process that is used for this study.

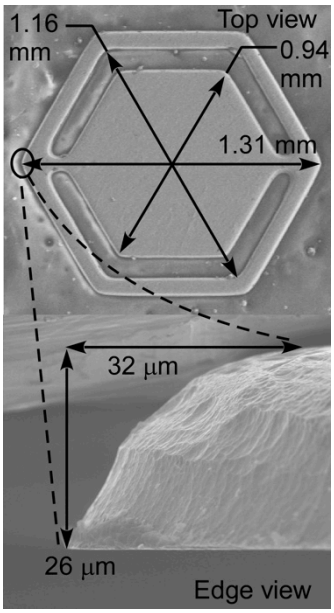

Fig. 4-4: SEM pictures of a frame-suspended hexagonal tag show the maximum sidewall over-etch is about 32 μm. Inspection of fabricated disc tags revealed a similar edge profile.

4.3 Experimental Methods and Results

4.3.1 Experimental Methods

As noted in Section 4.1.2.1, two configurations (A and B) of transmit coils and receive coils were utilized for characterization of small and large quantities of magnetoelastic tags (Fig. 4-2). Configuration A is suitable for small quantities of tags, as it provides a strong and concentrated interrogating field. Configuration B is suitable only

for very large quantities of tags, as it provides a weaker but more uniform interrogating field.

Both configurations included a network analyzer, an RF amplifier, and a receive coil. For these tests, the magnetic bias necessary for the tags was not provided by a permanent magnet, but instead by DC Helmholtz coils that were included in the setup. The transmit coil(s) and the receive coil were configured orthogonally. This arrangement of coils and symmetrical design of resonators contributed to decoupling the applied AC field from the received signal, reducing the signal feedthrough and emphasizing the response of the tags. The network analyzer provided the input signal, which was sent to the amplifier and then to the transmit coil. The receive coil was connected directly to the network analyzer as well. For all data presented here, the baseline signal feedthrough (without tags present) has been subtracted.

In configuration A, the transmit coil and receive coils were placed ≈0.5 cm apart. The targeted 1-10 tags were placed close to the transmit coils to provide a strong interrogation field. The transmit and receive coils used in configuration A had four turns of 60-strand 22 AWG Litz wire, in which each individual conducting strand is insulated to reduce impedance at high frequencies. These coils had 3.6 cm diameter and 0.5 cm axial length. In configuration B, which provided a weaker but more uniform field that could accommodate hundreds of resonators, the applied AC field was provided by two Helmholtz coils, each with four turns of the same Litz wire, a diameter of 7.2 cm and an axial length of 0.5 cm. The two Helmholtz coils were separated by 3.6 cm. The receive coil for configuration B was the same as for configuration A. The DC bias field was applied using two additional Helmholtz coils, placed 12 cm apart, each with 12.5 cm diameter and 3.3 cm axial length.

The applied AC current amplitudes for configuration A and B were experimentally measured to be 2.9 A and 0.94 A (N2774A current probe, Agilent, Santa Clara, CA). According to the FEA simulated relationship between magnetic field and the AC current (Section 4.1.2.1), the amplitudes of AC magnetic fields used for experiments at the location of the tags were estimated to be 7.8 Oe and 0.8 Oe for configurations A and B, respectively.

4.3.2 Experimental Results of a Single Magnetoelastic Tag using Configuration A

Fig. 4-5 shows the typical measured signal amplitude and resonant frequency of a hexagonal tag as a function of DC bias. The signal amplitude reaches a maximum and the resonant frequency reaches a minimum [Cop94] when a preferred 31.5 Oe DC bias was applied. In a similar study, the required DC magnetic field bias for disc tags was experimentally determined to be 33 Oe.

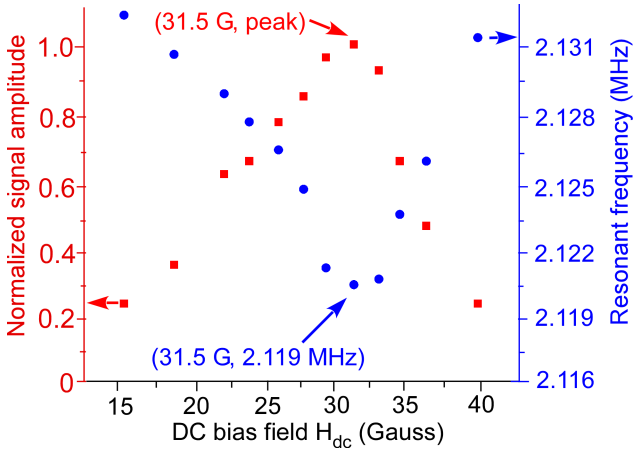

Fig. 4-5: The typical preferred DC magnetic field bias for a single frame-suspended hexagonal tag is experimentally measured to be 31.5 Oe. The signal amplitude is normalized to the peak when a preferred DC magnetic field is applied. At this bias field strength, the resonant frequency and signal amplitude reach a minimum and maximum, respectively.

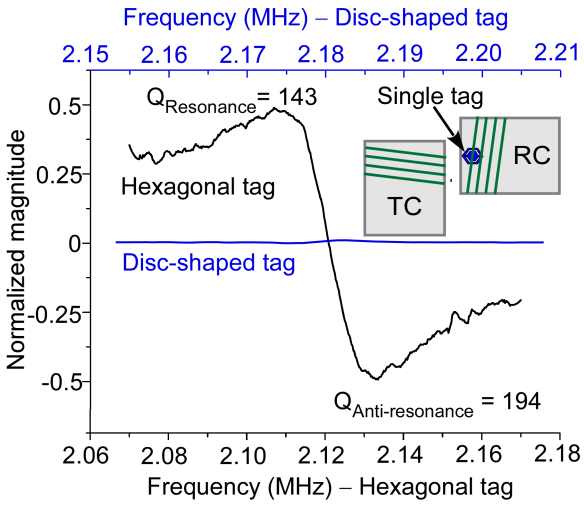

Fig. 4-6: A typical resonant response of a frame-suspended tag, exhibiting quality factors of 100-200 at a resonant frequency of 2.11 MHz.

Because the signal amplitudes of tags vary with different experimental setups and the measuring conditions, signal amplitudes in this paper are normalized to the measured maximum signal amplitude of a single frame-suspended hexagonal tag with a preferred DC bias under the condition that the DC and AC fields are aligned. The measured signal amplitude of a frame-suspended hexagonal tag was 75X that of a disc-shaped tag (without a suspension) that was measured for comparison (Fig. 4-6). The resonant response of frame-suspended hexagonal tags showed quality factors of 100-200.

As expected, the response of the frame-suspended hexagonal tags varies in amplitude with the azimuthal orientation of the applied AC magnetic field (Fig. 4-7(a)). Although signal amplitude varied with angle, it was larger than that of disc-shaped tags in every orientation. In this measurement, the DC bias magnetic field and the applied AC field had the same direction while the axis of the receive coil was orthogonal to the directions of those two fields. Fig. 4-7(b) shows the effect of orientations of DC bias field on the signal amplitude while the applied AC field and the received AC field were maintained at angles of 90˚ and 0˚ to the tag, respectively. With a 45˚ offset between the

applied AC and DC bias field, the response increased by about 80%. The AC field amplitude was 7.8 Oe, whereas the DC field was 31.5 Oe.

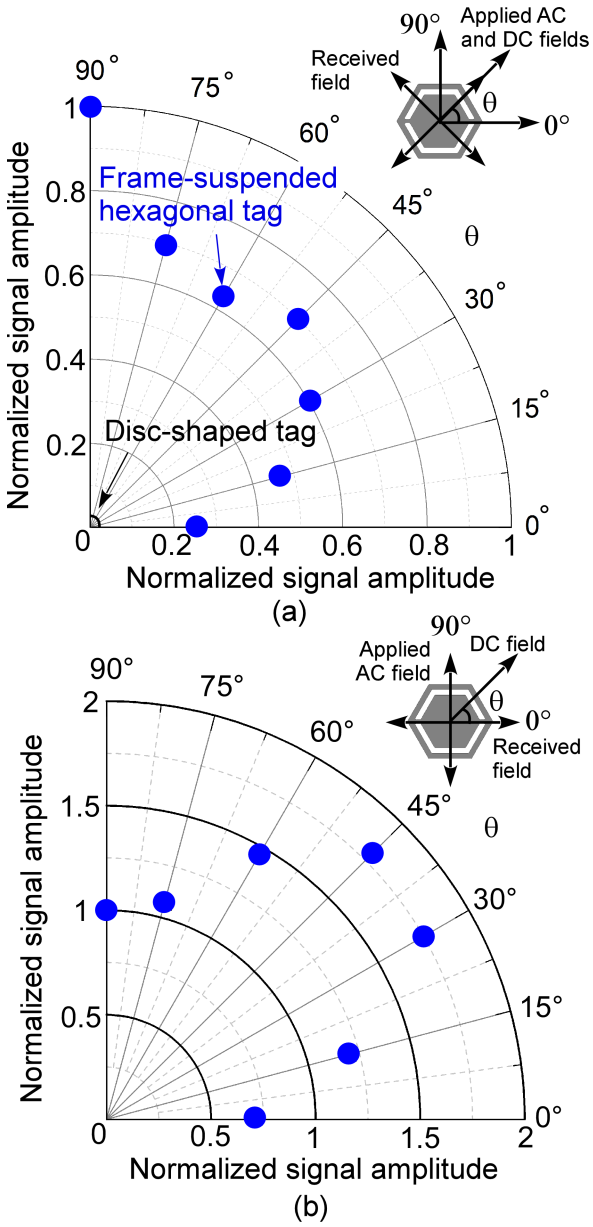

Fig. 4-7: (a) The measured normalized signal amplitudes of a typical frame-suspended hexagonal tag and an unsuspended ø1 mm disc-shaped tag as a function of orientation of azimuthal angle of applied AC magnetic field. The DC bias field and applied AC field have the same orientation. (b) While changing the direction of the DC bias field, the applied AC field and received field are maintained at 90˚ and 0˚ with respect to the tag. All signal amplitudes for (a) and (b) are normalized to the maximum signal amplitude measured with the applied AC field and DC bias aligned with each other at 90˚ with respect to the tag, as used in (a).

4.3.3 Experimental Results of Small Quantities of Hexagonal Tags using Configurations A and B

A number of hexagonal tags were measured individually to evaluate the basic variability in resonant frequency. Across 10 hexagonal tags, the average resonant frequency was 2.128 MHz with a 0.44% standard deviation. The small process variability facilitates signal superposition when the tags are arrayed or clustered.

Signal superposition for small quantities of hexagonal tags (up to 10) was measured using configuration A. The tags were placed in a 2X5 array in the proximity of the AC transmit coil. Evidence of signal superposition was provided by the analysis of 4 tags (Fig. 4-8). When tested individually, the peak-to-peak amplitude of these tags varied from 100 μV to 150 μV, and their resonant frequency ranged from 2.118 to 2.127 MHz. When tested together, the peak-to-peak response was 700 μV, and the resonant frequency was 2.123 MHz. As shown in Fig. 4-9, the signal strength increased linearly with the number of arrayed tags for modest counts.

The resonant responses of small quantities of tags were experimentally measured by configuration B as well, and normalized to the response of a single tag in configuration A. The equivalent normalized signal amplitudes for 4, 6, 8 and 10 tags in configuration B were calculated by multiplying measured signal amplitudes by the ratio of the simulated magnetic field strengths: 7.8 Oe/0.8 Oe. Fig. 4-9 shows a good match for the normalized equivalent signal amplitudes measured by the two different configurations.

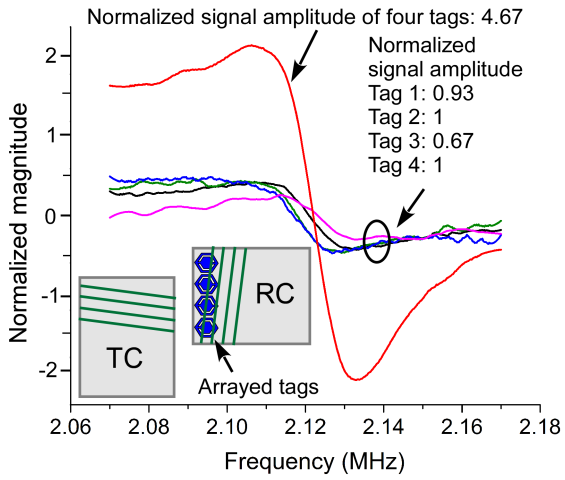

Fig. 4-8: Signal superposition for four frame-suspended tags: the overall signal amplitude of four tags is 4.67, whereas individual tags have signal amplitude of 0.93, 1, 0.67, and 1, normalized to the largest signal amplitude in the group.

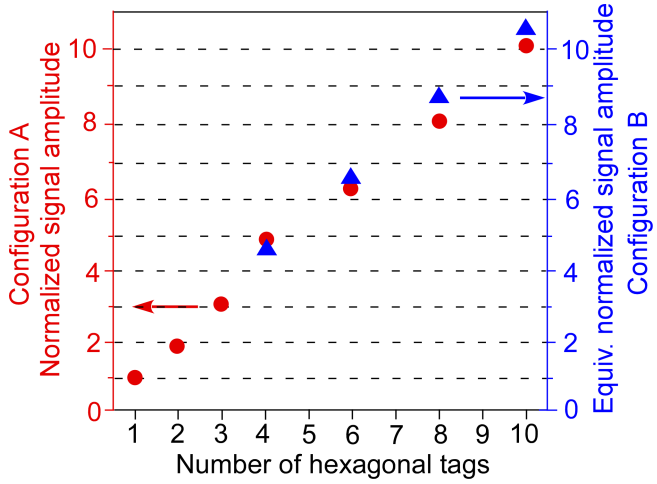

Fig. 4-9: Signal amplitudes of arrayed frame-suspended tags as a function of number of tags ranging from 1-10. The signal amplitudes are normalized to the largest signal amplitude measured amongst 10 tags in configuration A. The equivalent normalized signal amplitudes reported for configuration B are corrected by the ratio of the simulated applied magnetic fields in the two configurations.

4.3.4 Experimental Results of Large Quantities of Randomly Clustered Tags using Configuration B

The frequency responses of large clusters of hexagonal tags were experimentally evaluated. These tags were randomly clustered because of the difficulty in arraying such large quantities with preferred orientation and with convex surfaces away from the

substrate. The inset within Fig. 4-10 shows the typical resonant response for 500 randomly clustered frame-suspended tags at a resonant frequency of 2.13 MHz, presenting a signal amplitude that is ≈500X the signal amplitude from a single tag. Fig. 10 also indicates that although there may be signal loss due to random orientation and placement of the tags, the signal amplitude varied in approximately linear fashion with the number of tags. Interaction between tags might have contributed to the compensation of the signal loss expected by random tag orientations and placement, but this requires further study that is beyond the scope of this paper.

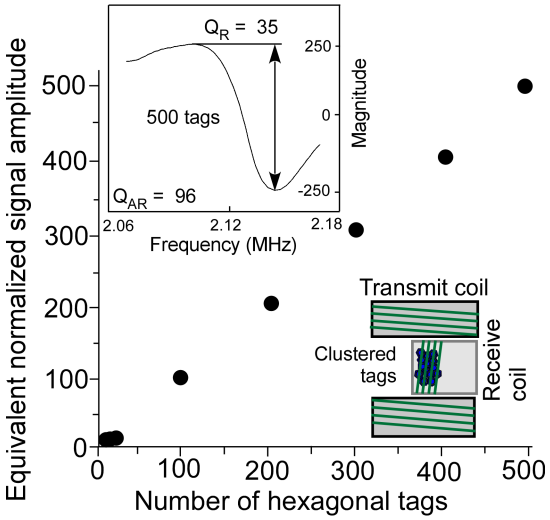

Fig. 4-10: Equivalent normalized signal amplitudes of randomly clustered hexagonal tags as a function of number of tags (up to 500). Test configuration B was used.

4.4 Discussion

In order to maintain the signal strength at millimeter dimensions for magnetoelastic tags, two features were investigated: frame suspensions and signal superposition. Experimental results showed that the frame suspension provides a significant signal amplitude increase for a single magnetoelastic tag. Although the frame suspension was demonstrated for hexagonal tags, a similar approach for performance

improvement may also apply to typical conventional rectangular strips. For example, a strip can be suspended by two springs connecting its center to an outer frame.

It was also confirmed that signal superposition boosts the signal strength dramatically for both carefully arrayed or randomly clustered small and large quantities of magnetoelastic tags. The signal superposition for large quantities (up to 500) of clustered magnetoelastic tags was experimentally evaluated. The advantages of miniaturization as demonstrated in this work is the ability to tag small items individually or the ability to distribute tags into networks of small tubes or crevices. Clustered large quantities of these tags can be utilized for applications that require long-range detection.

A package with appropriate support and an integrated DC bias magnetic material requires further consideration. For a product-level implementation, the magnetoelastic tag should be supported by the frame so that the resonant element can vibrate freely. The package should also include a magnetic material that provides the DC field bias. The biasing magnet material – preferably with a geometry similar to that of the tag – should have high coercivity, and a material like Arnokrome™ (an iron-chromium-cobalt alloy) may fit the purpose.

Metglas™ 2826MB has been used for this work, but other amorphous alloys with high magnetostrictivity, good mechanical properties, and demanding a modest DC bias field might provide better performance than this work. Although the PCM process is appropriate for the fabrication of hundreds of magnetoelastic tags, other low cost fabrication processes capable of producing large quantities may be worthwhile to explore. Metglas™ and other amorphous alloys can be fabricated with desired geometry by metal alloy quenching [Che89]. Typically, metal powders or granules with preselected portions are melted and homogenized, and then the molten alloy is rapidly quenched on a surface or in a recess with the desired geometry.

Annealing of the magnetoelastic material – especially transverse field annealing – can potentially improve the performance [Bro79]. However, transverse field annealing will likely increase the signal strength sensitivity to the orientation of the applied magnetic field because, unlike the as-cast material, a transverse-field-annealed material has induced magnetic anisotropy. Implementation of a transverse-field-annealed tag would require further study for the specific intended application.

The detection range is normally limited by the interrogation and detection approach – especially in how the approach accommodates transmitter-to-receiver feedthrough. This work employed spatial separation of applied and received signals afforded by the coupled longitudinal and transverse resonant motion of the tags. However, other approaches may complement this approach and further enhance transmitter-to-receiver isolation and thereby increase range. For example, a pulsed interrogating signal can be used, and the magnetic flux generated during the "ring-down" vibration of tags could be detected so that the excitation signal is temporally decoupled from the received signal. An acoustic interrogating signal, instead of a magnetic field signal, could also be used for decoupling the excitation signal from the receive signal.

4.5 Summary

This chapter described the investigation of PCM fabricated hexagonal magnetoelastic tags of about ø1.3 mm X 27 μm, which is approximately 100X smaller than commercial tags currently in use. The preferred DC field bias for the fabricated tags was ≈31.5 Oe. The tags showed quality factors of 100-200. The frame suspension of hexagonal tags resulted in ≈75X improvement in signal amplitude compared to that of non-suspended tags with similar size, frequency, and DC field bias orientation. For the frame-suspended hexagonal tags, misalignment DC bias field by 45˚ with respect to the

applied AC field provided another 80% improvement in signal amplitude. Although the frame suspension is demonstrated in miniaturized magnetoelastic tags, it may also be used to improve the performance of commercial tags or other magnetoelastic sensors. The signal amplitude of a hexagonal tag was a function of the azimuthal orientation of the applied AC magnetic field. Varying signal was observed for different orientations. For 1-10 arrayed tags, the signal amplitudes were at least the sum of the amplitude of each tag. Across 10 hexagonal tags, the average resonant frequency was 2.13 MHz, with a standard deviation of 0.44%. Such a small variation of frequency response favors signal superposition and increased signal strength for ensemble detection. Signal superposition was also observed for up to 500 clustered tags.

Chapter 5

Conclusions and Future Work

5.1 Performance Summary

This work studied wireless tagging and actuation with shaped magnetoelastic transducers. Magnetoelastic resonant rotary motors were studied as a classic actuator example while the magnetoelastic tags were also investigated to explore the limitations of miniaturization.

5.1.1 Magnetoelastic Resonant Rotary Motor Performance Summary

The first generation motors demonstrate a standing wave resonant rotary motor, which uses a stator with a bilayer of silicon (ø8 mm x 65 μm thick) and magnetoelastic foil (Metglas™ 2826MB bulk foil, ø8 mm x 25 μm thick) to tailor the stiffness and mode shapes. The motor provides bi-directional rotation capability. The counterclockwise mode provides a rotation rate of ≈100 rpm, start torque of 30 nN·m, a step size of 74 milli-degree and a capability for driving a 100 mg payload while a 8 Oe DC and a 6 Oe-amplitude AC magnetic field are applied. One advantage of the magnetoelastic motor is the wireless actuation. This reduces the complexity of integrating the control circuit with the device and facilitates miniaturization. The motor also provides high payload (up to 100 mg), which is preferred for applications that requires the rotary stage to be able to carry and drive other hybrid-integrated sensors. The magnetoelastic motors can operate with a very small step (less than 10 milli-degree), which can potentially provide very accurate rotation resolution with proper control design.

The second-generation of motors include both standing wave and traveling wave designs (ø5 mm stator) with integrated capacitive sensors for real-time position measurement and speed estimation. Clockwise and counterclockwise mode shapes with resonant frequencies of 12 kHz and 22.4 kHz, respectively, are measured for the standing wave motor. Two mode shapes (with $\pi/2$ spatial phase difference) at resonant frequencies of 30.2 kHz and 31.7 kHz are measured for the traveling wave motor.

5.1.2 Promising Advantages of Magnetoelastic Actuation

The output power, one important performance metric for practical applications, is compared between different types of chip-scale rotary actuation methods in Fig. 5-1. In general, piezoelectric motors provide relatively large output power. There is also significant improvement that has been achieved for electrostatic and electromagnetic micromotors over the years. The first generation magnetoelastic motors provide moderate performance among all the chip-scale motors; however, considering that magnetoelastic motors are early in development, there is still large space for improvement. Because of the similar energy density and coupling coefficient [Lun97, Wan07], the theoretical potential performance of magnetoelastic motors is comparable to that of piezoelectric motors. In addition, the unique promising advantages of magnetoelastic motors lie in wireless actuation and simplified system architecture.

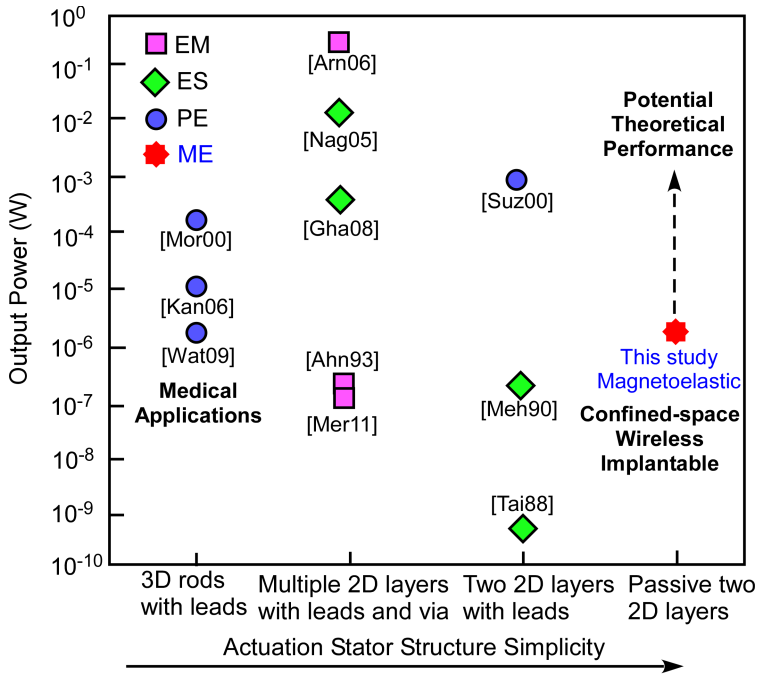

Fig. 5-1: Comparison of the output power of different types chip-scale rotatory actuation methods: electromagnetic (EM), electrostatic (ES), piezoelectric (PZ) and magnetoelastic (ME).

A major advantage of the magnetoelastic motors is wireless actuation. Although electromagnetic motors are also wirelessly driven, the driving distances are typically in micron scale [Guc91, Liv04]. In this work, at least a few centimeters of actuation distance is achieved for magnetoelastic rotary motors, because a uniform, unidirectional magnetic field is all that needed for actuating the standing wave motor. The actuation distance can be further increased by sacrificing power efficiency due to energy loss in the coils and the intervening medium (e.g. air). This unique advantage provides an actuation approach for remote applications, such as wireless implantable medical devices. The wireless actuation also allows operation in confined space, in which the integration of the power supply or other active electric components is a challenge.

Another major benefit of magnetoelastic actuation lies in the simplified architecture. The magnetoelastic actuation method described in this work is developed based on 2D structures with integration between the magnetoelastic material and silicon.

In addition, this magnetoelastic actuation method utilizes passive structures. Miniaturization can be easily achieved or more functional components can be easily integrated into the motor by taking advantage of the space freed by the reduced requirement for onboard power and wiring. This is demonstrated in the second-generation motors with the integration of the capacitive sensing electrodes.

5.1.2 Miniaturization of Magnetoelastic Tags

Another major achievement of this work is the miniaturization of magnetoelastic tags while maintaining the response signal strength. Miniaturized magnetoelastic tags have an overall size of ø1.3 mm x 27 μm and a resonant frequency as high as 2.13 MHz. The tags are about 100x smaller than the commercial anti-theft magnetoelastic tags. A unique feature is the frame-suspension, which results in ≈75x improvement in signal amplitude compared to that of non-suspended disc tags with similar size and frequency. The signal amplitude can be boosted by utilizing signal superposition of an ensemble of tags. This superposition is experimentally measured for up to 500 clustered magnetoelastic tags.

Although these two approaches provide a significant increase in the response signal strength of magnetoelastic tags, the detection range is limited by feedthrough from the transmit signal in the current interrogation approach. For future designs, it is important to investigate other interrogation approaches for increasing the detection range.

5.2 Future Work

5.2.1 Integrated Wafer-Level Fabrication Process for Magnetoelastic Motors

There are some potential design improvements worthy to be studied. For standing wave motors, miniaturization is facilitated because they are made with micro-fabricated

passive components. A layer with proper design of hub and cap structures is necessary to reduce the lateral and out-of-plane motion of the rotor. This layer should be attached to the stator with good alignment. A close-loop control system is also preferred for a precise rotational output. For the prototype of the traveling wave motor, the frequency mismatch between the desired mode shapes compromises the performance. Thus, the next design should focus on reducing this frequency mismatch by either using an isotropic material or compensating for the anisotropy of silicon with targeted mass and stiffness distributions. Minimizing susceptibility of the geometry to asymmetry as a result of fabrication is also important. Another solution is to tune the resonant frequencies of the stator by precisely trimming the stator or springs after fabrication.

For the first-generation magnetoelastic rotary motors, a stainless steel hub with a diameter of 1 mm is used for constraining the rotatory motion. However, the lack of control of the gap between the hub and rotor results in relatively large lateral walking of the rotor. The center hub also does not have any features that prevent the out-of-plane wobbling of the rotor. The relatively large diameter of the hub also increases frictional torque that reduces rotation rate and motor efficiency. Thus, one future work should focus on integration of the hub and rotor with the stator with a wafer-level fabrication process. In the next sub-sections, a possible architecture is first given, then the fabrication processes for such an approach are also discussed.

5.2.1.1 Architecture

A possible architecture of the magnetoelastic resonant motors with integrated fabrication processes for stators and rotors is shown in Fig. 5-2. It consists of a stator with a bilayer of silicon and magnetoelastic material, and a cap rotor layer with self-alignment features. The rotor and the capping layer are made out of a silicon on insulator

(SOI) wafer. The rotor layer and the stator layer are fabricated separately and can be bonded at the wafer or die level. The rotor is released after the bonding process. The detailed description of the fabrication processes is given in the next sub-section.

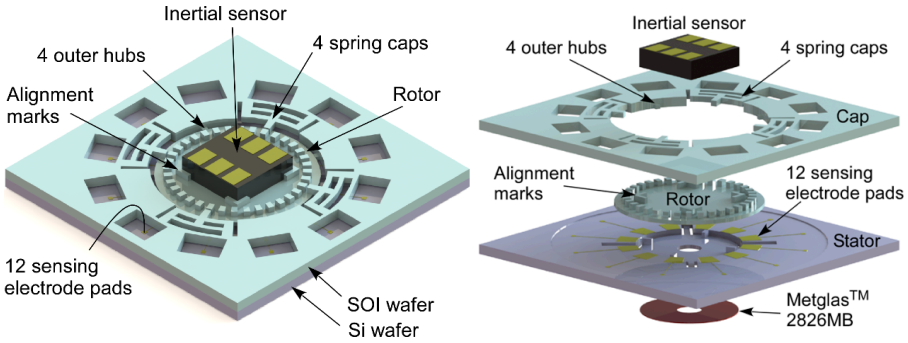

Fig. 5-2: 3D schematic and each layer of Gen.2.0 motor design. The design the rotor layer allows integration of alignment marks for the inertial sensors or fabricated together with the rotor layer.

5.2.1.2 Overall Process Description

The proposed fabrication process includes a standard silicon wafer and a SOI wafer, as shown in Fig. 5-3. The wafer level integration can be realized by fabricating a rotor and a capping layer simultaneously from a SOI wafer. The rotor is released after bonding the rotor layer to the stator layer. The lateral gaps between the rotor and the hub are defined lithographically (less than 10 μm). The out-of-plane gap can be controlled by adjusting the thickness of the bonding layer. This approach provides a lateral and an out-of-plane misalignments that are less than 10 μm. The Metglas™ layer can be fabricated separately and bonded with the stator in the same process, or it can be deposited directly on the silicon.

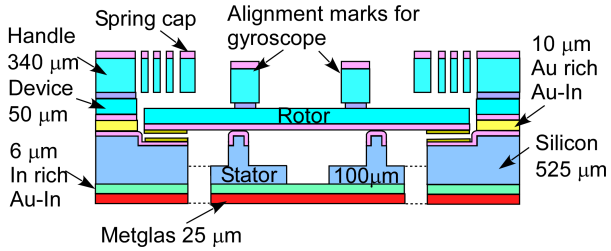

Fig. 5-3: A schematic of the cross-section of the bonded rotor layer, stator layer and Metglas™ layer.

The stator can be fabricated using the same process developed for second-generation magnetoelastic motors described in Chapter 3. In addition, the magnetoelastic material can be directly deposited and patterned on the backside of the silicon.

The rotor is fabricated from a SOI wafer with a 50 μm thick device layer and a 340 μm thick handle layer, as shown in Fig. 5-4. First, a 2 μm thick silicon nitride and 2 μm silicon oxide are deposited on the device layer using PECVD. The oxide is then patterned using BHF wet etch. A 0.5 thick Al layer is evaporated then patterned on the handle layer by using lift-off. Another 2 μm silicon nitride layer is then deposited on the top of the aluminum layer. This layer is for passivation of the electrodes to reduce shorting between the rotor and stator layers and to allow active electrostatic rotor lockdown, if desired. A Cr/Au (0.1 μm/0.5 μm) seed layer is evaporated and patterned on the handle layer by using lift-off. An Indium layer with thickness of 6 μm is electroplated on the device layer for gold rich Au-In bonding between the rotor wafer and the stator wafer. A thick PR is coated and patterned as the mask for the DRIE steps. Silicon nitride is etched using RIE and the silicon is DRIE etched down to the buried oxide as an etching stop layer. Then, the silicon of the device layer is DRIE etched using silicon oxide as an etching mask. An Al_2O_3 layer is then deposited all over the devices. The Al_2O_3 layer at the bottom of the trench in the device layer is selectively etched using RIE to expose the silicon. The exposed silicon area is DRIE etched to the buried oxide. After that, an isotropic silicon etch allows undercutting the silicon structures with small dimension, while leaving the wide structures in the device layer remaining in contact with the handle layer through the buried oxide. The fabrication of the rotor layer is completed.

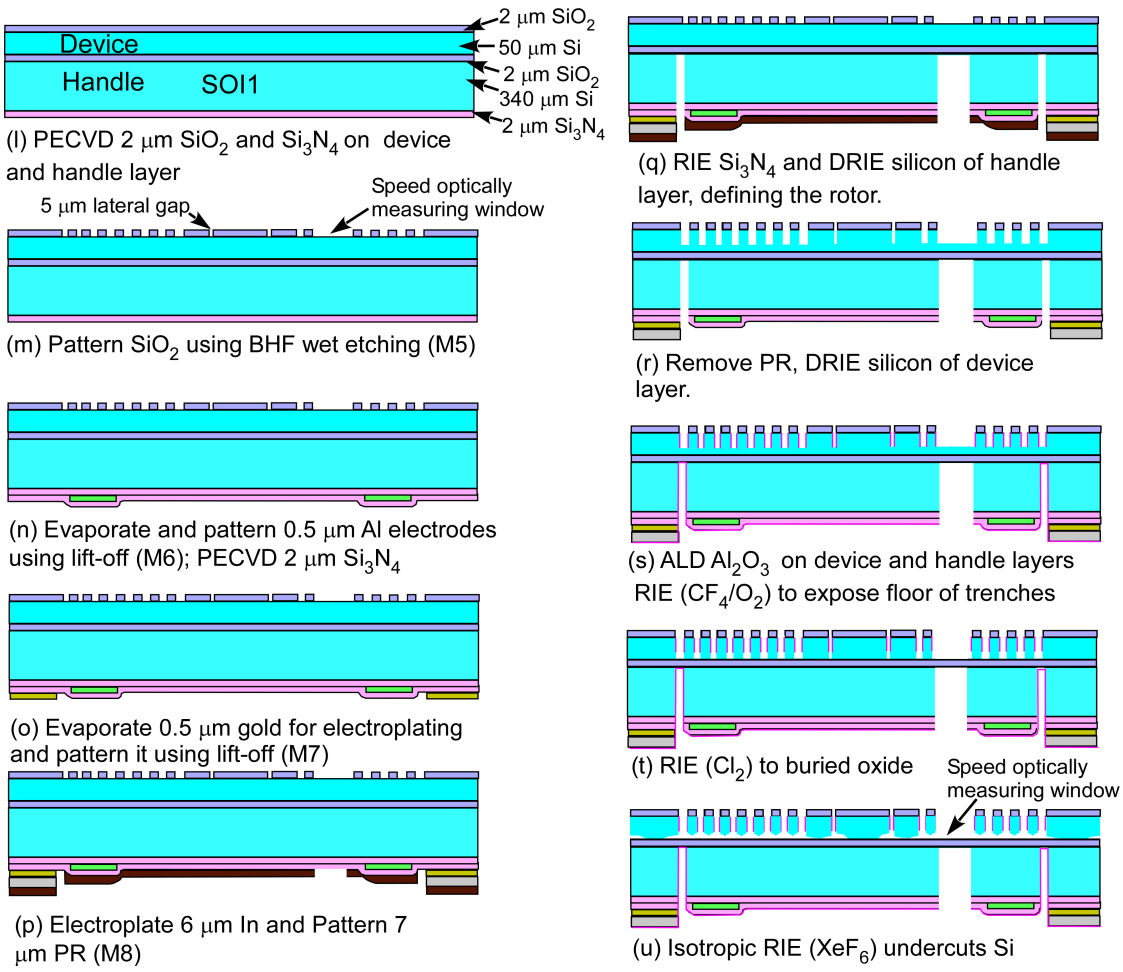

Fig. 5-4: Fabrication processes of a rotor layer. The fabricated rotor layer has a center hub that confines the lateral and in-plane motion of the rotor. The center hub design reduces the friction force between the hub and rotor significantly compared to an outer hub, which is more easily to be fabricated.

After fabrication of the stator and rotor separately, the rotor wafer and stator layer is first bonded using gold rich Au-In bonding. Then, the rotor can be released or detached from the capping layer using wet etching. Finally, Metglas™ is bonded to the stator wafer, which completes the fabrication.

5.2.2 Magnetoelastic Tags

5.2.2.1 Increase Detection Range by Exploring Different Interrogation Approaches

Although the frame-suspended magnetoelastc tags provide a significant advantage in signal strength compared to that of non-suspended magnetoelastic tags, the interrogating range is limited by the feedthrough from the transmit signal. For current interrogating approach, the receive signal is a combination of the transmit signal and the response signal generated by the tags, making it difficult to extract the latter signal when the sensing distance increases and the transmit signal is very strong. Other approaches are worth studying.

One promising approach is to differentiate the transmit signal and the receive signal in the time domain. First, a transmit signal that can be a pulse or a short period of AC signal is sent to the tags. Then the receive coils start to pick up the signal generated during the "ring-down" vibration of the tags. Because the miniaturized magnetoelastic tags resonates at a very high frequency, the transmit coil should have a relatively small quality factor, in order to prevent the transmit signal being generated after the period of the applied exciting signal. In the opposite, the receive coils should have a high quality factor and a resonant frequency similar to that of the tags for a strong receiving signal response. For the magnetoelastic tags, high quality factors are preferred for a long "ring-down" vibration time. The quality factors of the magnetoelastic tags can be increased by changing the suspensions (i.e. reducing anchor loss), or by using a vacuum package, or by bonding the magnetoelastic material to other materials with high quality factors.

Another approach is to differentiate the transmit signal and receive signal by changing the exciting physical domain. Instead of driving the vibration of the magnetoelastic tags magnetically, an acoustic signal can be used for excitation. In that case, mainly the electromagnetic response signal from the tags is picked up by the receive

coils. However, appropriate approaches for generating and propagating an acoustic wave that targets and sufficiently excites the tags remain a challenge.

5.2.2.2 Further Miniaturization of the Magnetoelastic Tags

For some applications, magnetoelastic tags have to be distributed through a very small space into the detection regions of interest. This requires further miniaturization of the tags. However, when the size of the magnetoelastic tags is further reduced, the sensitivity of resonant frequency with respect to the dimensions of the tags increases dramatically, as shown in Fig. 5-5. Thus, a low cost fabrication approach for large quantities of magnetoelastic tags with accuracy of tens of microns requires further study.

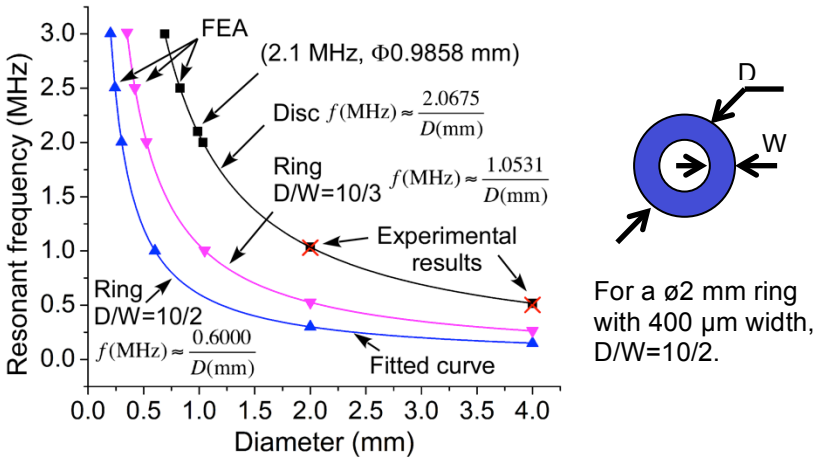

Fig. 5-5: FEA simulation results of the resonant frequency versus the size of a disc or a "ring" magnetoelastic tag.

5.3 Major Contributions to the Field

One focus of this work is the wireless magnetoelastic resonant rotary motor. The concept of utilizing 2D magnetoelastic structures for standing wave and traveling wave resonant motors is new to the field. The successful demonstration of a bi-layer of the silicon and bulk magnetoelastic material shows the promising potential for actuation.

One specific advantage – wireless actuation – makes miniature magnetoelastic motors an attractive candidate for wireless microsystems.

Another focus of this work lies in miniaturization of the magnetoelastic tags. With proper designs and packages, the frame-suspension concept can also be applied to other magnetoelastic tags for an improvement of response signal strength. The signal strength can also be boosted by utilizing small or large quantities of arrayed or clustered magnetoelastic tags. This opens a new window for many applications. For example, large quantities of magnetoelastic tags can be distributed into a network of cracks or pipes, which then can be mapped by the detection of the locations of the accumulated magnetoelastic tags.

APPENDIX A

Dynamic Model of Magnetoelastic Standing Wave Rotary Motors

Precision measurement of rotary stages requires exceptionally high motion accuracies in order to meet gyroscope calibration requirements of rotation at up to 1000 degree/s over arbitrary angles with a resolution less than ±10 milli-degree. To reach such accuracy, the dynamic behavior of a given micro-motor must be very well understood and distilled into an analytical or numerical model. A model of the motor dynamics that is simple yet captures the essential behaviors, including transient and steady state stator motions, stator-to-rotor momentum transfer mechanics and energy loss mechanisms could be used for predictive design in Kalman filters or other estimation and control schemes for motion reconstruction from intermittently sampled rotor position data and in servo-control systems that improve motion accuracy. The basic development of such a model is the subject of this appendix[3].

The dynamic model presented in this paper focuses on the standing wave magnetoelastic rotary motors described in Chapters 2 and 3 of this thesis. Both the stator and rotor motion is substantially affected by contact interactions between the two. Thus, the model presented here captures the second order linear system dynamics of the stator and the linear and angular momentum transfer between the stator and rotor, coupled with the rigid body dynamic response of the rotor. This model is coupled with the rigid body dynamic response of a rotor to model magnetoelastic motor behavior.

[3] The work in this appendix was done in collaboration with Mr. Jinhong Qu, Dr. Scott Green, and Prof. Kenn Oldham.

A.1 Dynamic Rotary Motor Model

The basic approach to the dynamic rotary motor model is first described, followed by the assumptions made by the model. Then, the stator geometry and dynamic motion, both steady state and transient, are discussed; a second-order linear model of the stator will be introduced. Next, the analyses around the collision time points are developed based on the linear model of stator. The final step is to model the motion of the rotor between two separate collisions. At the end of this section, the typical model output is presented and the parameters in this model are discussed.

A.1.1 Modeling Approach

A.1.1.1 Modeling Method

To understand and predict the dynamic motion of the motor, both a Parametric Modal Model (PMM) and a Finite Element Model are used. The Parametric Modal Model is based on the parameters of the stator and rotor measured experimentally, which can be used to predict the dynamic motion of the stator and rotor. It captures the major features of the motor motion, and is especially useful in simulating long durations of operation with many stator-to-rotor collisions. The Finite Element Model (FEM) is based on a multiphysics model implemented in COMSOL and is used to predict additional behavior of the stator, including mode shapes, driven stator amplitude, and residual deformation. It is helpful to predict the motion of stator before fabrication and serves to validate some assumptions used in the PMM.

A.1.1.2 Flow of the Parametric Modal Model

The first step in the parametric model is to determine the parameters of the device (geometrical parameters, modal frequencies, damping factors), and then initialize the model. Subsequently, in each step, the motion of rotor and stator is estimated by a transient motion model, until a collision between the stator and rotor is determined to occur. If a collision occurs, the states after collision are calculated. If these states are such that rotor and stator separation occurs, transient motion is again calculated until the next collision point. If the states indicate that no separation occurs, further instantaneous collisions are simulated until separation does occur.

A.1.1.3 Finite Element Model

The custom magneto-mechanical finite element technique described in Chapter 2 is used to evaluate a number of stator behaviors that are used in the dynamic rotary motor model, including: deformation due to thermal expansion mismatch between the silicon and MetglasTM layers; eigenfrequency and mode shapes of the stator (both with and without thermal expansion deformation), magnetomechanical response of the stator (again, with and without thermal expansion deformation), and impulse response of the stator. For predictive design, the target stator geometry can be implemented in the FEM and analyzed. For the model verification done in this paper, the measured stator geometry is implemented and analyzed.

The following assumptions are made in deriving the dynamic model for stator and rotor interaction:

1. The teeth are treated as rectangular bodies with a negligible moment of inertia.
2. A collision occurs at the inner edge of the teeth, and the measurement of tooth motion is assumed to be at the center of mass of the tooth.

3. During contact, slippage could occur between the teeth and the rotor. The friction force is proportional to the normal force without slippage (i.e. a dry Coulomb friction model).
4. A pair of teeth, each tooth located on opposite sides of the stator, collides with the rotor at the same time with identical velocities (some randomness of each pair of teeth will later be introduced to account for non-uniformity of the fabricated system).
5. The mass distribution of the stator is uniform.
6. The damping coefficients and spring constants of the stator are mode-dependent constants.

Important parameters used in the dynamic model are introduced here at the beginning of the derivation. First, as shown in Table A-1, the velocities of the stator and rotor in tangential and vertical directions are defined, both before and after a collision occurs.

Table A-1: The definitions of different dynamic parameters of micro-motor

Parameter	Parameter description	Positive Direction
v_{rzf}	Vertical velocity of rotor, after collision	Opposite to gravity
v_{rzo}	Vertical velocity of rotor, before collision	Opposite to gravity
v_{szf}	Vertical velocity of stator at tooth position, after collision	Opposite to gravity
v_{szo}	Vertical velocity of stator at tooth position, before collision	Opposite to gravity
$v_{r\theta f}$	Tangential velocity of rotor, after collision	Clockwise
$v_{r\theta o}$	Tangential velocity of rotor, before collision	Clockwise
$v_{s\theta f}$	Tangential velocity of stator at tooth position, after collision	Clockwise
$v_{s\theta o}$	Tangential velocity of stator at tooth position, before collision	Clockwise

Four different forces are defined in the derivation. F_f stands for the friction between stator and rotor in the tangential direction and F_n stands for the normal force between the stator and rotor in vertical direction. f_m is the magnetic force acting on the stator, generated by the coils, resulting in the out-of-plane driven stator motion. f_i is the impulse force, and appears only when a vertical collision occurs between stator and rotor.

In this case, $F_n = f_i$. Fig. A-1 shows all the velocity and force parameters on the stator and rotor. Also $u(\theta, t)$ is defined as the vertical displacement of the stator as a function of time (t) at the angular position on the stator (θ). Other important definitions of stator dimensions are illustrated in Fig. A-2.

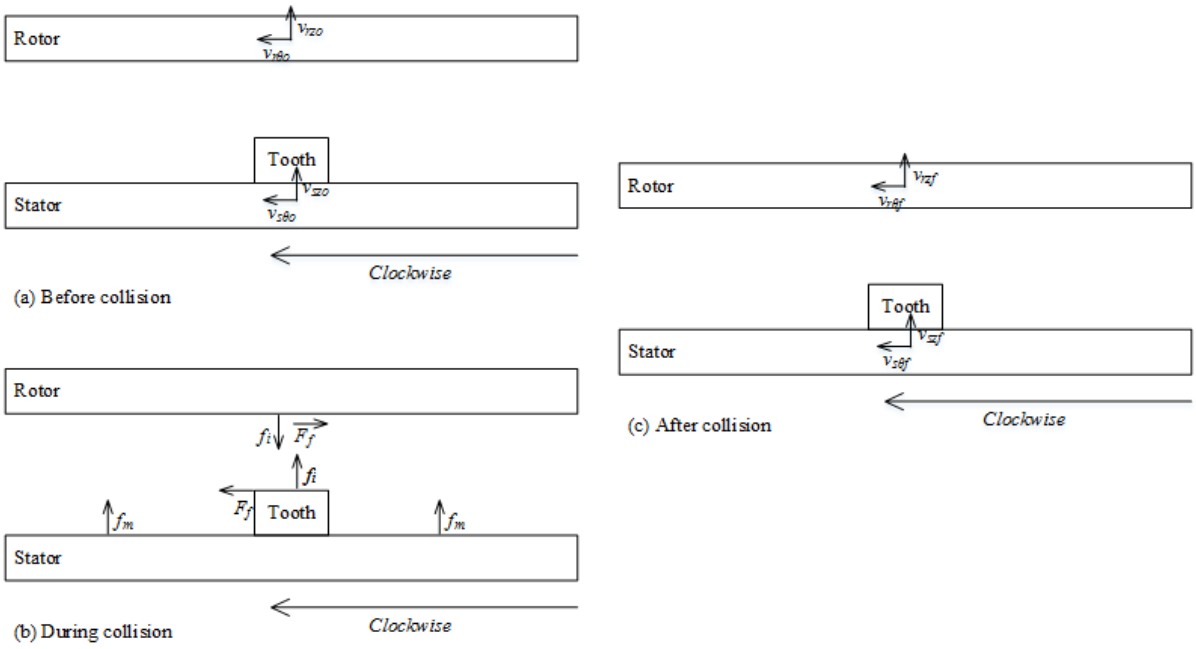

Fig. A-1: Velocities and forces occurring during motor operation: (a) directions of velocities before collision; (b) free body diagram of collision; (c) directions of velocities after collision.

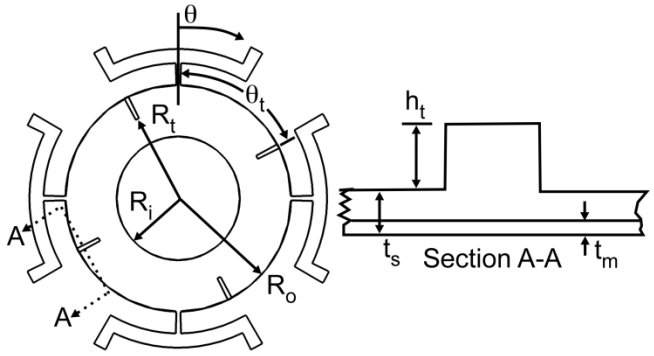

Fig. A-2: Stator geometry and key dimensional parameters.

A.1.2 Stator Geometry and Dynamics

The teeth on the stator are offset from the locations of maximum motion for both actuation modes. This offset occurs so that the teeth will move periodically under both of the actuation modes, with opposite directions between modes. When a collision between a tooth on the stator and the rotor occurs, the impact force between them changes the velocity of the rotor and stator both vertically and tangentially. A series of these collisions over time continues to transfer overall positive angular momentum to the rotor during operation.

A.1.2.1 FEA results: Resonant Mode Shapes and Static Deformation

The dynamic model introduced here is applicable to a standing wave motor as described in Chapters 2 and 3. Via the applied magnetic field or as a result of collisions between the teeth and the rotor, different vibration modes of the stator can be excited (Fig. A-3). The lowest frequency mode excited, referred to as mode A in this appendix, is a pseudo-rigid-body motion of the entire stator ring. The magnetoelastically-driven modes are the ones used to generate the rotary motion and are referred to as modes B and C in this appendix. Two other tilting modes exist between mode A and modes B and C; however, these are not strongly excited by the symmetric collisions nor by the driving magnetic field. In the prototype motor studied, mode B occurs at about 6.3 kHz and has its maximum vibration position located between the suspensions connections; this mode shape causes the rotor to rotate clockwise. Mode C occurs at about 7.4 kHz and has its maximum vibration positions at the connections of the stator to the suspension; mode C causes the rotor to rotate counter-clockwise.

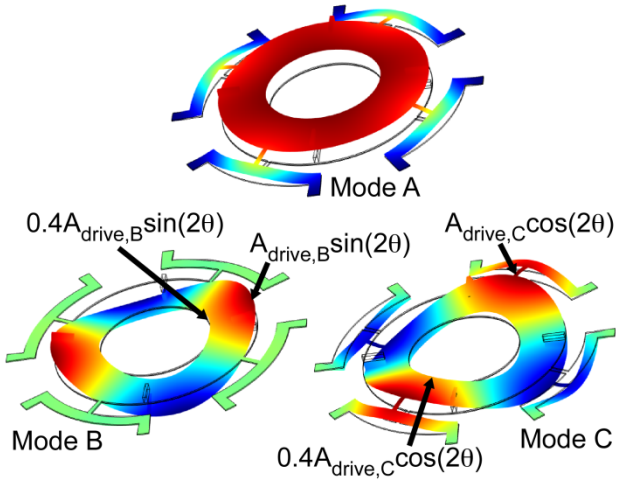

Fig. A-3: Excited stator mode shapes: (1) pseudo-rigid-body mode (first mode, mode A); (2) first actuation mode (fourth mode, mode B, clockwise); (3) second actuation mode (fifth mode, mode C, counterclockwise).

Eigenfrequencies and mode shapes for the stator can also be calculated using the FEM. For modes B and C, the driving magnetic field is implemented by assigning a surface current to the curved surface of a cylindrical domain positioned around the stator, with the long axis of the cylinder in the direction of the driving field. The surface current density amplitude is specified such that the resulting magnetic field amplitude is the same as that generated by the experimentally-used Helmholtz coils at the position of the motor. For mode A, a periodic force is applied to the top surfaces of the teeth in order to excite that mode shape. A frequency sweep analysis is performed near the eigenfrequencies of interest to estimate the steady-state amplitude of the driven mode shapes, and to estimate the quality factor (and associated damping coefficient) of the resonant peaks.

An analysis of the unstressed stator (neglecting thermal expansion mismatch) and an analysis of the pre-stressed stator were performed. Calculated mode shapes, evaluated as displacements from the unstressed or pre-stressed state, were identical for both analyses; however, the pre-stressed eigenfrequency analysis exhibited higher modal frequencies for each shape. It was also found that the driven amplitudes, mode shapes,

and quality factors were not significantly different between unstressed and pre-stressed analyses. The residual deformation leads to the assumption that the collision between stator and rotor happens at the inner edge of the teeth (Fig. A-4).

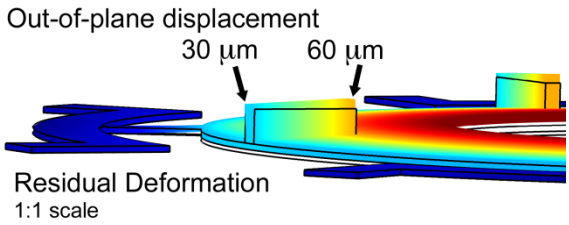

Fig. A-4: residual deformation of the stator from FEA.

A.1.2.2 Tooth Directional Relationships

The relation between tangential and vertical motion of the stator teeth becomes useful in deriving momentum transfer effects, and can be derived from the geometry of the stator before dynamic interactions are considered (Fig. A-2). The stator vibrates in a given mode shape with the amplitude of out-of-plane motion of the neutral axis (A) described by a sinusoidal function of angular (θ) and radial (r) position,

$$A = A_i + \frac{(A_o - A_i)(r - R_i)}{R_o - R_i} \tag{A-1}$$

where R_i and R_o are the inner and outer radii of the stator, and A_i and A_o are the amplitudes of displacement at the inner and outer radii of the stator, respectively, of its antinodes of vibration. These amplitudes are determined by the driving field strength and geometry.

During vibration, the tooth tilts through an angle of amplitude (θ_{tilt}). This tilting angle will cause both vertical (δz) and tangential ($\delta\theta$) motion. The motion is periodic, the amplitude of which can be described as follows:

$$\delta\theta = \frac{t_s + 2h_t}{2} sin\ (\theta_{tilt}) \tag{A-2a}$$

$$\delta z = A\cos(2\theta_t) + \frac{t_s+2h_t}{2}(\cos(\theta_{tilt}) - 1) \quad \text{(A-2b)}$$

The tilt angle amplitude is the derivative of the vertical displacement with respect to the tangential displacement at tooth position (r) when the small angle approximation is made for θ_{tilt}.

$$\tan(\theta_{tilt}) = \frac{\partial \delta z}{\partial r \theta_t} = \frac{-2A\sin(2\theta_t)}{r} \quad \text{(A-3)}$$

Also the radial position (r) is the inner radius of tooth mass (R_t) because of the residual deformation of stator caused by the stress remained in the stator from fabrication:

$$\theta_{tilt} \approx \tan(\theta_{tilt}) = \frac{-2A\sin(2\theta_t)}{R_t} \quad \text{(A-4)}$$

$$\delta\theta = \frac{t_s+h_t}{2}\sin(\theta_{tilt}) \approx \frac{A(t_s+2h_t)\sin(2\theta_t)}{R_t} \quad \text{(A-5a)}$$

$$\delta z = A\cos(2\theta_t) + \frac{t_s+2h_t}{2}(\cos(\theta_{tilt}) - 1) \approx A\cos(2\theta_t) \quad \text{(A-5b)}$$

Hence, tangential and vertical motions are related by the stator geometric parameters.

A.1.2.3 Steady State Motion

Steady state motion of the stator is generated only when it is under the influence of a steady state magnetic field alone. While the actual magnetic force on the stator cannot be measured accurately, by assuming the stator as a mass-spring-damper system, its magnitude can be inferred by observing the steady-state motion of different positions on the stator before the rotor is present. Given the proposed model of the stator, the displacement of a given position on stator is expected to be a sinusoidal function with respect to time, while the relation between the amplitude of vertical and tangential motion is derived from the geometry of the stator.

The stator motion at each tooth position is periodic under a driving magnetic field of a certain frequency (f), so the position of the tooth during steady-state motion in vertical ($x_{sz,ss}$) and tangential ($x_{s\theta,ss}$) directions can be described as follows:

$$x_{sz,ss} = A\cos(2\theta_t)\sin(2\pi f t) \tag{A-6a}$$

$$x_{s\theta,ss} = \frac{A(t_s+2h_t)\sin(2\theta_t)}{r}\sin(2\pi f t) \tag{A-6b}$$

And the stator vertical ($v_{sz,ss}$) and tangential ($v_{s\theta,ss}$) velocity at tooth position is just the derivative of the position

$$v_{sz,ss} = 2\pi f A\cos(2\theta_t)\cos(2\pi f t) \tag{A-7a}$$

$$v_{s\theta,ss} = \frac{2\pi f A(t_s+2h_t)\sin(2\theta_t)}{r}\cos(2\pi f t) \tag{A-7b}$$

The upward direction is positive for vertical motion and velocity, and the clockwise direction is positive for tangential motion and velocity.

A.1.2.4 Stator Impulse Response

The stator is treated as a ring with uniform mass distribution. Once the inertia of the teeth is assumed to be negligible, it is reasonable to model the stator as a linear mass-spring-damper system with respect to angle (θ) and time (t):

$$m\ddot{u}(\theta,t) + b(\theta)\dot{u}(\theta,t) + k(\theta)u(\theta,t) = f_m + f_i \tag{A-8}$$

in which mass (m), damping coefficient (b), the spring constant (k), and both forces f_m (magnetic force from the coil) and f_i (impulsive force due to collision with the rotor) are given in units per angle. For example, m is defined as $\frac{m_s}{2\pi}$, in which m_s is the mass of the stator.

Taking the displacement of the stator at the inner radius of the tooth (R_t) as a function of time and angle ($u(\theta,t)$), the displacement can be decoupled into a combination of three different modes,

$$u(\theta,t) = g_A(t) + g_B(t)\sin(2\theta) + g_C(t)\cos(2\theta) \quad \text{(A-9)}$$

in which the first mode is the pseudo-rigid-body motion (mode A), and the terms with $\sin(2\theta)$ and $\cos(2\theta)$ correspond to the two actuation modes (modes B and C).

The impulsive force between the stator and the rotor, acting on the stator, can be determined by linear momentum conservation at the rotor. Describing the impulse force f_i as force per angle, the expression for momentum transfer from an impulse impact between the rotor and stator becomes as follows:

$$f_i = -\frac{m_r(v_{rf}-v_{ro})\delta(t-t_c)}{2\Delta\theta} \quad \text{(A-11a)}$$

Here, the interaction force is placed at the tooth position, θ_t, and determined by the rotor velocity before (v_{ro}) and after (v_{rf}) collision. $\delta(t-t_c)$ is the Dirac delta function defined at the collision time (t_c). When wobble and tilting of the rotor are insignificant, two teeth in each set are assumed to be identical to each other, and the rotor will collide with both teeth in a set simultaneously. The interaction force is assumed to act on the entire arc length of the tooth in angle direction at lateral surface, occupying angle of $\Delta\theta$. Therefore the force could be expressed as a function of pulse train with amplitude $-\frac{1}{2}m_r(v_{rf}-v_{ro})$, duty cycle ($\Delta\theta$) and period ($\pi$).

Applying a Fourier series expansion to the spatial distribution of the interaction force, (A-11a) becomes

$$f_i = -\frac{1}{2\Delta\theta}m_r(v_{rf}-v_{ro})\delta(t-t_c)\left[\frac{\Delta\theta}{\pi} + \sum_{n=1}^{\infty}\frac{2}{n\pi}sin(n\Delta\theta)\cos\big(2n(\theta-\theta_t)\big)\right] \quad \text{(A-11b)}$$

For $\Delta\theta \ll \pi$, (A-11b) simplifies to:

$$f_i \approx -\frac{1}{2}m_r(v_{rf}-v_{ro})\delta(t-t_c)\left[\frac{1}{\pi} + \sum_{n=1}^{\infty}\left\{\frac{2}{\pi}cos(2n\theta)\,cos(2n\theta_t) + sin(2n\theta)\,sin(2n\theta_t)\right\}\right] \quad \text{(A-11c)}$$

Only the first three terms in the Fourier series are listed here because only the response of the rigid body and actuation modes are important in this model, and later

terms are small enough to be neglected because the frequencies of the later terms are well-separated higher modes which are difficult to excite and relatively small in amplitude. The interaction force is thus finally reduced to the form:

$$f_i \approx -\frac{1}{2}m_r(v_{rf}-v_{ro})\delta(t-t_c)[\frac{1}{\pi}+\frac{2}{\pi}cos(2\theta)\,cos(2\theta_t)+sin(2\theta)\,sin(2n\theta_t)] \quad \text{(A-11d)}$$

From the assumption that the damping coefficient (b) and the spring constant (k) are constants depending on the modes, the second order linear equation of the stator can be decoupled into three second order linear equations with different damping coefficients and spring constants. Since all terms in (A-9), (A-10), (A-11d) in this system are known, the second order linear equation of motion of the system in (A-8) can be decoupled into three equations:

$$m\ddot{g_A}(t)+b_A\dot{g_A}(t)+k_Ag_A(t)=-\frac{1}{2\pi}m_r(v_{rzf}-v_{rzo})\delta(t-t_c) \quad \text{(A-12a)}$$

$$m\ddot{g_B}(t)+b_B\dot{g_B}(t)+k_Bg_B(t)=-\frac{1}{\pi}m_r\big(v_{rzf}-v_{rzo}\big)\delta(t-t_c)\,sin(2\theta_t)+f_{mB}\,sin(2\pi f_Bt) \quad \text{(A-12b)}$$

$$m\ddot{g_C}(t)+b_C\dot{g_C}(t)+k_Cg_C(t)=-\frac{1}{\pi}m_r\big(v_{rzf}-v_{rzo}\big)\delta(t-t_c)\,cos(2\theta_t)+f_{mC}\,sin(2\pi f_Ct) \quad \text{(A-12c)}$$

The response of each equation can be superposed as the sum of responses under the magnetic force and interaction force. The magnetic force response is the steady state response to a second order linear equation and the interaction force response is the impulse response.

A.1.3 Collision Model

Before deriving the collision model, the coefficient of restitution and friction need to be defined. Then the closed-form solution of the dynamic model can be solved and used in later simulation.

Coefficient of restitution: By definition, the coefficient of restitution equals the ratio of the relative velocity in the normal direction after collision to the relative velocity in the vertical direction after collision:

$$e = \frac{v_{rzf} - v_{szf}}{v_{szo} - v_{rzo}} \tag{A-13}$$

in which v_{rzf} and v_{szf} is the velocity of rotor and stator after collision, v_{rzo} and v_{szo} is the velocity of rotor and stator before collision.

Coefficient of friction: A dry (Coulomb) friction model is assumed, and no slippage occurs between the tooth and the rotor during the collision. Thus, the relationship between the normal force and the friction can be described in the following equation:

$$F_f = \mu F_n \tag{A-14}$$

A.1.3.1 Model Derivation

When the rotor is present, the vertical stator displacements due to a collision is modeled as the sum of impulse responses for the three equations decoupled from the original system equation (A-12a-c):

$$u_i(\theta, t) = \frac{2\pi F}{m_s \omega_{d,A}} e^{-\xi_A \omega_A} \sin(\omega_{d,A} t) + \frac{4\pi F}{m_s \omega_{d,B}} e^{-\xi_B \omega_B} \sin(\omega_{d,B} t)\, sin(2\theta_t) \sin(2\theta) + \frac{4\pi F}{m_s \omega_{d,C}} e^{-\xi_C \omega_C} \sin(\omega_{d,C} t)\, cos(2\theta_t)\, cos(2\theta) \tag{A-15}$$

in which $F = -\frac{1}{2} m_r (v_{rf} - v_{ro}) \frac{1}{\pi}$, $\omega_n = 2\pi f_n = \sqrt{\frac{k_n}{m_n}}$, $\omega_{d,n} = \omega_n \sqrt{1 - \xi_n}$, $\xi_n = \frac{b_n}{2 m_n \omega_n}$, *n=A, B or C*

Likewise, the tangential response can be found as a combination of three responses. Because the vertical and the tangential motion of the tooth on the stator are related, the relation between v_{szf} (vertical velocity of the tooth) and $v_{s\theta f}$ (tangential

velocity of the tooth) for each single mode is derived from the geometry of the stator, as shown in (A-7), as:

$$v_{s\theta f} = \frac{tan(2\theta_t)(t_s+h_t)}{r} v_{szf} \tag{A-16}$$

Here, we define the ratio between v_{szf} and $v_{s\theta f}$ as $K = \frac{tan(2\theta_t)(t_s+h_t)}{r}$ to simplify later notation. Mode A results in vertical tooth motion only, as there is no tooth tilting associated with the mode, and the two actuation modes will have tangential motions in opposite directions. By considering the direction of tangential motion of each mode, the tangential motion in the clockwise direction of the stator at tooth position can be written as:

$$u_{i,tangential}(t) = \frac{4\pi FK}{m_s\omega_{d,B}} e^{-\xi_B \omega_B} \sin(\omega_{d,B}t)\, sin(2\theta_t)^2 - \frac{4\pi FK}{m_C\omega_{d,C}} e^{-\xi_C \omega_C} \sin(\omega_{d,C}t)\, cos(2\theta_t)^2 \tag{A-17}$$

After determining the analytical solution of the stator motion, the change of velocity at the tooth position right after a collision can be derived from (A-15) in analytical form:

$$\dot{u_\iota}(\theta_t, 0) = \frac{2\pi F}{m_s} + \frac{4\pi F}{m_s} sin^2(2\theta_t) + \frac{4\pi F}{m_s} cos^2(2\theta_t) \tag{A-18a}$$

This expression can be simplified to a form with change of rotor velocity and the mass of rotor and stator only:

$$\dot{u_\iota}(\theta_t, 0) = -\frac{3m_r}{m_s}(v_{rzf} - v_{rzo}) \tag{A-18b}$$

Defining a ratio of mass r_m from (A-18b) as $r_m = \frac{3m_r}{m_s}$, then the relation between the velocities of the stator/rotor before/after collision is derived:

$$r_m(v_{rzf} - v_{rzo}) = -(v_{szf} - v_{szo}) \tag{A-19}$$

Given the definition of the coefficient of restitution from (A-13) and the equation (A-19), the expression for v_{szf} (stator velocity after collision at tooth position) can be derived:

$$v_{szf} = \frac{v_{szo} - r_m(ev_{szo} - (e+1)v_{rzo})}{1+r_m} \tag{A-20a}$$

Also, the expression of v_{rf} can be derived from (A-13) and (A-19):

$$v_{rzf} = e(v_{szo} - v_{rzo}) + v_{szf} \tag{A-20b}$$

Finally, the $v_{r\theta f}$ (tangential velocity of the rotor after collision) can also be written as a function of $v_{r\theta o}$ (tangential velocity of the rotor before collision), depending on whether the friction exceeds the maximum allowance (i.e. whether static or kinetic friction is occurring):

$$v_{r\theta f} = \begin{cases} v_{r\theta o} + \frac{\mu m_r (v_{rzf} - v_{rzo}) r}{J} & if\ \mu < \tan(\alpha) \\ v_{r\theta o} + \frac{tan(\alpha) m_r (v_{rzf} - v_{rzo}) r}{J} & if\ \mu > \tan(\alpha) \end{cases} \tag{A-20c}$$

in which α is the angle between the vertical direction and the interaction the force acting on the rotor. The α at each collision is defined as the ratio of the tangential and vertical displacement of the stator at tooth position.

A.1.4 Rotor Geometry and Dynamics

In the basic actuator, the rotor is just a disc with some small features on the top surface for optical testing purposes, so only the mass (m_r) and radius of the collision point (r, same as the radius of collision position on stator) are considered in vertical direction model and the momentum of inertia (J_r) for the tangential rotation.

After a collision, the transient motion of rotor is a ballistic motion affected by the gravity force, squeeze film damping force and the drag force. The squeeze film damping force and the drag force are mainly produced by the air between the stator and rotor. The

free body diagrams of the rotor are shown in Fig. A-5. The vertical velocity (v_{rz}) and tangential velocity ($v_{r\theta}$) can be written as follows:

$$m_r \dot{v_{rz}} = -m_r g - b_z v_{rz} \tag{A-21a}$$

$$J_r \dot{\omega_{r\theta}} = -b_\theta \omega_{r\theta} \qquad \text{with} \quad \alpha_{r\theta} = \dot{\omega_{r\theta}} \qquad \omega_{r\theta} = \frac{v_{r\theta}}{r} \tag{A-21b}$$

in which b_z and b_θ are the damping coefficients in the vertical and tangential directions.

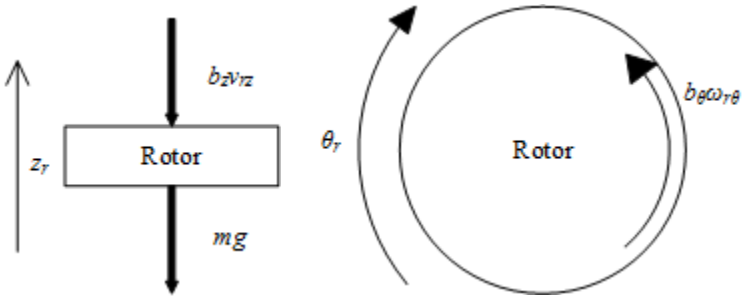

Fig. A-5: (a) free body diagram of the rotor transient motion in a vertical direction; (b) free body diagram of the rotor transient motion in a tangential direction.

A.1.4.1 Parameter Identification

Before running the simulation of the model, several system parameters must be defined when comparing results to experimental measurements. Parameters can be determined either from prior literature, such as coefficient of restitution and coefficient of friction, or experimentally, such as rotor mass or stator steady-state vibration amplitude.

Coefficient of Restitution: In general, coefficients of restitution may range from 0 to 1. These coefficients depend on the speed of collision, the materials, and the geometries of the surfaces involved in the collision. Previous studies have shown the coefficient of restitution of collisions between poly-silicon and silicon micro-geometries to range from 0.57 to 0.642 [Den10, Lee93]. Within that range, Coefficient of restitution can be used as a tuning parameter in this model to better match the measured results.

Coefficient of Friction: The coefficient of friction (μ) for silicon-on-silicon interaction has been shown to vary widely depending on the exact conditions of the

interaction, from 0.03 to 0.69 [Bhu96, 97]. This coefficient thus can also be considered as a tuning parameter for this model.

Rotor mass: The mass of the rotor can be measured accurately as a discrete component. It is measured to be 46 ± 0.5 mg. However, the mass of the stator is estimated from the stator geometry, which is about 10.7 mg in this case. The formula to determine the stator mass is the following:

$$m_s = \pi\left(R_o^2 - R_i^2\right)(\rho_m t_m + \rho_s t_s) + 4\pi(R_o^2 - R_t^2)\rho_s \theta_{to}/180° \quad \text{(A-22)}$$

in which R_o, R_i, R_t is the stator outer, stator inner, tooth inner radius; θ_{to} is the angle each tooth occupied, which is 2.6°; the ρ_m and ρ_s is the density of Metglas™ 2826MB and silicon, which is 7900 kg/m^3 and 2330 kg/m^3 [Met08].

Squeeze film damping and Drag coefficients: From previous literature the squeeze film damping coefficient can be approximated a few different ways [Bao07, Gri66];

$$b_z = \frac{48\eta R_o(1+\beta)(1-\beta)^3}{\pi^3 d^3} \approx 0.6 \text{ mNs/m} \quad \text{(A-23a)}$$

in which $\beta = \frac{R_i}{R_o}$, the air viscosity (η) is assumed to be $1.983 * 10^{-5}$ at 300K and d is the distance between rotor and stator. A second model used to estimate b_z, from [Gri66], was:

$$b_z = \frac{4.45}{d^3}\eta\left(R_o^4 - R_i^4\right) \approx 3.6 \text{ mNs/m} \quad \text{(A-23b)}$$

For the two cases, the coefficient varies from 0.6 to 3.6 mNs/m. Due to the wide range of reasonable damping coefficients, this parameter was also treated as a tuning parameter for the model.

The viscous drag from air acting to oppose tangential motion was estimated by integrating drag forces about the circumference of the hub:

$$b_\theta = \int \frac{r\, dF}{\omega} = \int \frac{r^2\eta}{d} dA = \frac{2\pi\eta}{d}\int r^3 dr = \frac{\pi\eta(R_o^4 - R_i^4)}{2d} \approx 4.3 * 10^{-11} \quad \text{(A-24)}$$

in which ω is the angular velocity of the rotor, J is the momentum of the viscous drag, and dF is the viscous drag force at each area dA.

The steady state motion of the stator in magnetic field is measured experimentally. The mode frequencies and amplitudes of the stator are measured experimentally by giving a frequency sweep to the sinusoidal voltage input and measuring the motion response of the stator. These results allow the model assignation of modal frequencies, damping parameters, and steady state amplitudes.

From previous studies, analytical solutions and experiment results, the system parameters could be determined for simulation. The full description of the system parameters are shown in Table A-2(a-c). The value of parameters used in a nominal simulation is listed in the column "Simulation".

Table A-2(a): Motor geometric parameters used in simulation

Parameter (Symbol)	Range	Simulation	Method to determine
Stator inner radius (R_i)	2.13 ±0.02 mm	2.125 mm	Measured
Stator outer radius (R_o)	3.89 ±0.02 mm	3.89 mm	Measured
Tooth inner radius (R_t)	3.06 ±0.02 mm	3.063 mm	Measured
Stator thickness (t_s)	70 ±10 um	70 um	Measured
Tooth height (h_t)	260 ±10 um	260 um	Measured
Tooth location angle (θ_t)	27.37 ±0.2 °	27.365°	Measured
Mode shift angle (θ_m)	0 ±3 °	2.5°	Estimated

Table A-2(b): Motor frequency response parameters used in simulation

Parameter (Symbol)	Range	Simulation	Method to determine
Mode A frequency (f_A)	2150 ±10 Hz	2150 Hz	FEA
Mode A damping ratio (ξ_A)	0.0225 ± 0.0014	0.0225	FEA
Mode B frequency (f_B)	6.30 ± 0.01 kHz	6.30 kHz	Measured
Mode B tooth amplitude	20.72 ± 1.24 µm	20.72 µm	Measured
Mode C frequency (f_C)	7.46 ± 0.01 kHz	7.46 kHz	Measured
Mode C tooth amplitude	1.81 ± 0.11µm	1.81 µm	Measured
Mode B & C damping ratio (ξ_B ξ_C)	0.0050 - 0.0077	0.0063 (ξ_B) 0.0075 (ξ_C)	Measured

Table A-2(c): Motor properties used in simulation

Parameter (Symbol)	Range	Simulation	Method to determine
Rotor mass (m_r)	46 ± 0.5 mg	46 mg	Measured
Stator mass (m_s)	10.7 ± 1.0 mg	10.7 mg	Eq. (24)
Coefficient of restitution (e)	0.570 - 0.642	0.6	[Dem10, Lee93]
Coefficient of friction (μ)	0.03 - 0.69	0.4	[Bhu96, 97]]
Squeeze film damping coefficient (b_z)	0.6 - 3.6 mNs/m	3.6 mNs/m	Eq. (25a) (25b)
Air viscous drag (b_θ)	4.3×10^{-11} Ns/m	4.3×10^{-11} Ns/m	Eq. (26)

A.1.5 Typical Model Output

A.1.5.1 Simulation Features and Trends

Using the parameters in Table A-2(a-c), a simulation code was developed in Matlab to simulate the dynamic behavior of the micro-motor. Fig. A-6 shows sample results from the simulated rotor motion. The vertical motion of the rotor can be recognized as a ballistic motion (Fig. A-6(a), (b)), with the vertical velocity having a sudden change at impacts and deceleration otherwise nearly constant, differing only from deceleration due to the gravity and the squeeze film damping effect. The tangential velocity is accelerated at beginning and eventually oscillates around a steady state value (Fig. A-6(c)).

After generating the time domain simulation results, a Fast Fourier Transform (FFT) was applied to the results to obtain a frequency spectrum for motion (Fig. A-6(d)), which can used to check the reliability of the model quantitatively against experimental results. Because stochastic variation prevents a one-to-one comparison of experimental and simulated time domain data sets, statistical comparisons are made to validate model predictions against experimentally observed behavior. These comparisons are made by first applying a FFT algorithm to each data set. In the frequency domain, collision frequency distribution and vertical motion amplitude were checked, in particular from the frequency and amplitude of the peak vertical motion in frequency domain. Detailed

simulation results will be further discussed in the next section, when assessing experiment validation.

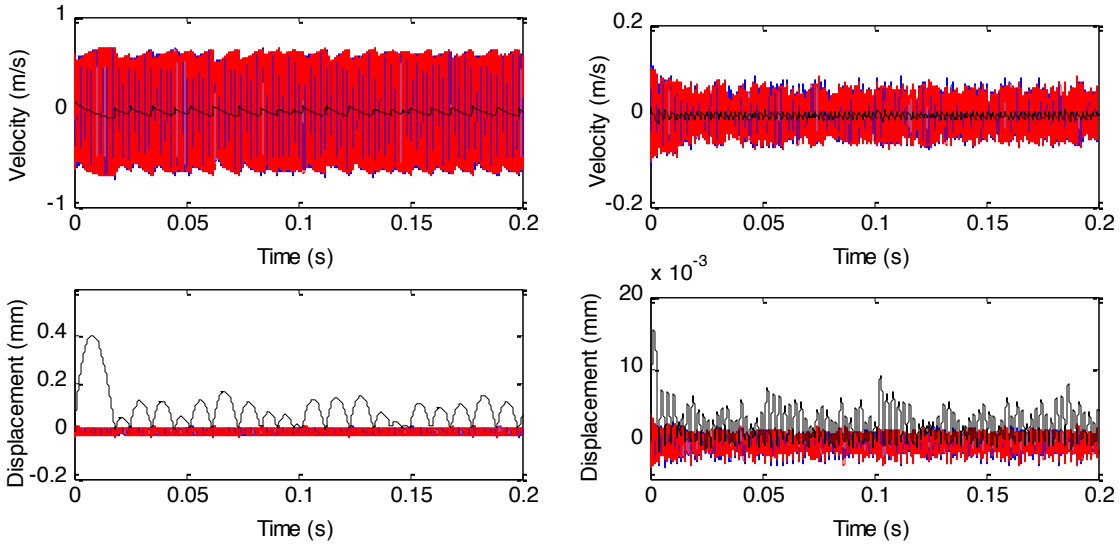

Figure A-6(a): Sample simulation of tangential velocity and displacement in time domain (mode B on the left and mode C on the right). The black line stands for the displacement/velocity of the rotor, red and blue lines stand for the displacements/velocities of the two sets of teeth.

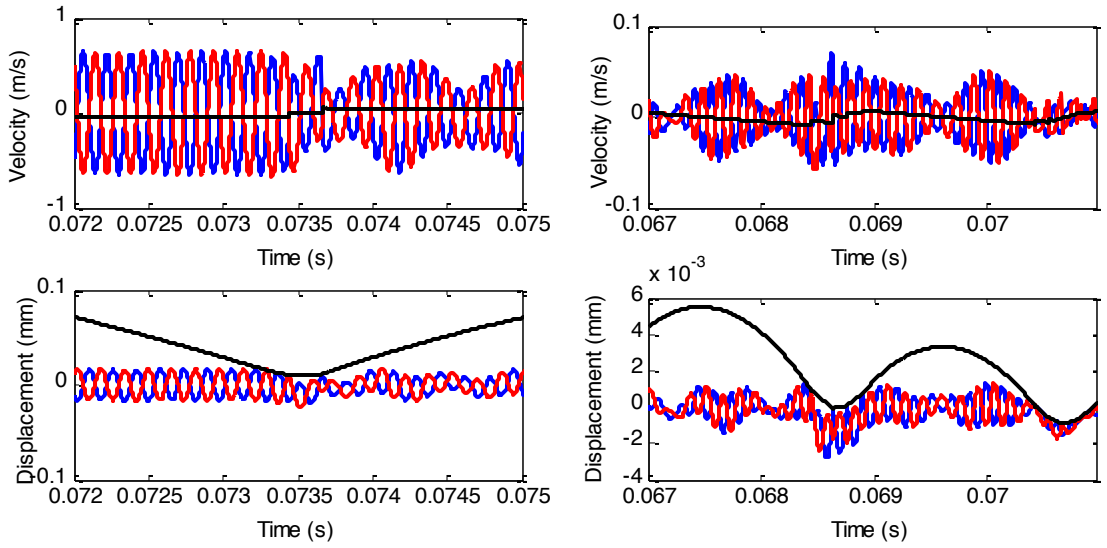

Fig. A-6(b): Zoom in around collisions in time domain (mode B and mode C). Black lines stand for the displacement/velocity of the rotor, red and blue line stands for the displacements/velocities of two sets of tooth.

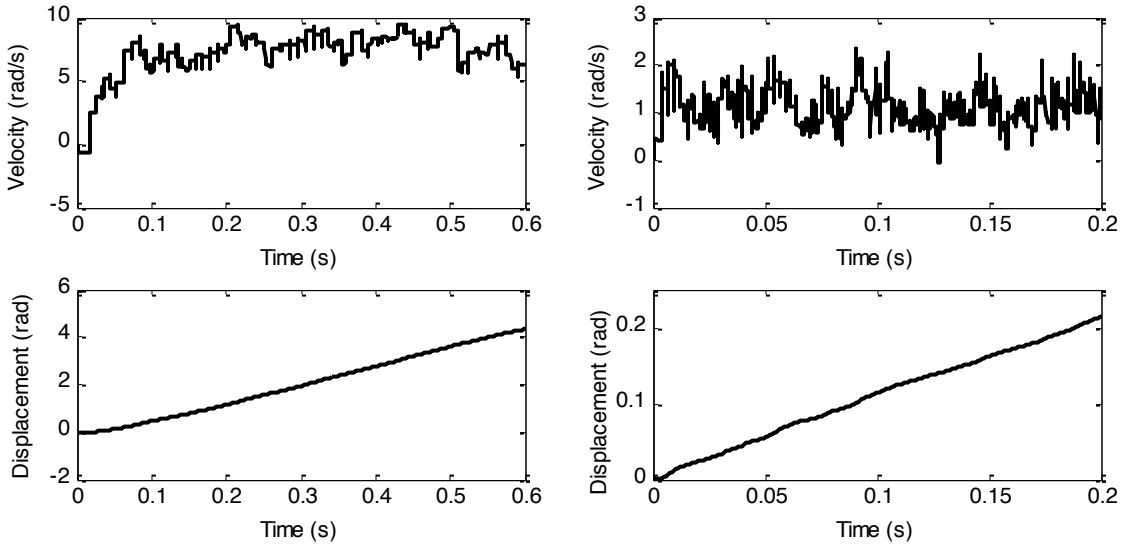

Fig. A-6(c): Sample simulations of angular velocity and angle rotated in tangential direction (mode B and mode C).

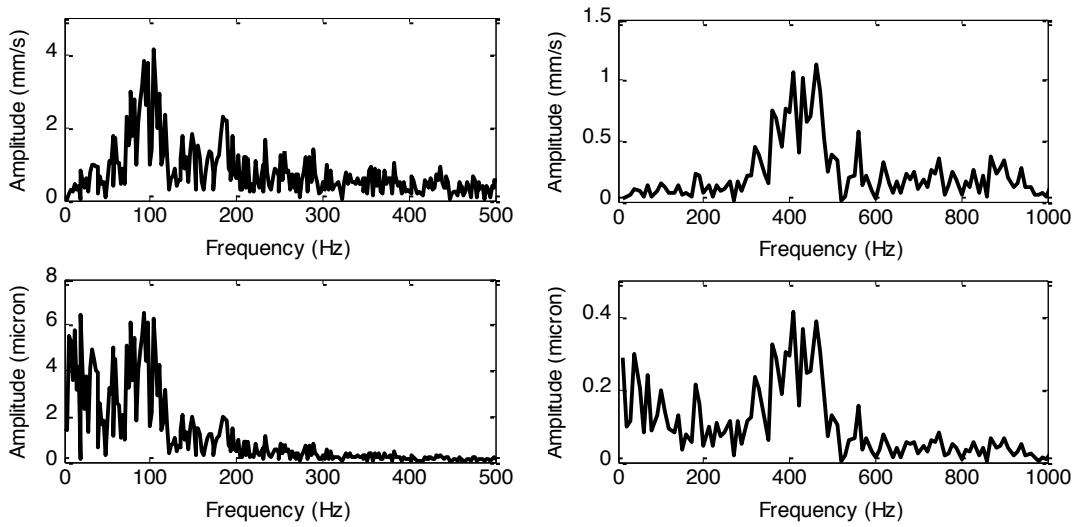

Fig. A-6(d): Frequency domain velocity and displacement from simulated rotor motion (mode B and mode C).

A.2 Experimental Validation

A.2.1 Experimental Design and Setup

An experimental system is used to check the reliability of the simulation. Vertical motions of multiple points on the unloaded stator are measured by a Laser Doppler Vibrometer (LDV) to check the accuracy of the stator FEA model. Then, vertical motion near the center point on the rotor is measured, when the micro-motor is in place and

rotating. Comparison of the motion of rotor, particularly in the vertical direction, is used to validate the model of the micro-motor.

The LDV used in the experiment is Polytec OFV 303 sensor head and Polytec OFV 3001 S vibrometer controller. The voltage amplifier used in the experiment to provide voltage to the Helmholtz coils is a Krohn-Hite Model 7500. The magnetic field amplitude generated by the coils at the position of the motor is measured to be 8 Oe typically, by a gaussmeter (F.W. Bell model 5170)

In addition to the LDV, a microscope with a high-speed camera (Photron FASTCAM MC2.1 and LEICA 104459290.5x) is used to track rotation of the rotor. The resolution of the camera is approximately 2 micron. A coil is used to generate the sinusoidal magnetic field at actuation frequency by being supplied with a sinusoidal voltage signal. The entire experimental setup is shown in Fig. A-7.

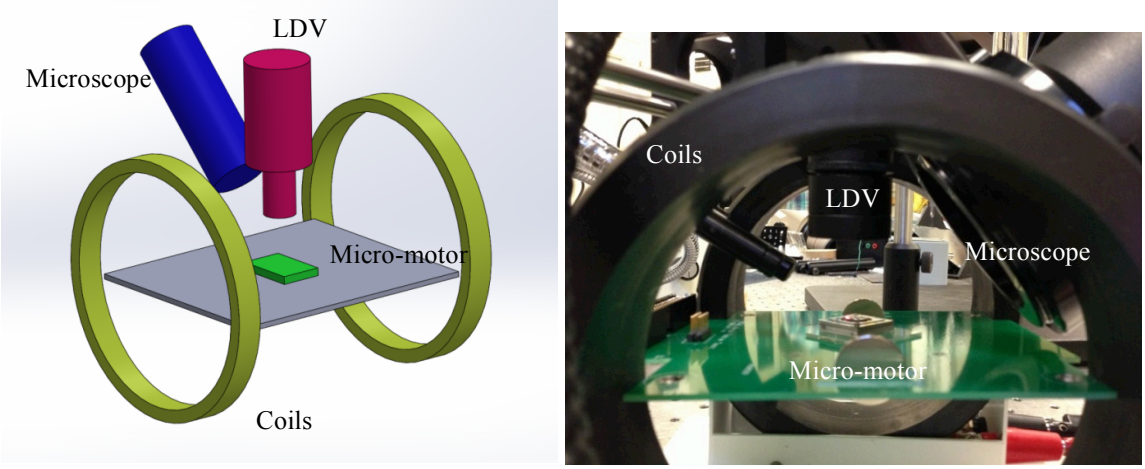

Fig. A-7: (a) Experimental set-up scheme with LDV (red) and microscope (blue). The micro-motor (green) is actuated by the voltage signal in the coiling (yellow); (b) photo of the experimental set-up.

A.2.1 Experimental Results and Comparison to Model

A.2.1.1 Velocity and Displacement

Results from experimental measurement of vertical rotor velocity are shown in Fig. A-8 and Fig. A-9 for modes B and C, respectively. The displacement of the rotor is calculated by integrating the velocity over time (shown in Fig. A-8 (left) and Fig. A-9 (left)). With simulation results, an FFT is also applied to the experimental measurement. The peak frequency in the resulting FFT spectrum is considered the representative collision frequency for the data set. The amplitude at the peak frequency is also a point of comparison between data sets. The FFTs of typical experimental and simulation results are shown in Fig. A-8 (right) and Fig. A-9 (right).

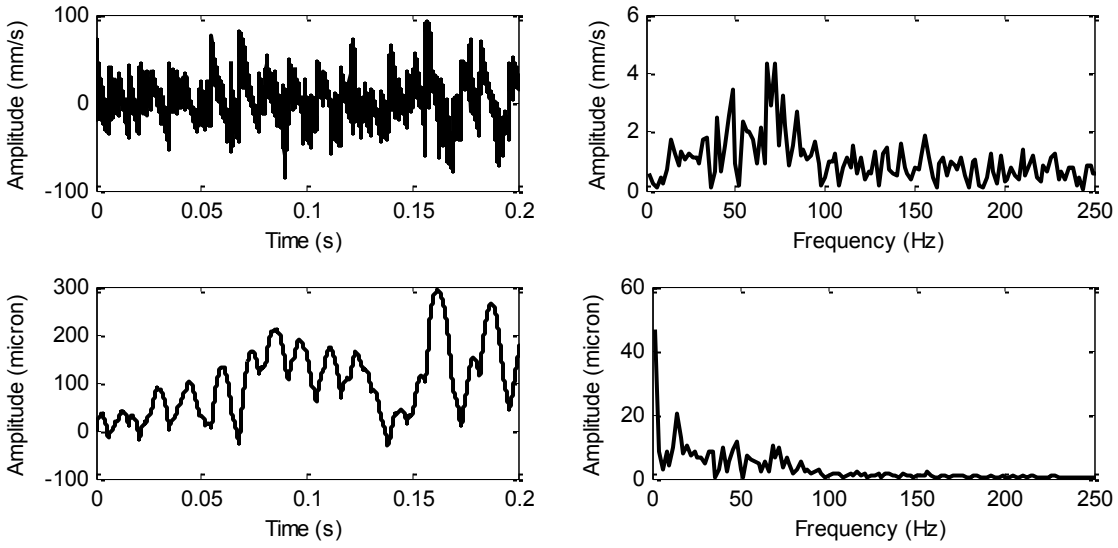

Fig. A-8: (left) typical time domain experimental velocity and displacement under mode B; (right) frequency domain experimental velocity and displacement under mode B.

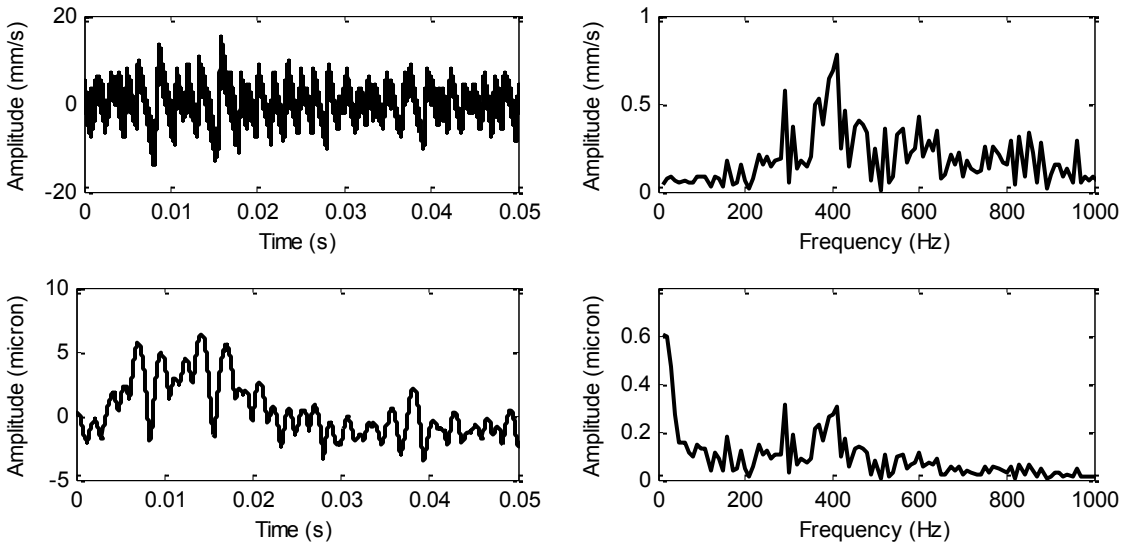

Fig. A-9: (left) typical time domain experimental velocity and displacement under mode C; (right) frequency domain experimental velocity and displacement under mode C.

Tangential velocities are measured by the high-speed camera at frame rates of 5000 fps (mode B) and 10000 fps (mode C). The average tangential velocity measured by the camera is listed in Table A-3. The average and error based on the standard deviation of three experimental data sets presented.

Table A-3: Experimentally measured results

Rotor behavior	Experiment
Mode B collision frequency	76 ± 20Hz
Mode B collision amplitude	3.94 ± 0.57 mm/s
Mode B tangential velocity	~1 rad/s
Mode C collision frequency	400 ± 104 Hz
Mode C collision amplitude	0.88 ± 0.28 mm/s
Mode C tangential velocity	~1.4 rad/s

A.2.1.2 Comparison between simulation and experimental results

The collision frequency is well predicted by this dynamic model for both mode B and mode C (Table A-4, Fig. A-10 and Fig. A-11). The average simulated vertical rotor velocities of both mode B and mode C are larger than average of the experimental results, although standard deviations do significantly overlap. These small differences may be caused by not including in the model all sources of friction on the rotor (e.g., friction

between the hub and the rotor). The average and error are based on the standard deviation of five simulated and three experimental data sets.

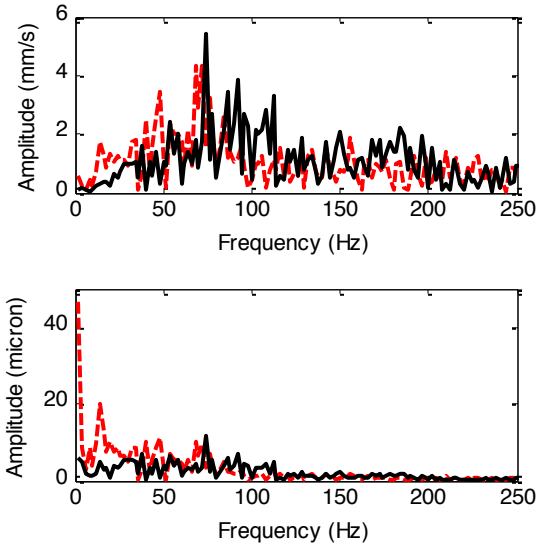

Fig. A-10: Frequency spectrum of simulated (black solid line) and experimental (red dash line) velocity and displacement under mode B.

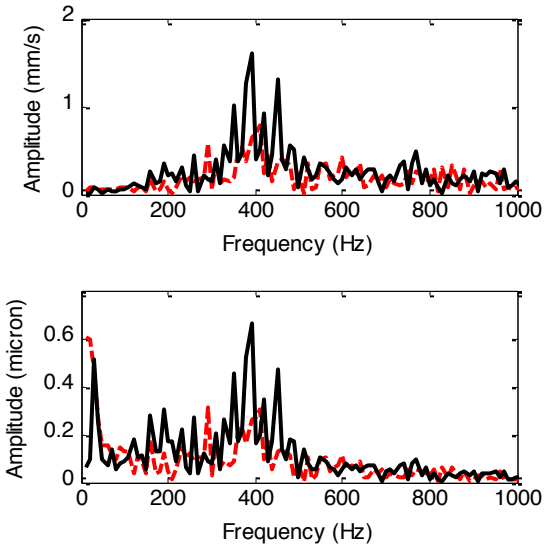

Fig. A-11: Frequency spectrum of simulated (black solid line) and experimental (red dash line) velocity and displacement under mode C.

Table A-4: Comparison of simulated and experimental results

Motor behavior	Simulated	Experiment
Mode B collision frequency	88.8 ± 7.13 Hz	76 ± 20Hz
Mode B collision amplitude	4.08 ± 1.17 mm/s	3.94 ± 0.57 mm/s
Mode B tangential velocity	8.01 ± 0.63 rad/s	~1 rad/s
Mode C collision frequency	422 ± 51.8 Hz	400 ± 104 Hz
Mode C collision amplitude	1.48 ± 0.26 mm/s	0.88 ± 0.28 mm/s
Mode C tangential velocity	1.02 ± 0.17 rad/s	~1.4 rad/s

A.3 Conclusion

The dynamic model has substantial benefits in predictive design, allowing many collisions to be simulated and the sensitivity to many parameters understood. However, the model still has limits. For example, for mode B in the prototype system, the simulated and experimental results with respect to the tangential velocity amplitude of the rotor do not match well, either in the frequency domain behavior or to a lesser extent its average velocity. The reasons for this difference highlight two limitations of the model: First, larger motion may lead to imbalanced rotor motion and the collisions with the hub, which are not included in the model; second, friction effects in particular are difficult to predict and model, either between the teeth and the rotor or, in this latter case, between the hub and rotor.

Future work of modeling may include tracking each of four teeth separately while the tooth motion amplitude differences are applied to each tooth individually. This modification could allow the model to include the tilting of the rotor, which while smaller than the effects studied in the current paper, can be caused by the difference of motion of each tooth and needs to be determined by further analytical modeling.

APPENDIX B

Run Sheet of Second-Generation Motor Fabrication Process

A general description of the fabrication process of second-generation motor is given in Chapter 3. A detailed description of each step defined in Table B-1 is provided in this appendix.

Table B-1: The Definition and numbering of each fabrication step

Pre-fabrication clean
00.10 Piranha Clean
DRIE 10 μm depth for electrodes gap (Mask 1)
10.10 Photolithography
10.20 DRIE 10 μm
10.30 Plasma stripping
Wet etch SiO^2 (Mask 2)
20.00 Pre-furnace clean
20.10 LPCVD 0.1 μm nitride and 1 μm HTO
20.20 Photolithography
20.30 BHF wet etch SiO_2
20.40 Remove PR
Metallization (Mask 3)
30.10 Evaporate 1000Å Cr and 5000Å Au
30.20 Photolithography
30.30 Cr/Au wet etch
30.40 Remove PR
DRIEs (Mask 4)
40.10 Photolithography
40.20 RIE Si_3N_4
40.30 DIRE 150 μm
40.40 BHF wet etch SiO_2
40.50 RIE Si_3N_4
40.60 Etch through wafer
40.70 XeF_2 etch to remove silicon sidewalls
Metallization on backside of the device for Au-In bonding
50.00 Pre-evaporation Descum treatment for Metglas
50.10 Evaporate 1000Å Cr and 5000Å Au
50.20 Electroplate ≈8 μm Indium on backside of silicon
Bonding and deposit isolation layer on the rotor electrodes
60.10 Indium rich Au-In bond
60.20 ALD deposit Al_2O_3 on rotor electrodes

The run sheet for this process further provides the detailed the parameters, tools, and methods as follows:

Pre-fabrication clean

00.10 Prepare starting wafers

- Piranha Clean [H2O2:H2SO4=1:1];
- Tool: Acid Bench 12
- 5 minutes in Piranha solution and followed by at least 10 minutes DI wafer

1st DIRE for defining electrodes gap

10.10 Lithography

- Spin-coat photoresist
  - Photoresist: SPR220-3.0
  - Tool: ACS 200
  - Recipe: SPR_3μm (HDMS vapor coating, soft bake 115˚C 90 sec)
- Expose
  - Tool: (MA/BA6)
  - Mask: M1, Clear field
  - Expose time/type: (10 sec/hard)
- Develop
  - Tool: ACS 200
  - Recipe: Bake&Dev_300DEV_30sec
  - Post bake 115˚C 90 sec, develop 30 s using AZ 300 MIF

10.20 Etch 10 μm silicon

- Tool: STS PEGASUS 4
- Recipe: (LNF Pegasus recipe 1)
- Etch rate (Expected: 4.02 μm /min; Measured: ≈4 μm /min)
- Results: Etch time and depth – 2 minute 30 sec and ≈10 μm

10.30 Strip photoresist

- Stripper/Time: Plasma Etcher/ 6 min
- Tool: Yes Plasma Stripper
- Results PR is removed (confirmed by optical images under microscope)
- Results: PR is removed

LPCVD nitride and HTO

20.00 Pre-furnace clean

- Tool: PFC-01 Wet Bench
- Recipe: RCA cleaning
  - Organic clean. H2O:H2O2:NH4OH =1:1:5 (10 min)
  - Oxide strip. 10:1 HF (30 s)
  - Ionic clean. H2O:H2O2:HCL = 1:1:6 (10 min)

- Q-Rinse

20.10 LPCVD Si_3N_4 layer and HTO

- Tool: S2/T3
- Recipe: Nitride/HTO
  - Time: 20 min / 3 hour 14 min
- Measure silicon nitride layer thickness (Å) using NanoSpec 6100
- Inspection:
- Comments:

20.20 Lithography

- Spin-coat photoresist
  - Tool: ACS 200
  - Mask 2, Clear Field
  - Recipe: SPR_3μm (thickness ≈3 μm)
  - Photoresist: (SPR220-3.0)
  - Relevant parameters: HDMS vapor coating, soft bake 115˚C 90 sec
- Expose
  - Tool: (MA/BA6)
  - Mask: M2
  - Expose time/type: (12 sec / hard)
- Develop:
  - Tool: ACS 200
  - Recipe: Bake&Dev_300DEV_40sec
  - Post bake 115˚C 90sec, develop 300 MIF 40 s
  - Another Post bake 115˚C 90sec

20.30 Etch SiO_2

Notes: Opening is necessary for etching out silicon cavity.

- HF wet etching
- Recipe: BHF (1:5 DI water)
- Expected etch rate: (≈1300 Å/min)
- Etch time: 8 Min 30 sec
- Comments: the etch rate is quite consistent with that measured by LNF staff.

20.40 Remove PR

- Tool: Solvent bench 12
- Recipe: PRS 200 85 ˚C
- Strip time: 10 Min
- DI rinse
- Comments: Clean

Metallization

30.10 Evaporate 1000Å Cr and 5000Å Au

- Tool: Enerjet Evaporator
- Comments: 4 PWs and 2 DWs were coated

30.20 Lithography

- Spin-coat photoresist
  - Tool: ACS 200
  - Mask 3, Dark Field
  - Recipe: SPR_3μm (thickness ≈3 μm)
  - Photoresist: (SPR220-3.0)
  - Relevant parameters: HDMS vapor coating, soft bake 115˚C 90 sec
- Expose
  - Tool: (MA/BA6) Mask: M2
  - Expose time/type: (12 sec / hard)
- Develop:
  - Tool: ACS 200
  - Recipe: Bake&Dev_300DEV_40sec
  - Post bake 115˚C 90sec, develop 300 MIF 40 s
  - Another Post bake 115˚C 90sec
- Rinse: (DI water, 3min)
- Spin dry:
- Inspection:
- Comments:

30.30 Wet etch Cr/Au

- Tool: Acid Bench 12
- Etchant: Gold etchant TFAC (No dilution); Cr etchant 1020
- Etch Rate: 1900 Å/min for Au and 770 Å/min for Cr
- Etch time: 2 min 30 sec for Au and 1 min 30 sec for Cr
- DI rinse
- Comment: With accurate time control, and dehydration of the PR, ≈ 17 μm wide gold wires was achieved (design is 20 μm).

30.40 Remove PR

- Tool: Solvent bench 12
- Recipe: PRS 200 85 ˚C
- Strip time: 10 Min
- DI rinse
- Comments: Clean

DRIEs

40.10 Lithography

- Spin-coat photoresist
  - Tool: ACS 200
  - Mask 4, Dark Field

    - Recipe: Run twice SPR220-3.0 5 µm
    - Photoresist: (SPR220-3.0)
    - Relevant parameters: HDMS vapor coating, soft bake 115˚C 90 sec
- Expose
    - Tool: (MA/BA6) Mask: M2
    - Expose time/type: (33 sec / hard)
- Develop:
    - Tool: ACS 200
    - Recipe: Bake&Dev_300DEV_40sec
- Rinse: (DI water, 3min)
- Spin dry
- Inspection:
- Comments: Do not do post exposure bake, which will induce bubbles in PR layer

40.20 RIE silicon nitride

- Tool: STS PEGASUS 4
- Recipe: (LNF Oxynitride)
- Etch rate: ≈ 1000 Å/min; Etch time: 1 min 20 sec
- Results: Observed silicon surface

40.30 DRIE 150 µm

- Tool: STS PEGASUS 4
- Recipe: (LNF Pegasus 3)
- Etch rate: ≈ 17 µm/min (measured by Jun);
- Etch time: 10 min
- Results: Etch rate is slightly different for different depth etch. The measured etching depth is 175 µm.

40.40 BHF SiO_2

- Tool: Acid bench 12
- Recipe: BHF
- Etch rate: ≈ 1300 Å/min (measured by Jun)
- DI rinse

40.50 RIE silicon nitride

- Tool: STS PEGASUS 4
- Recipe: (LNF Oxynitride)
- Etch rate: ≈ 1000 Å/min; Etch time: 1 min 20 sec
- Results: Observed silicon surface

40.60 DRIE etch through

- Tool: STS PEGASUS 4
- Recipe: (LNF Pegasus 1)
- Etch rate: ≈ 6.6 µm/min (measured by Jun);
- Etch time: 53 min

- Results: Etch rate is different for different region of the device. The trenches between springs have relatively slow etch rate. Thus, the actual thickness of stator is thinner than the 150 μm. Residual sidewalls are observed.

40.70 XeF2 etch to remove silicon sidewall

- Tool: Xactix XeF2
- Recipe: 10 sec etch time per cycle, 3.0 Torr XeF2
- Etch time: 30 cycles

Metallization on backside of the device for Au-In bonding

50.00 Pre-evaporation Descum treatment for Metglas

- Tool: Yes Plasma
- Recipe: Descum
- Etch time: 20 second

50.10 Evaporate 1000Å Cr and 5000Å Au

- Tool: Enerjet Evaporator
- Deposit rate: 10 Å/sec for both Au and Cr

50.20 Electroplate ≈8 μm Indium on backside of silicon

- Tool: Acid Bench in wet-chemistry room
- Electroplating current and time: 0.75 A for 10 min
- Measured thickness: ≈8 μm

Bonding and deposit isolation layer on the rotor electrodes

60.10 Indium rich Au-In bond

- Tool: Vacuum oven
- Temperature and time: 30 min heat up to 200 ˚C and maintain 200 ˚C for 2 hours and cool down

60.20 ALD deposit Al_2O_3 on rotor electrodes

- Tool: Oxford ALD
- Cycles: 20 cycles

APPENDIX C

Study on Different Designs of Miniaturized Magnetoelastic Resonators

C.1 Disc and Ring Resonator Design, Fabrication and Evaluation

C.1.1 Modeling

Utilizing a magnetomechanically-coupled finite element analysis (FEA) method implemented in COMSOL Multiphysics [Gre09], the resonant frequencies and deformations of candidate geometries were estimated (Fig. C-1). Both disc and ring geometries were studied; these shapes provide the desired symmetry while also allowing control over resonant frequency through simple changes in diameter. Pertinent calculated resonant frequency results are listed in Table C-1.

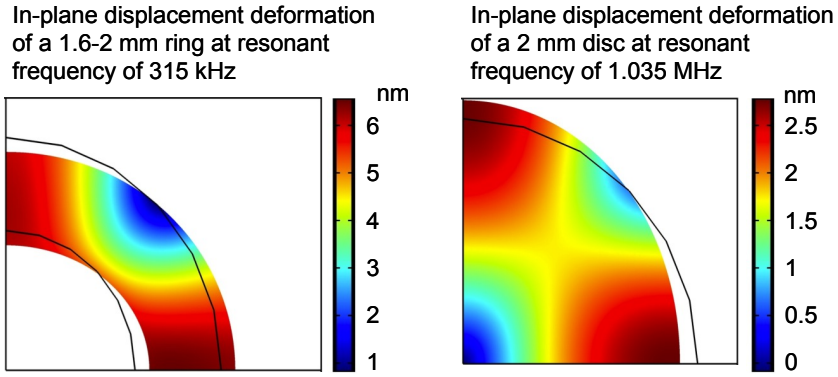

Figure C-1: FEA calculated deformations of candidate geometries at the fundamental resonant frequency of each geometry.

Table C-1: FEA calculated resonant frequencies of candidate geometries

Resonators	Ø 4-8 mm ring	Ø 2-4 mm ring	Ø 1.6-2 mm ring	Ø4 mm disc	Ø2 mm disc
Resonant Frequency	101 kHz	201 kHz	315 kHz	517 kHz	1.035 MHz

To evaluate the effect of geometrical variations on the resonant frequency of the device, a number of geometries were simulated with FEA, and the results were fit with simple curves (Fig. C-2). In general, the resonant frequency of disc shapes were shown to be less sensitive to diameter than the resonant frequency of ring shapes as the diameter is decreased. Additionally, the resonant frequency of ring shapes is sensitive to both inner and outer diameters; this shape thus may be less robust to process variations.

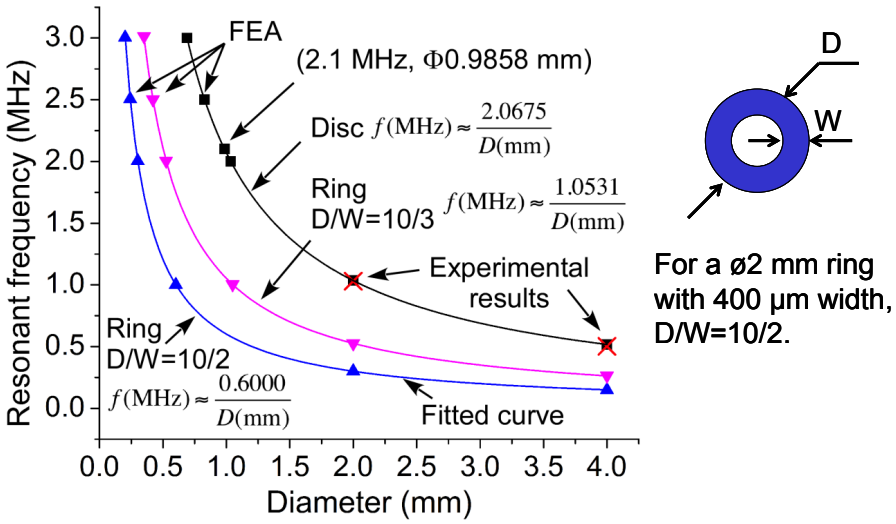

Figure C-2: FEA study of resonant frequency dependency on geometry. The experimental results shown are evaluated using the method described in the Evaluation section.

C.1.2 Fabrication

Initial prototype disc and ring resonators were fabricated using micro-electro-discharge machining (µEDM). Although this process can achieve micron precision, it is not likely appropriate for very high volume requirements. In this case, only a few prototypes were required for our initial studies, and serial fabrication of the prototypes was used. Figures C-3 and C-4 show optical and SEM images of the fabricated resonators, respectively. In all magnetoelastic elements in this report, as-cast MetglasTM 2826MB was used as the material.

Fig. C-3: Optical images of EDM'd resonators.

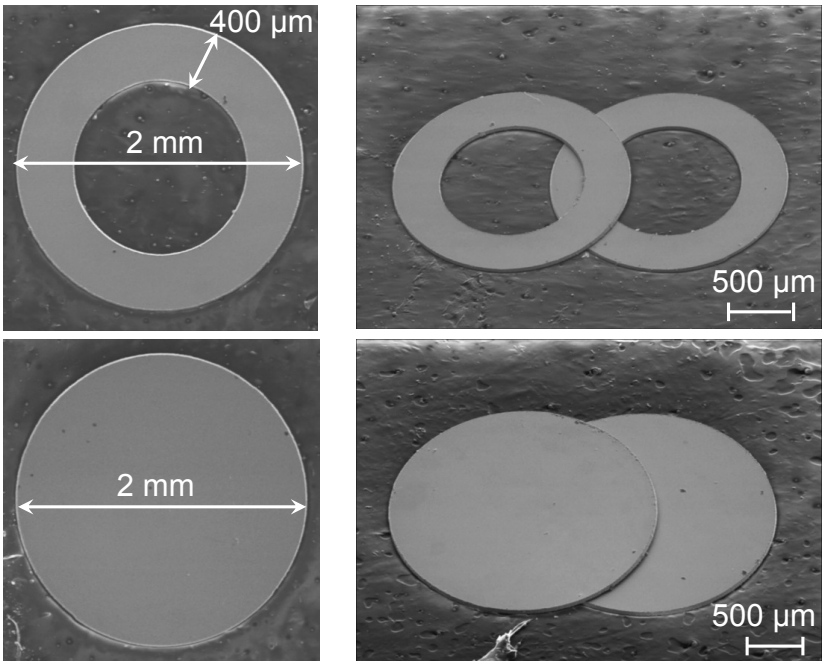

Fig. C-4: SEM images of EDM'd discs and rings.

A fabrication process appropriate for low-to-medium volumes was also utilized for disc and ring resonators – photochemical machining (PCM). The larger volume capability of this process (10-100 devices in a batch) enabled evaluation of gains in signal strength due to superposition of clustered or arrayed resonators. This process was carried out in this case by an out-of-house commercial vendor (Kemac Technologies, Inc., Azusa, CA). A one-sided etch was used. The etch process was also "tabless"; in other words, no connection between the unetched metal and the resonators remained once the etch was complete, and the resonators were free to drop out of the unetched metal. This

is in contrast to a typical "tabbed" etch. The "tabless" process provides the advantages of no required post-processing (to fully remove the resonators from the substrate metal) and the variability that small leftover tabs may add to the resonant frequencies of the resonators. However, the "tabless" process can result in more geometrical variation, as some resonators may remain in the etching process longer than others that drop out. The fabrication of "tabless" devices was a new extension of the standard Kemac process, so this attempt was also an experiment to evaluate the feasibility of a "tabless" MetglasTM etching process in a commercial foundry. The effect of process variation in this case is demonstrated in the subsequent "Evaluation" section. Figures C-5-7 show optical and SEM images of four different designs of the photochemically machined resonators.

Design A
Ø2 mm discs

Design B
Ø0.985 mm discs

Design C
Ø0.4-1 mm rings

Design D
Ø0.2-0.5 mm rings

Fig.C-5: PCM fabricated resonator designs.

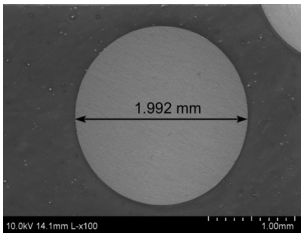

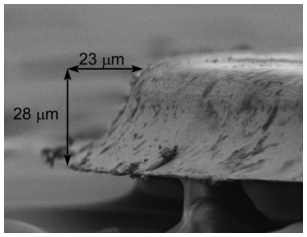

SEM image of backside of Design A: ø2mm disc

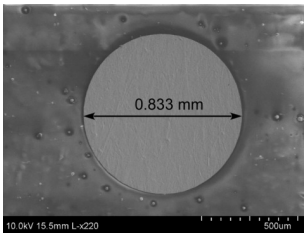

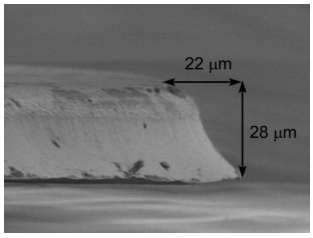

SEM image of backside of Design B: ø0.985 mm disc

Fig. C-6: SEM images of PCM fabricated discs

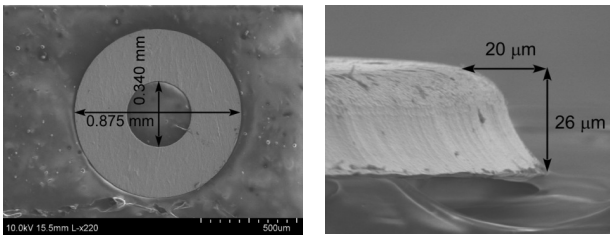

SEM image of backside of Design C: ø0.4-1 mm ring

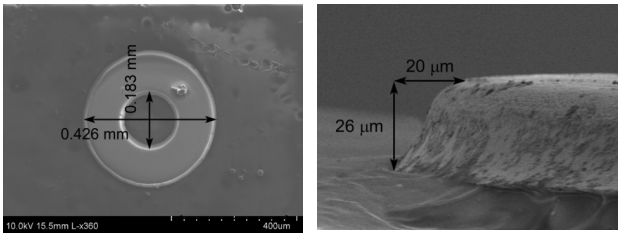

SEM image of front side of Design D: ø0.2-0.5 mm ring

Fig. C-7: SEM images of PCM fabricated rings

The SEM images in Figs. C-6 and 7 illustrate a noticeable sidewall angle created by the one-sided isotropic etching process. This angle is shallow but consistent; thus, its impact can be compensated by appropriate modeling and design.

C.1.3 Evaluation

C.1.3.1 Interrogation Setup

There are four main components of the interrogation setup for benchtop testing in air: a network analyzer, an amplifier, a transmit coil, and a receive coil. The coils are configured orthogonally such that the transmit coil and receive coil can both couple strongly to the resonators, but weakly with each other (Fig. C-7). The symmetry of the resonators and the excited mode shape allows for the transmitted oscillating magnetic field signal to be delivered in one direction while a response oscillating magnetic field is developed in a direction oriented orthogonally to the transmit direction. By also configuring the transmit and receive coils orthogonally to each other, the arrangement

helps to decouple the transmit signal from the received signal, improving the signal-to-noise ratio.

The network analyzer sweeps the frequency of the input signal, which is sent to the amplifier and to the transmit coil. The transmit coil generates an oscillating magnetic field, which causes the resonator to vibrate and generate a magnetic field in response. This response magnetic field induces a voltage on the receive coil, which is measured by the network analyzer. A frequency response for the resonator is thus generated, with the resonant response of the sensor indicating its presence in the interrogated region.

For this work, the coils have been turned using 60-stranded 22 AWG Litz wire, in which each individual conducting strand is insulated. For oscillating currents at the higher frequencies used in this work, the skin effect in a conductor is important in determining the overall impedance of the conductor. The individually-insulated conductors in the Litz wire are meant to reduce the skin effect and provide a higher conductance for high frequency signals. The higher conductance results in lower noise in the voltages induced on the receive coil, serving to increase the wireless range of the system. Similarly, the number of turns in the transmit and receive coils have been kept few (10) in order to lower the coil impedance and increase the magnitude of the transmitted magnetic field at the frequencies of interest. The transmit and receive coils have a diameter of ~3.8 cm.

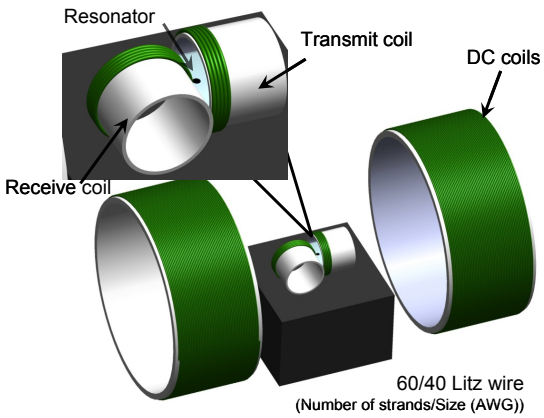

Fig. C-8: Schematic of preliminary evaluation setup for benchtop testing in air. The DC coils are used to provide a magnetic bias to the resonator when no permanent magnet is packaged with the resonator.

C.1.3.2 µEDM'd Prototypes and Signal Superposition

The µEDM'd prototypes described in the fabrication section were first evaluated. Individual discs and rings were measured while in air. Subsequently, these same discs were placed in arrays of larger number to evaluate the possibility of signal superposition for closely spaced resonators. As shown in Figs. C-9 and 10, results with these prototypes indicate that signal superposition can occur. Note that the responses of the individual discs are similar but not identical. This indicates that some process variability can be tolerated while still gaining the advantage of signal superposition.

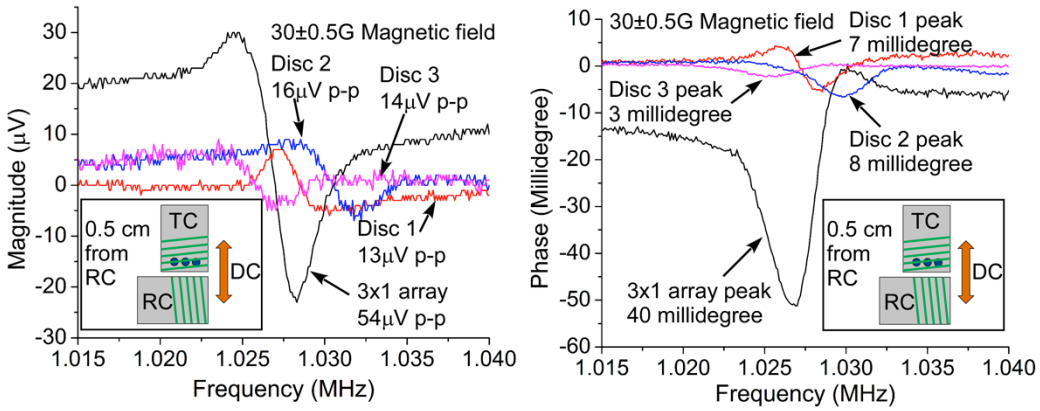

Fig. C-9: Magnitude (left) and phase (right) response of individual discs (colored curves) fabricated by µEDM, and the same discs in an array (black curves), illustrating the signal superposition that occurs.

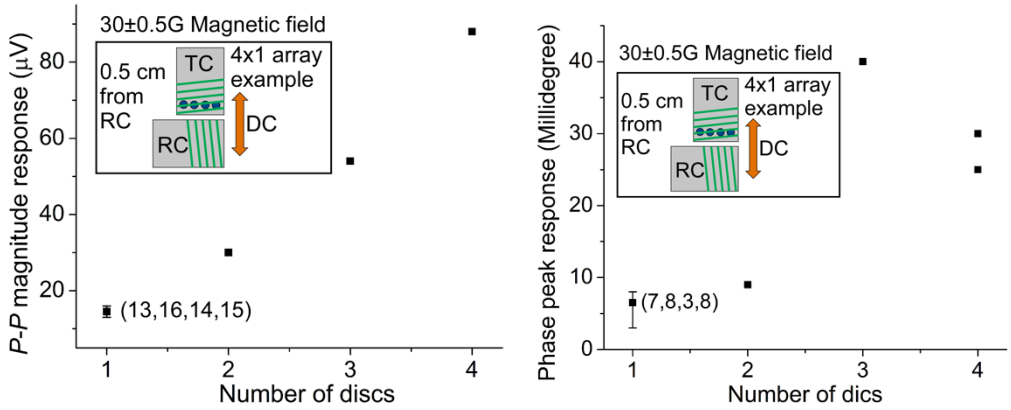

Fig. C-10: Magnitude (left) and phase (right) swings in the measured response of clustered resonators fabricated by μEDM exhibit properties of superposition of the individual responses.

C.1.3.3 Effect of Process Variability in PCM'd Resonators

A number of resonators fabricated in the "tabless" PCM process were measured to evaluate the variability in resonant frequency that may occur from such a process. Typical results with 2 mm discs (in air) are shown in Fig. C-11. Across 19 devices, there is a 0.7% standard deviation in resonant frequency. Based on the superposition analysis done with the μEDM'd resonators, we expect this small process variability to still result in signal superposition as the resonators are clustered.

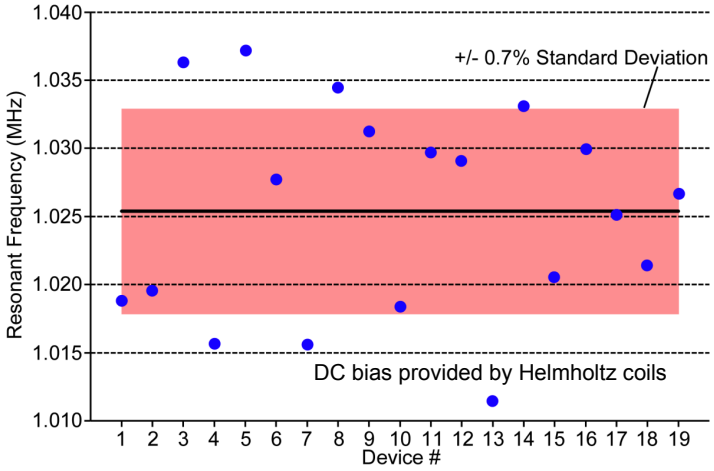

Fig. C-11: Measured resonant frequency response of individual PCM'd 2 mm discs (in air). The DC bias in this case is provided by the Helmholtz coils.

The effect of a preliminary resonator encapsulation method – including a flexible magnet layer for biasing the resonator – on the resonant frequency variability was also investigated. This encapsulation method is very preliminary and will thus not be covered in detail here; it is intended only to allow the resonators to be immersed in sand while biased with an integrated magnet. Devices with similar resonant frequencies as measured in Fig. C-12 were encapsulated and measured again. As shown in Fig. C-13, this process results in a very consistent resonant frequency distribution, with a standard deviation of 0.5% across 9 encapsulated resonators.

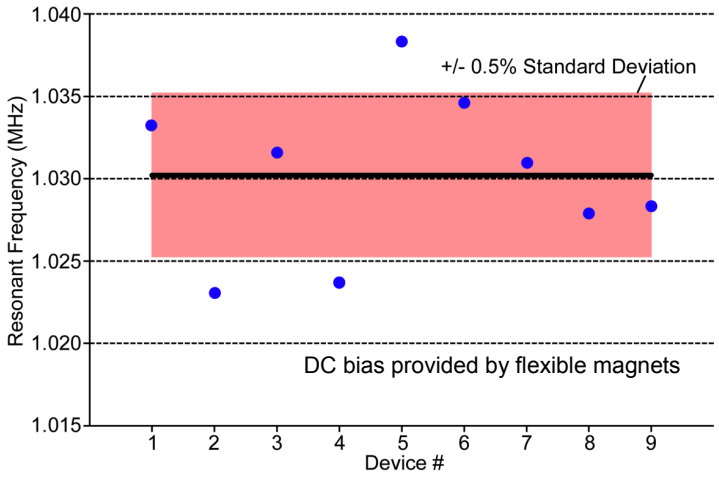

Fig. C-12: Resonant frequency response of PCM'd 2 mm discs after encapsulation (in air). The DC bias in this case is provided by a flexible magnet that is encapsulated with the resonator.

C.1.3.4 Signal Transmission in Sand

The six most closely matched devices encapsulated and measured in Figure 14 were arranged in a 3 x 2 array for measurement. The transmit and receive coils were spaced apart by 4 cm in this case (Fig. C-13) to investigate the feasibility of a small increase in wireless range. As shown in Fig. C-13, the resulting resonant signal of the clustered, encapsulated resonators (in air) is clear and distinct.

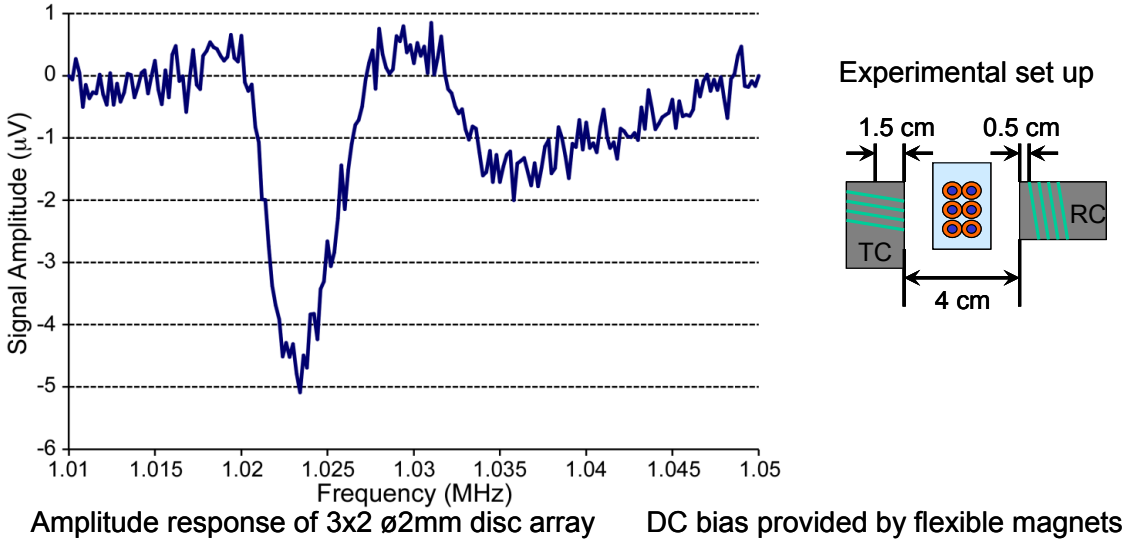

Fig. C-13: Measured signal amplitude of a 3 x 2 cluster of encapsulated resonators in air.

The array and coils were then buried in dry, room temperature sand as illustrated in Fig. C-14. A comparison between the frequency responses as shown in Fig. C-13 (air) and Fig. C-14 (sand) reveals negligible changes in signal strength or resonant frequency. This indicates that the response of the encapsulated particles is not affected by the presence of the dry sand.

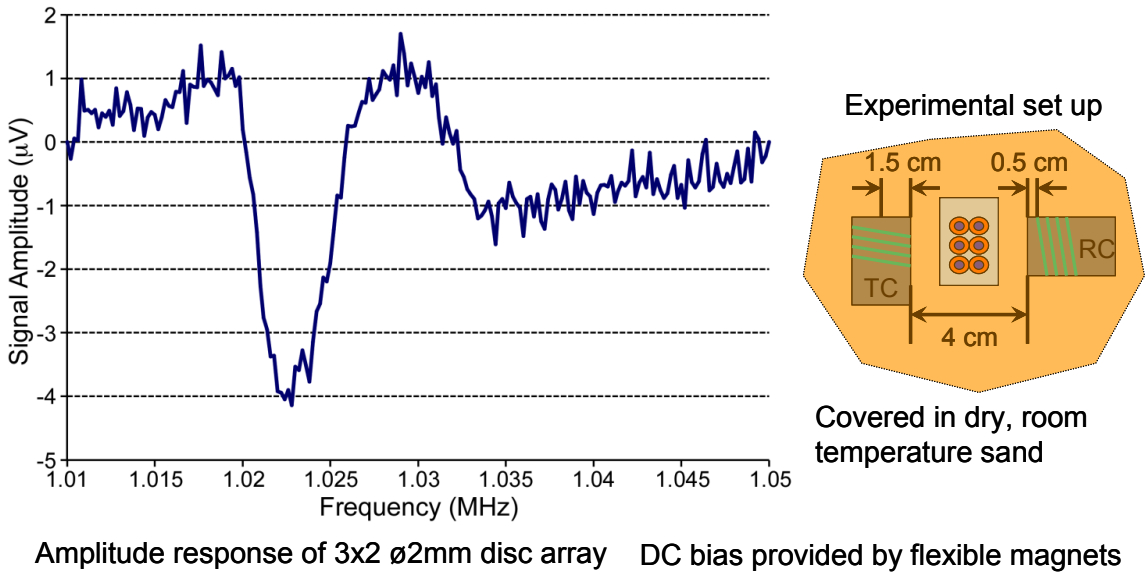

Fig. C-14: Measured signal amplitude of a 3 x 2 cluster of encapsulated resonators in dry sand

C.2 Disc Resonator Packaging, Increasing Sensing Range and Refining Structure

C.2.1 Package

C.2.1.1 Magnetic Field Bias Effect Characterization and Permanent Magnet Preparation

In order to resonate with optimum signal, the resonators must be biased with a DC magnetic field. Due to the ranges at which this technology is expected to operate, packaging a small permanent magnet with the resonators is preferable to supplying a large field from the borehole or other external source. The DC field required is a function of resonator size and geometry. The relationship between magnetic bias and measured signal amplitude has been characterized on ø1 mm disc resonators by utilizing two orthogonally placed small coils, one as a transmitter and another a receiver, and a set of DC coils as a source of magnetic field bias (Fig. C-15).

The results, as shown in Fig. C-15, suggest appropriate magnetic field biases for ø1 mm should be around 30-40 G. A number of possible permanent magnetic materials may be suitable for this type of application. One such material is NdFeB (magnets made from this material are commonly referred to as “neodymium” magnets). Magnets of this material can provide a very strong field for a given volume, but in general the material is relatively expensive. Another option is a chromium-iron permanent magnet alloy named Arnokrome™ 5, (Arnold Magnetic Technologies Corp., Rochester, NY). The Arnokrome™ 5 has magnetic remanence (Br) of 2000 – 16000 G, coercivity (Hc) of 20 - 50 Oe. Further, the Arnokrome™ foil is cold rollable to 0.002” thick, which can facilitate miniaturization of the package as well as high volume stamping processes. For preliminary packages, Arnokrome™ foil was EDM’d into ø1 mm discs, the same size as

the disc resonators. As a final step before packaging, these disc permanent magnets were magnetized using a bench-top pulse magnetizer.

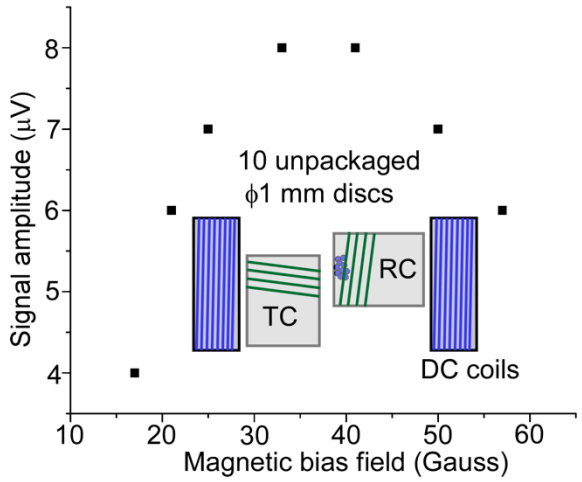

Fig. C-15: DC magnetic bias optimization for 1 mm diameter disc resonators.

C.2.1.2 Packaging Approach

A preliminary packaging approach consists of a ø1 mm disc resonator, a ø1 mm disc permanent magnet (fashioned from Arnokrome^{TM} 5 material, ≈50 μm thick), a ring-shaped polymer spacer, isolating $Mg_3Si_4O_{10}(OH)_2$ powder and two layers of adhesive tape, as shown in Fig. C-16 (a). First, a relatively thick transparent layer (≈200 μm thick) is punched with ø1.5 mm holes large enough for resonators. Second, the transparent layer is attached to one (bottom) layer of adhesive tape. The isolating powder is then used to cover the exposed area of adhesive tape, such that the resonator does not become adhered to the tape. This step is followed by placing both the permanent magnet and resonator inside the cavity. In some cases, intermediate spacing layers may be placed between the resonator and the magnet to adjust the DC bias level. Next, another thin layer of isolation powder is placed on the top of resonator and a second layer of adhesive tape is used to seal the cell. Finally, the whole unit is punched out from all layers,

forming a sealed cavity with resonator and magnet within. The packaged device has a total thickness of 600 µm and a diameter of 3 mm; an optical image is shown in Fig. C-16 (b). It is important to note that this preliminary packaging approach is intended to determine the amount of signal attenuation that may occur in a packaged resonator; it is not intended to withstand the expected pressures or temperatures of a down-hole application. Final packaging has been deferred to later stages of development based on guidance from Aramco.

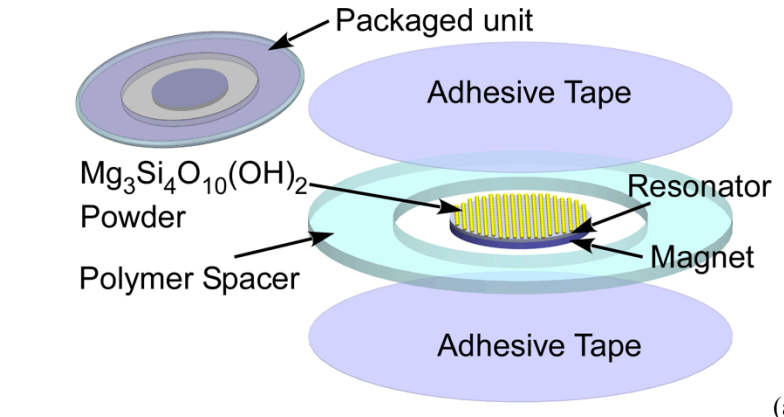

(a)

Packaged ø2 mm resonator Packaged ø1 mm resonator (b)

Fig. C-16: (a) Preliminary packaging approach. (b) Optical images of packaged resonators

C.2.1.3 Packaged Resonator Response

Measurement of the frequency response of the packaged "smart" pseudoparticle has been carried out using two small coils placed orthogonally to each other and closely

spaced. The orientation of the coils – one transmit coil (TC) and one receive coil (RC) – is shown in schematic form in Figure 23 below. For this work, the coils have been turned using 60-stranded 22 AWG Litz wire, in which each individual conducting strand is insulated. The number of turns in the transmit and receive coils have been kept few (10) in order to lower the coil impedance and increase the magnitude of the transmitted magnetic field at the frequencies of interest. The transmit and receive coils have a diameter of ≈3.9 cm. The network analyzer sweeps the frequency of the input signal, which is sent to the amplifier and the transmit coil. The transmit coil generates an oscillating ac magnetic field that drives the resonator into vibration. The vibration in the resonator, along with the magnetoelastic nature of the resonator material, generates a magnetic field in response. This response magnetic field induces a voltage on the receive coil, which is measured by the network analyzer. In this measurement, 25 dBm (≈0.3 W) was applied to the transmit coil. It is important to note that a large "common mode" signal exists between the transmit coil and receive coil, on top of which is the resonator signal. To better illustrate the resonator response in these figures, post-processing has been used to remove the common mode signal. The common mode signal usually exists as a linear function between magnitude and frequency. Thus, the post-processing consists of subtracting a linear estimate of the common mode signal (found from fitting multiple data points that are away from the resonant frequency of the resonator) from the overall signal. As shown in Figs. C-17 and 18, it is confirmed that the intended signals exist for the ø2 mm and ø1 mm packaged resonators.

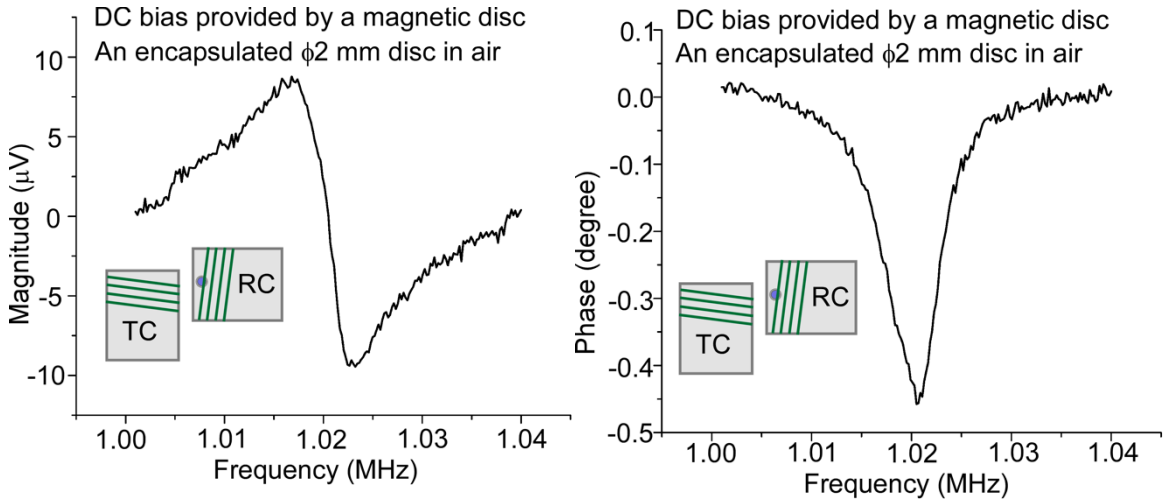

Fig. C-17: Typical frequency response of a ø2 mm disc resonator, encapsulated and biased with a neodymium magnet.

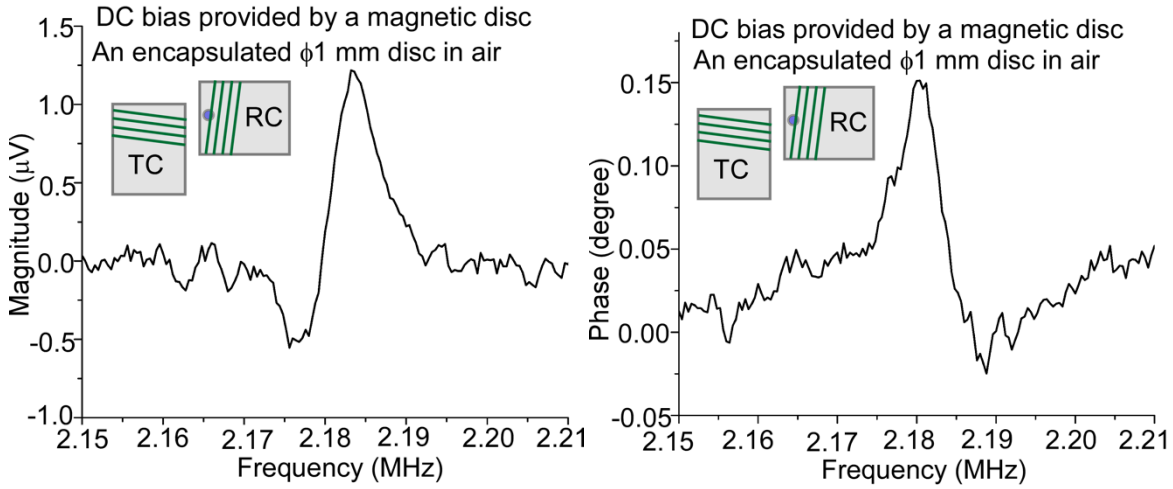

Fig. C-18: Typical frequency response of a ø1 mm disc resonator, encapsulated and biased with a Arnokrome™ 5 magnet.

C.2.2 Signal Superposition

Signal superposition is crucial for the fracture imaging system because it not only improves signal strength – and thus total imaging range – but also enables the ability to distinguish whether a given interrogated volume contains a large or small number of resonators. The concept of superposition has already been proven with four ø2 mm disc resonators. However, it is worthwhile to investigate whether superposition continues to be advantageous with a larger amount of ø1 mm disc resonators. By utilizing the same

experimental setup as that used for DC bias characterization measurement, the resonant response of ≈100 ø1 mm disc resonators was obtained with 1.4 mV amplitude, as shown in Fig. C-19. Compared to the signal amplitude of 2 μV for one ø1 mm disc resonator, the signal amplitude is magnified by 700 times. This not only shows superposition, but is a surprising result that suggests non-linear effects are occurring that provide further advantages than what would be expected from linear superposition. Further, this result shows that even a relatively large amount of resonators provides a single peak resonant response, regardless of the variation of the resonant frequency for each resonator.

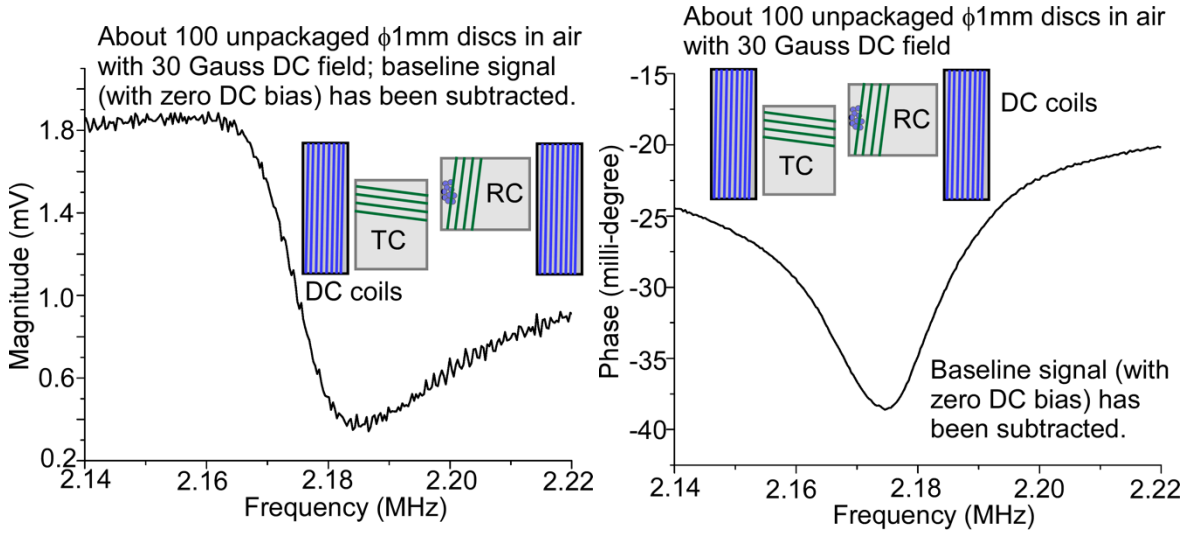

Fig. C-19: Signal superposition of ≈100 unpackaged 1 mm diameter disc resonators

C.2.3 Increasing Sensing Range

C.2.3.1 Interrogation Setup[4]

To increase sensing range, an interrogation setup was used that consists of a small transmit coil (≈3.9 cm diameter), a receive antenna of the form developed (referred to as the HMMF antenna), DC coils, a network analyzer and an amplifier. The network analyzer sweeps the frequency of the input signal, which is sent to the amplifier and to

[4] This work was done in collaboration with Prof. Kamal Sarabandi and Jihun Choi.

the transmit coil. The transmit coil generates an oscillating magnetic field, which causes the resonator to vibrate and generate a magnetic field in response. This response magnetic field induces a voltage on the receive antenna, which is measured directly by the network analyzer. DC coils are used to provide an appropriate magnetic bias as required by the magnetoelastic resonators. Further, because the resonators can be activated and deactivated by switching the DC coils "on" and "off", the transmitted signal was decoupled from the received signal by subtracting the frequency response of the "off" status from the frequency response of the "on" status, improving the signal-to-noise ratio. The resulting frequency response exhibits the resonant response of the resonators in the interrogated region. A total of ≈100 ø1 mm resonators were placed inside the transmit coil, in order to be driven by a strong magnetic field. Different sensing distances between resonators and the receive antenna (Range, R) were characterized. In this set of experiments, the receive antenna was the tuned, narrow band antenna described in section 7.2. It was developed for this effort to perform characterization of 2 MHz ø1 mm resonators during preliminary investigations. Two different orientations of the transmit coils with respect to the receive antenna, shown in Fig. C-20, have been investigated.

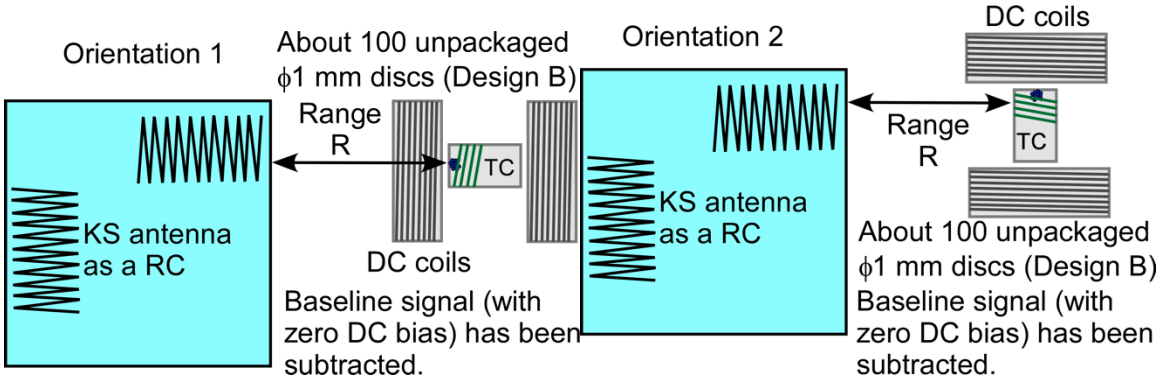

Fig. C-20: Schematic of antenna Orientations 1 and 2.

C.2.3.2 Experimental Results

The sensing distances (Range, R) for Orientation 1, as shown in Fig. C-20, were set at 25 cm, 40 cm, and 60 cm. The signal amplitudes for the distance of 25 cm, 40 cm, and 60 cm are 60 μV, 30 μV and 12 μV, respectively, demonstrating amplitude as inversely proportional to range. A typical response with the distance of 60 cm is shown in Fig. C-21. The noise level for this configuration is about 5 μV, which makes it challenging to detect a resonant response with distance beyond 60 cm with this configuration. For the results shown in Fig. C-21, the data has been pre- and post-processed to better illustrate the sensor signal. The pre-processing step involves measurement of the baseline signal, which is taken with the resonators in place but without a biasing field applied. This baseline signal is subtracted from the signal measured with a 30 G DC bias applied to the resonators. For both the baseline and measured signal, 16 traces are averaged together. The resulting measurement, which contains 401 sample points across the measured frequency band, is then post-processed via a 30 point moving average smoothing process.

The sensing distances for Orientation 2 were set at 20 cm, and 40 cm. The signal amplitude for the distance of 20 cm is about 15 μV. The resonant response for the distance of 40 cm is on the order of a few microvolts and has become comparable to the noise level at this range.

As shown in Fig. C-22, Orientation 1 exhibits a stronger received signal than Orientation 2 at all ranges. This may be due to slight anisotropy present in the near field of the receive antenna. In the far field, the antenna is expected to be isotropic. Further increase of the sensing range may require more transmitted power, a large quantity of the

resonators, or reduced noise on the receive antenna (which may be achievable with reduced signal feedthrough or improved antenna quality factor).

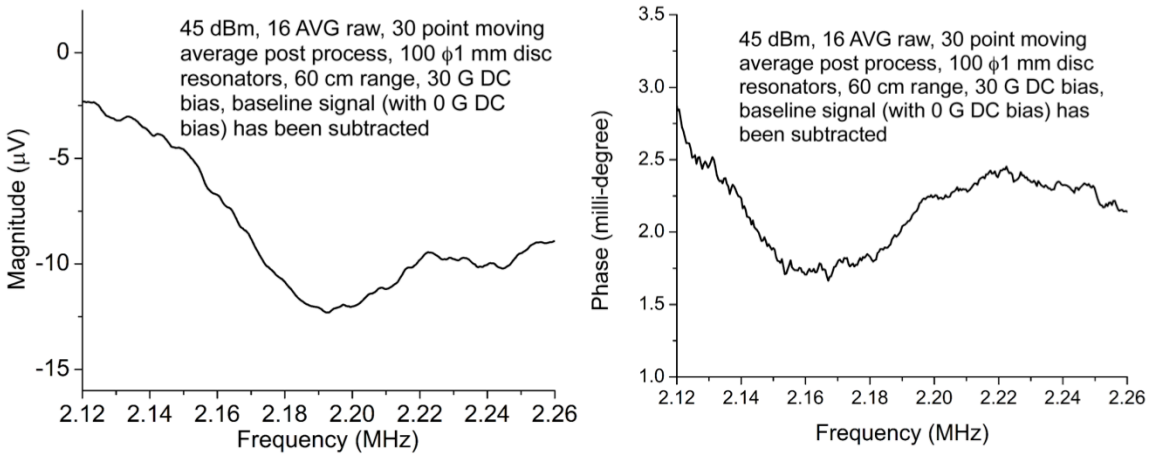

Fig. C-21: Resonant response of 100 unpackaged 1 mm diameter disc resonators, R=60 cm

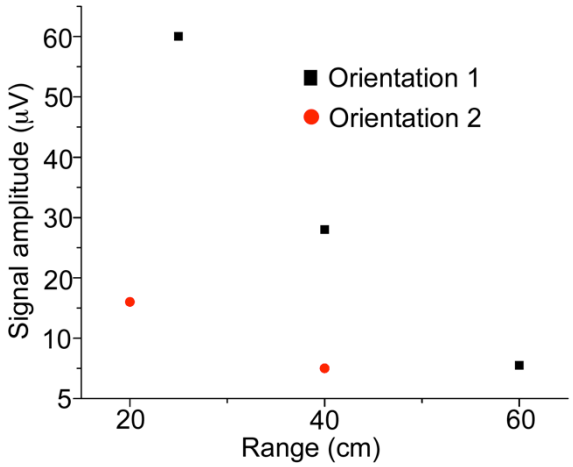

Fig. C-22: Comparison of orientations in air.

C.2.4 Detection of Resonators in Brine Tank

The salinity of the terrain between the interrogating antenna and the dispersed smart proppants may result in significant attenuation of the electromagnetic signals and reduce the usable range of the system (or alternatively increase the power requirements significantly). To evaluate the effect of salinity and to demonstrate that sensors can still be interrogated in the presence of salinity, a test setup was developed as shown in Fig. C-

23. In this setup, 40 unpackaged 2 mm diameter discs were positioned on a flexible magnetic strip (for DC biasing purposes) and placed inside the small transmit coil used and described previously. This transmit coil and its contents were placed inside a capped tube and connected to the amplifier driven by the network analyzer. The small receive coil was also placed inside a separate capped tube and connected to the network analyzer. These tubes were placed inside a tank, which was then filled with 3.5% (by weight) saline (seawater equivalent). The distance between the coils was varied, and the resultant response of the cluster of resonators measured at each distance (as well as with and without saline in the tank).

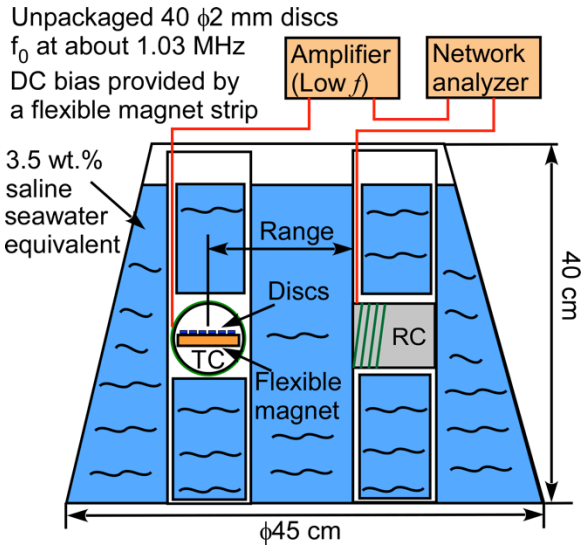

Fig. C-23: Brine tank test setup

Fig. C-24 shows a typical measured response from the cluster of resonators, at a range of 6 cm and with saline in the tank. Fig. C-25 summarizes the magnitude of the measured responses at various ranges and with air or saline in the tank. As can be seen, the presence of saline results in ≈40% reduction in signal strength compared to the signal received in air. The presence of saline also adds a small amount of noise to the measured

signal. Importantly, this test demonstrates that the presence of saline does not completely annihilate the transmitted signal in this frequency range.

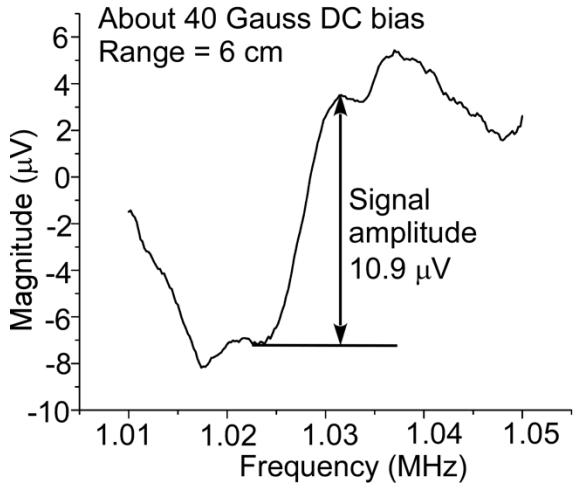

Fig. C-24: Typical measured response from resonator cluster.

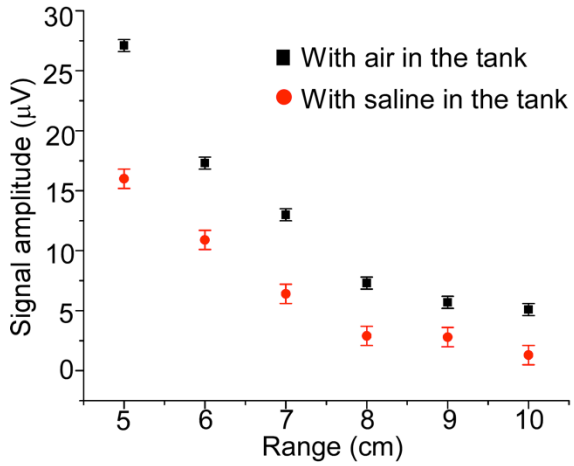

Fig. C-25: Comparison of measured responses at various ranges and with air or saline in the tank

C.3 3D Hexagonal Resonator Structure

C.3.1 Modeling

Utilizing the similar FEA simulation method, the simulated mode shapes, resonant frequencies, and maximum tip displacements of 3D "petal-shaped" hexagonal structures are given in Fig. C-26. The overall size of Design H is less than ø1.5 mm × 0.8

mm. There are two mode shapes that have resonant frequencies of 1.1 MHz and 1.3 MHz respectively.

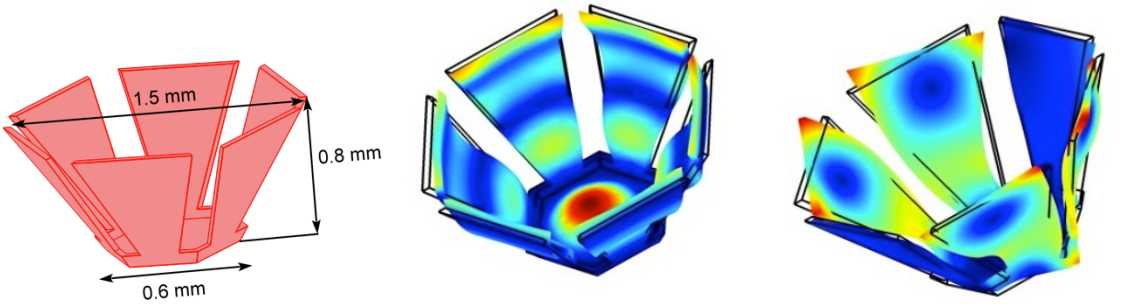

(a) Geometry (b) 1.1 MHz and 12 nm deformation (c) 1.3 MHz and 8 nm deformation

Fig. C-26: Geometry and FEA simulation results of Design H.

C.3.2 Fabrication

The fabrication process of 3D hexagonal structures was more complicated and is illustrated in Fig. C-27. The process started with 2D "starfish" structures fabricated using μEDM. An array of moulds was patterned on a brass substrate also using μEDM. Then, the 2D "starfish" structures were placed into the moulds, and pins were pushed through an aligning cover and towards the substrate, transforming 2D structures into 3D "petal-shaped" structures. The whole setup was clamped and put in a vacuum oven (~30 mTorr) for an annealing process at 275˚C for 12 hours. After the annealing process, the deformation of the structure became permanent.

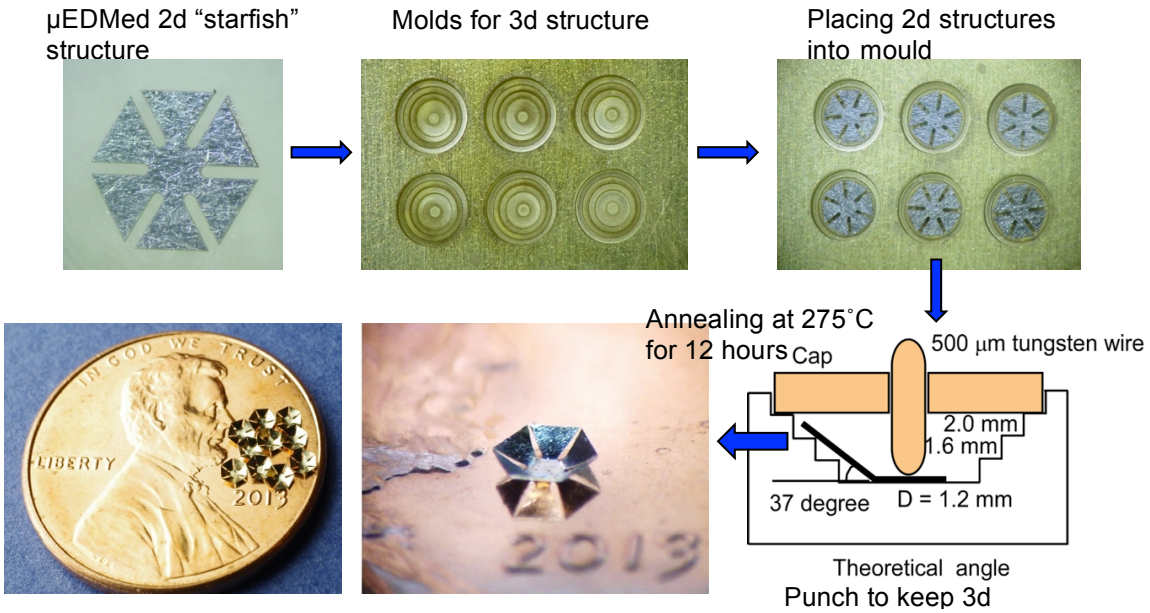

Fig. C-27: Fabrication process of 3D hexagonal structures.

C.3.3 Experimental Results

The resonant response of 3D hexagonal resonators was obtained using similar experimental setups described in Appendix 3.1.3.1. The signal amplitude of Design H (27 μV) is also larger than that of the disc resonator (described in Appendix C.1) because more magnetoelastic material is involved in the vibration. In addition, it has been experimentally confirmed that signal superposition also works for 3D hexagonal resonators. There are three resonant peaks obtained for 15 clustered 3D hexagonal resonators, and the signal amplitudes of each resonant peak is smaller than 15x the signal amplitude of single resonator. The multiple peaks and small signal amplitudes may be caused by the large variation in resonant frequencies for the 3D hexagonal structure induced during the fabrication process.

C.4 Asterisk Magnetoelastic Tag Simulations

Asterisk geometry is potential a good candidate for magnetoelastic tags because it allows reduce the signal strength sensitivity to the orientations of the interrogation field. The FEA simulations are used to investigate the resonant frequency, mode shapes and signal strength of the asterisk magnetoelastic tag. The geometry used in the simulation is shown in Fig. C-28. The dimension of each bar in the sensor is 0.25mm × 1.5mm. The angle between the central line and direction of the applied DC and AC magnetic field is defined as Θ. Two specific cases when the Θ is equal to 0 degree and 22.5 degree are investigated.

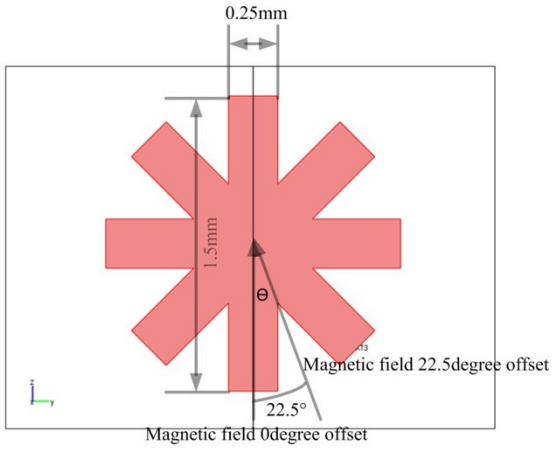

Fig. C-28: Geometrical parameters of the asterisk magnetoelastic tag. The angle between the applied AC and DC magnetic field and the center axis of the tag is defined as Θ.

The FEA simulations are carried out using customized magneto-mechanical coupled model in Comsol 3.4 [Gre09]. The magnitude and phase of the signal generated by the tag are calculated from the integration of the magnetic flux density within the pick up coil. The resonant frequency for the tag with different oriented applied magnetic field ranges from 1.48 MHz to 1.5 MHz. The resonant frequencies and the mode shapes of the asterisk tag with Θ of 0 degree and 22.5 degree are given in Fig. C-29.

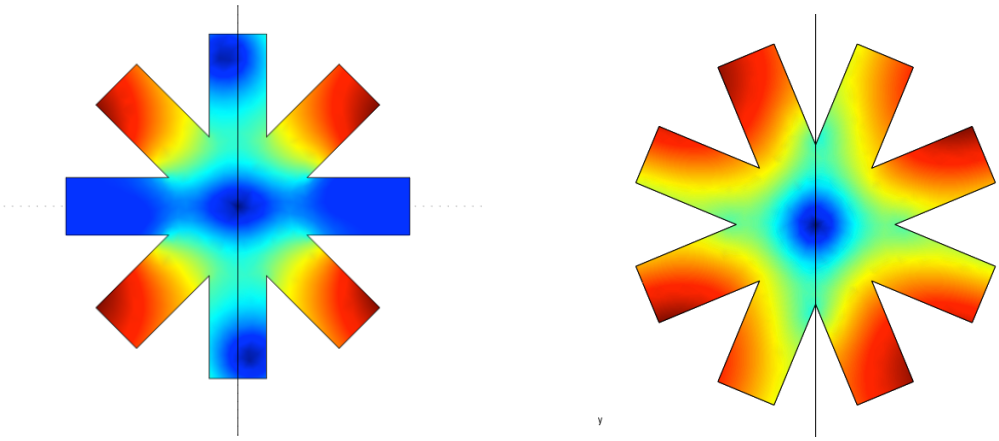

(a) (b)

Fig. C-29: (a) Θ = 0 degree model shape and resonant frequency of 1.4896MHz; (b) Θ = 22.5 degree mode shape and resonant frequency of 1.492MHz.

The frequency responses of the tag with Θ of 0 and 22.5 degree are given in Fig. C-30. The FEA simulation results show small variations of the peak-to-peak magnitude and frequency shift for two simulated conditions.

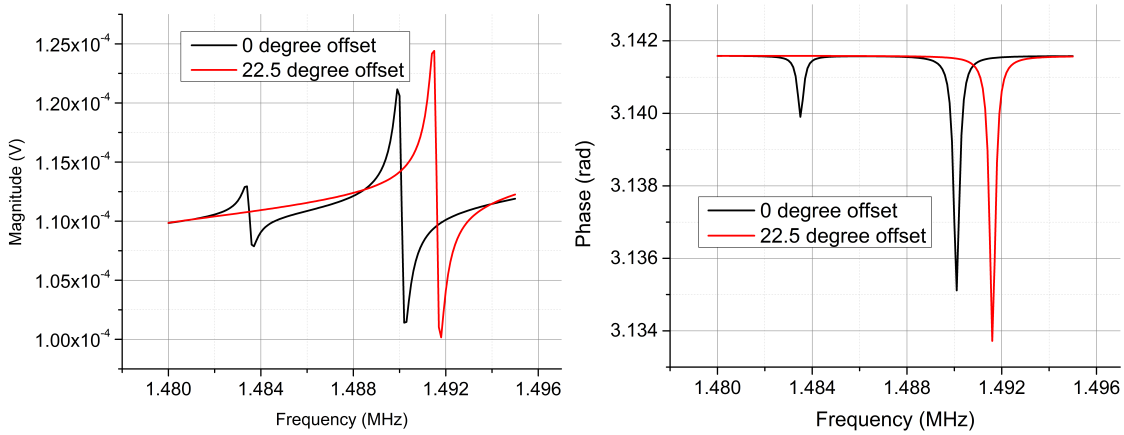

Fig. C-30: (Left) Magnitude and (Right) Phase frequency response of the voltage induced in the pick up coil.

REFERENCES

[Ach06] N. Achotte, P. A. Gilles, O. Cugat, J. Delamare, P. Gaud, and C. Dieppedale, "Planar brushless magnetic micromotors," *Journal of Microelectromechanical Systems,* vol. 15, pp. 1001-1014, Aug 2006.

[Ahn93] C. H. Ahn, Y. J. Kim, and M. G. Allen, "A Planar Variable Reluctance Magnetic Micromotor with Fully Integrated Stator and Wrapped Coils," *Micro Electro Mechanical Systems, Proceedings,* pp. 1-6, 1993.

[And85] P. M. Anderson, G. R. Bretts, J. E. Kearney, "Surveillance System Having Magnetomechanical Marker," U.S. Patent 4510489, Apr. 9, 1985.

[Arn06] D. P. Arnold, S. Das, F. Cros, I. Zana, M. G. Allen, and J. H. Lang, "Magnetic induction machines integrated into bulk-micromachined silicon," *Journal of Microelectromechanical Systems,* vol. 15, pp. 406-414, Apr 2006.

[ASM89] ASM Handbook, 16, ASM International, 1989.

[Bao07] Bao, M., & Yang, H. (2007). Squeeze film air damping in MEMS. Sensors and Actuators A: Physical, 136(1), 3-27.

[Bar89] S. F. Bart, J. H. Lang, "An analysis of electroquasistatic induction micromotors," *Sensors and Actuators,* vol. 20, p. 9, 1989.

[Bar92]Bart, S. F., Mehregany, M., Tavrow, L. S., Lang, J. H., & Senturia, S. D. (1992). Electric micromotor dynamics. Electron Devices, IEEE Transactions on, 39(3), 566-575.

[Bar73] H. V. Barth, *IBM Tech. Disclosure Bull.,* vol. 16, p. 2263, 1973.

[Bel05] A. S. Belyakov, "Magnetoelastic sensors and geophones for vector measurements in geoacoustics," *Acoustical Physics*, vol. 51, pp. S43-S53, 2005.

[Ben05] J. Benatar, "FEM Implementations of Magnetostrictive-Based Applications", MS thesis, Univ. of Maryland, 2005.

[Bhu96] Bhushan, B. (1996). "An Investigation of Micro Structures, Sensors, Actuators, Machines and Systems," *IEEE, The Ninth Annual International Workshop on Micro Electro Mechanical Systems, 1996, MEMS'96, Proceedings*.

[Bhu97] Bhushan, B., & Li, X. (1997). “Micromechanical and tribological characterization of doped single-crystal silicon and polysilicon films for microelectromechanical systems,” *Journal of Materials Research*, 12(1), 54-63.

[Bro79] M. Brouha, J. van der Borst, “The Effect of Annealing Conditions On the Magnetomechanical Properties of FeBSi Amorphous Ribbons,” *Journal of Applied Physics*, vol. 50, pp. 7595-7596, Nov 1979.

[Cal07] F. T. Calkins, A. B. Flatau, and M. J. Dapin, "Overview of magnetostrictive sensor technology," *Journal of Intelligent Material Systems and Structures*, vol. 18, pp. 1057-1066, Oct 2007.

[Cai00] Q. Y. Cai, A. Cammers-Goodwin, and C. A. Grimes, "A wireless, remote query magnetoelastic CO2 sensor," *Journal of Environmental Monitoring,* vol. 2, pp. 556-560, Dec 2000.

[Cai04] Q. Y. Cai, K. F. Zeng, C. M. Ruan, T. A. Desai, and C. A. Grimes, "A wireless, remote query glucose biosensor based on a pH-sensitive polymer," *Analytical Chemistry,* vol. 76, pp. 4038-4043, Jul 15 2004.

[Cha92] L. C. Chang, W. Deptford, “Coplanar Multiple Loop Antenna for Electronic Article Surveillance Systems,” U.S. Patent 5142292, Aug. 25, 1992.

[Cha12] M. L. Chan, B. Yoxall, H. Park, Z. Y. Kang, I. Izyumin, J. Chou, M. M. Megens, M. C. Wu, B. E. Boser, and D. A. Horsley, "Design and characterization of MEMS micromotor supported on low friction liquid bearing," *Sensors and Actuators a-Physical,* vol. 177, pp. 1-9, Apr 2012.

[Che89] H. Chen, D. E. Polk, “Novel Amorphous Metals and Amorphous Metal Articles,” U. S. Patent, 32925, May 16, 1989.

[Cho11] J. Cho, J. Gregory, and K. Najafi, "Single-crystal-silicon vibratory cylinderical rate integrating gyroscope (CING)," presented at the *Solid-State Sensors, Actuators and Microsystems Conference (TRANSDUCERS)*, 2011.

[Cla97] F. Claeyssen, N. Lhermet, R. LeLetty, and P. Bouchilloux, "Actuators, transducers and motors based on giant magnetostrictive materials," *Journal of Alloys and Compounds,* vol. 258, pp. 61-73, Aug 1 1997.

[Cro06] F. Cros, H. Koser, M. G. Allen, and J. H. Lang, "Magnetic induction micromachine-part II: fabrication and testing," *Microelectromechanical Systems, Journal of,* vol. 15, pp. 427-439, 2006.

[Cop94] R. L. Copeland, M. Kopp, and R. C. Ohandley, "Analysis of a Magnetoelastic Sensor," *IEEE Transactions on Magnetics*, vol. 30, pp. 3399-3402, Sep 1994.

[Der10] Demiri, Shpend, "Geometric Effects on the Wear of Microfabricated Silicon Journal Bearings" (2010). Thesis. Rochester Institute of Technology.

[Dub98] M. A. Dubois and P. Muralt, "PZT thin film actuated elastic fin micromotor," *Ieee Transactions on Ultrasonics Ferroelectrics and Frequency Control,* vol. 45, pp. 1169-1177, Sep 1998.

[Duf96] Dufour, I., Sarraute, E., & Abbas, A. (1996). "Optimization of the geometry of electrostatic micromotors using only analytical equations," *Journal of Micromechanics and Microengineering*, 6(1), 108.

[End13] Endemano, A., Fourniols, J., Camon, H., Marchese, A., Muratet, S., Bony, F., Overton, G. (2003). "VHDL–AMS modelling and simulation of a planar electrostatic micromotor," *Journal of Micromechanics and Microengineering*, 13(5), 580.

[Fab] C. E. Fabian, P. M. Anderson, G. E. Fish, "Miniature Magnetomechanical Marker for Electronic Article Surveillance System," U.S. Patent, 7075440 B2, Jul. 11, 2006.

[Fan89] L.S. Fan, Y.-C. Tai, Long-Shen Fan, Richard S. Muller, "IC-processed electrostatic micromotors," *Sensors and Actuators* vol. 20, pp. 41-47, 1989.

[Fra] Frangi, A., Corigliano, A., Binci, M., & Faure, P. (2005). Finite element modelling of a rotating piezoelectric ultrasonic motor. Ultrasonics, 43(9), 747-755.

[Gha08] N. Ghalichechian, A. Modafe, M. I. Beyaz, and R. Ghodssi, "Design, fabrication, and characterization of a rotary micromotor supported on microball bearings," *Journal of Microelectromechanical Systems,* vol. 17, pp. 632-642, Jun 2008.

[Gia14] Y.B. Gianchandani, J. Tang, S.R. Green, "Frame-suspended magnetoelastic resonators," US patent 61931300 (application submitted in 2014).

[Gia14] Y.B. Gianchandani, S.R. Green, K. Sarabandi, M. Kanj, H. Schmidt, J. Tang, J. Wu, "Interrogating Subterranean Hydraulic Fractures using Magnetoelastic Resonators," US patent 61931934 (application submitted in 2014).

[Gre09] S. R. Green and Y. B. Glanchandani, "Wireless Magnetoelastic Monitoring of Biliary Stents," *Journal of Microelectromechanical Systems*, vol. 18, pp. 64-78, Feb 2009.

[Gre10] S. R. Green and Y. B. Gianchandani, "Tailored magnetoelastic sensor geometry for advanced functionality in wireless biliary stent monitoring systems," *Journal of Micromechanics and Microengineering*, vol. 20, pp. 075040-075053, Jul 2010.

[Gre10] S. R. Green, R. S. Kwon, G. H. Elta, and Y. B. Gianchandani, "In situ and ex vivo evaluation of a wireless magnetoelastic biliary stent monitoring system," *Biomedical Microdevices,* vol. 12, pp. 477-484, Jun 2010.

[Gri96] Griffin, W., Richardson, H. H., & Yamanami, S. (1966). “A study of fluid squeeze-film damping,” *Journal of Basic Engineering*, 88, 451.

[Gri00] C. A. Grimes and D. Kouzoudis, "Remote query measurement of pressure, fluid-flow velocity, and humidity using magnetoelastic thick-film sensors," Sensors and Actuators a-Physical, vol. 84, pp. 205-212, Sep 1 2000.

[Gri11] C. A. Grimes, S. C. Roy, S. J. Rani, and Q. Y. Cai, "Theory, Instrumentation and Applications of Magnetoelastic Resonance Sensors: A Review," Sensors, vol. 11, pp. 2809-2844, Mar 2011.

[Guc91] H. Guckel, K.J. Christenson, J. Klein, B. Choi, E.G. Lovell and T. W. Chapman, “Fabrication and testing of the planar magnetic micromotor,” *Journal of Micromechanics and Microengineering*, vol. 1(3), pp. 135, 1991.

[Guc93] H.Guckel, T.R. Christenson, K.J. Sdrobis, T.S. Jung, J. Klein, K.V. Hartojo, and I. Widjaja, "A first functional current excited planar rotational magnetic micromotor," *Micro Electro Mechanical Systems, MEMS’93, Proceedings An Investigation of Micro Structures, Sensorsm Acutators, Machines and Systems, IEEE,* 1993, pp. 7-11.

[Hag95] Hagood IV, N. W., & McFarland, A. J. (1995). “Modeling of a piezoelectric rotary ultrasonic motor,” *IEEE, Transactions on Ultrasonics, Ferroelectrics and Frequency Control*, 42(2), 210-224.

[Han10] L. H. Han, S. M. Wu, J. C. Condit, N. J. Kemp, T. E. Milner, M. D. Feldman, and S. C. Chen, "Light-powered micromotor driven by geometry-assisted, asymmetric photon-heating and subsequent gas convection," *Applied Physics Letters,* vol. 96, May 24 2010.

[Hen12] Y. B. Gianchandani, E. Hendarto, "Marangoni-driven Micromotor in Liquid Medium," presented at the *Solid-State Sensors, Actuators and Microsystems Conference (TRANSDUCERS)*, 2011.

[Her00] G. Herzer, “Amorphous Magnetostrictive Alloy with Low Cobalt Content and Method for Annealing Same,” U.S. Patent, 6018296, Jan. 25, 2000.

[Her00] G. Herzer, “Method of Annealing Amorphous Ribbons and Marker for Electronic Article Surveillance,” U.S. Patent, 6011475, Jan. 4, 2000.

[Her02] G. Herzer, “Magneto-Acoutic Marker for Electronic Article Surveillance Having Reduced Size and High Signal Amplitude,” U.S. Patent, 6359563 B1, Mar. 19, 2002.

[Her03] G. Herzer, "Magnetic materials for electronic article surveillance," *Journal of Magnetism and Magnetic Materials*, vol. 254, pp. 598-602, Jan 2003.

[Iio00] A. Iino, K. Suzuki, M. Kasuga, M. Suzuki, and T. Yamanaka, "Development of a self-oscillating ultrasonic micro-motor and its application to a watch," *Ultrasonics,* vol. 38, pp. 54-59, Mar 2000.

[Jai00] M. K. Jain, S. Schmidt, K. G. Ong, C. Mungle, and C. A. Grimes, "Magnetoacoustic remote query temperature and humidity sensors," *Smart Materials & Structures,* vol. 9, pp. 502-510, Aug 2000.

[Jai01] M. K. Jain, S. Schmidt, and C. A. Grimes, "Magneto-acoustic sensors for measurement of liquid temperature, viscosity and density," *Applied Acoustics*, vol. 62, pp. 1001-1011, Aug 2001.

[Kaa07] V. Kaajakari and A. Lal, "Micromachined ultrasonic motor based on parametric polycrystalline silicon plate excitation," *Sensors and Actuators a-Physical,* vol. 137, pp. 120-128, Jun 12 2007.

[Kan06] T. Kanda, A. Makino, T. Ono, K. Suzumori, T. Morita, and M. K. Kurosawa, "A micro ultrasonic motor using a micro-machined cylindrical bulk PZT transducer," *Sensors and Actuators a-Physical,* vol. 127, pp. 131-138, Feb 28 2006.

[Kim96] C. K. Kim and R. C. Ohandley, "Development of a magnetoelastic resonant sensor using iron-rich, nonzero magnetostrictive amorphous alloys," *Metallurgical and Materials Transactions a-Physical Metallurgy and Materials Science*, vol. 27, pp. 3203-3213, Oct 1996.

[Koc02] B. Koc, S. Cagatay, and K. Uchino, "A piezoelectric motor using two orthogonal bending modes of a hollow cylinder," *IEEE Transactions on Ultrasonics Ferroelectrics and Frequency Control,* vol. 49, pp. 495-500, Apr 2002.

[Kos06] H. Koser and J. H. Lang, "Magnetic induction micromachine-part I: Design and analysis," *Microelectromechanical Systems, Journal of,* vol. 15, pp. 415-426, 2006.

[Kou00] D. Kouzoudis and C. A. Grimes, "The frequency response of magnetoelastic sensors to stress and atmospheric pressure," *Smart Materials & Structures,* vol. 9, pp. 885-889, Dec 2000.

[Lan86] Landau, L.D.; Lifshitz, E.M. Theory of Elasticity, 3rd ed.; Pergamon Press: New York, NY, USA,1986.

[Lee93] C.C. Lee, C.Y. Wang, and G. Matijasevic, "Au-in Bonding Below the Eutectic Temperature," *IEEE Transactions on Components Hybrids and Manufacturing Technology*, vol. 16, pp. 311-316, May 1993.

[Lee93] Lee, A. P. Pisano, A. P. (1993). Repetitive impact testing of micromechanical structures. *Sensors and Actuators A: Physical*, 39(1), 73-82.

[Lee07] H. S. Lee, C. Cho, and M. W. Cho, "Magnetostrictive micro mirrors for an optical switch matrix," *Sensors*, vol. 7, pp. 2174-2182, Oct 2007.

[Lin97] J.F. Lindberg, "The Application of High Density Transducer Materials to Smart Systems," MRS Proceeding, vol. 459, pp. 509-519, 1997.

[Liu10] W. Liu, X. H. Jia, F. J. Wang, and Z. Y. Jia, "An in-pipe wireless swimming microrobot driven by giant magnetostrictive thin film," *Sensors and Actuators a-Physical,* vol. 160, pp. 101-108, May 2010.

[Liv04] C. Livermore, A. R. Forte, T. Lyszczarz, S. D. Umans, A. A. Ayon, and J. H. Lang, "A high-power MEMS electric induction motor," *Journal of Microelectromechanical Systems,* vol. 13, pp. 465-471, Jun 2004.

[Maa00] Maas, J., Schulte, T., & Frohleke, N. (2000). Model-based control for ultrasonic motors. Mechatronics, IEEE/ASME Transactions on, 5(2), 165-180.

[Maa95] Maas, J., Ide, P., Frohleke, N., & Grotstollen, H. (1995). Simulation model for ultrasonic motors powered by resonant converters. Paper presented at the Industry Applications Conference, 1995. Thirtieth IAS Annual Meeting, IAS'95., Conference Record of the 1995 IEEE.

[Meh90] M. Mehregany, S. F. Bart, L. S. Tavrow, J. H. Lang, and S. D. Senturia, "Principles in Design and Microfabrication of Variable-Capacitance Side-Drive Motors," *Journal of Vacuum Science & Technology a-Vacuum Surfaces and Films,* vol. 8, pp. 3614-3624, Jul-Aug 1990.

[Men09] Meng, G., Zhang, W.-M., Huang, H., Li, H.-G., & Chen, D. (2009). "Micro-rotor dynamics for micro-electro-mechanical systems (MEMS)," *Chaos, Solitons & Fractals*, 40(2), 538-562.

[Mer11] S. Merzaghi, C. Koechli, and Y. Perriard, "Development of a Hybrid MEMS BLDC Micromotor," *IEEE Transactions on Industry Applications,* vol. 47, pp. 3-11, Jan-Feb 2011.

[Met08] Metglas, Inc. "Magnetic Alloy 2826MB (nickel-based) Technical Bulletin".

[Mon88] S. Montean, "RF Reactivatable Marker for Electronic Article Surveillance System," U.S. Patent 4745401, May 17, 1988.

[Mon90] S. Montean, Blaine, "Multi-directionally Responsive Dual-status, Magnetic Article Surveillance Marker Having Continuous Keeper," U.S. Patent 4967185, Oct. 30, 1990.

[Mor00] T. Morita, M. K. Kurosawa, and T. Higuchi, "A cylindrical shaped micro ultrasonic motor utilizing PZT thin film (1.4 mm in diameter and 5.0 mm long stator transducer)," *Sensors and Actuators a-Physical,* vol. 83, pp. 225-230, May 22 2000.

[Mor03] T. Morita, "Miniature piezoelectric motors," *Sensors and Actuators,* vol. 103, pp. 291-300, 2003.

[Nag05] S. E. Nagle, C. Livermore, L. G. Frechette, R. Ghodssi, and J. H. Lang, "An electric induction micromotor," *Journal of Microelectromechanical Systems,* vol. 14, pp. 1127-1143, Oct 2005.

[Par01] J. S. Park, L. L. Chu, A. D. Oliver, and Y. B. Gianchandani, "Bent-beam electrothermal actuators - Part II: Linear and rotary microengines," *Journal of Microelectromechanical Systems,* vol. 10, pp. 255-262, Jun 2001.

[Pio92] C. Piotrowski, C. L. Bruzzone, J. W. Mcallister, "Multi-layer Thin-film EAS Marker," U.S. Patent 5083112, Jan. 21, 1992.

[Qua00] E. Quandt and A. Ludwig, "Magnetostrictive actuation in microsystems," *Sensors and Actuators a-Physical,* vol. 81, pp. 275-280, Apr 1 2000.

[Rud12] R.Q. Rudy, D.L, DeVoe, R. G. Polcawich, "Traveling Wave Ultrasonic Motor using Thin-film Piezoelectrics," presented at the *Solid-State Sensors, Actuators, and Microsystems Workshop*, Hilton Head Island, South Carolina, 2012.

[Sas85] T. Sashida, Motor device utilizing ultrasonic oscillation, U.S. Patent Number 4,562,374, December 1985.

[Sch01] S. Schmidt and C. A. Grimes, "Elastic modulus measurement of thin films coated onto magnetoelastic ribbons," *IEEE Transactions on Magnetics,* vol. 37, pp. 2731-2733, Jul 2001.

[Shc00] Shcheglov, K., Evans, C., Gutierrez, R., & Tang, T. K. (2000). Temperature dependent characteristics of the JPL silicon MEMS gyroscope. Paper presented at the *Aerospace Conference Proceedings*, 2000 IEEE.

[She10] W. Shen, L. C. Mathison, V. A. Petrenko, and B. A. Chin, "A pulse system for spectrum analysis of magnetoelastic biosensors," *Applied Physics Letters*, vol. 96, Apr 19 2010.

[So00] W.W. So and C.C. Lee, "Fluxless process of fabricating In-Au joints on copper substrates," *IEEE Transactions on Components and Packaging Technologies*, vol. 23, pp. 377-382, Jun 2000.

[Sto00] Stoyanov, P.G.; Grimes, C.A. A remote query magnetostrictive viscosity sensor. *Sens. Actuat. B Chem.* 2000, 80, 8-14.

[Sun02] Sun, D., Liu, J., & Ai, X. (2002). Modeling and performance evaluation of traveling-wave piezoelectric ultrasonic motors with analytical method. Sensors and Actuators A: Physical, 100(1), 84-93.

[Sun12] G. Sun, T. Liu, P. Sen, W. Shen, C. Gudeman, C.-J.Kim, "Electrostatically driven rotor on conductive liquid ring bearings," presented at the Solid-State Sensors, Actuators, and Microsystems Workshop, Hilton Head Island, South Carolina, 2012.

[Suz00] Y. Suzuki, K. Tani, and T. Sakuhara, "Development of a new type piezoelectric micromotor," *Sensors and Actuators a-Physical,* vol. 83, pp. 244-248, May 22 2000.

[Tri87] W. S. N. Trimmer and K. J. Gabriel, "Design Considerations for a Practical Electrostatic Micro-Motor," *Sensors and Actuators,* vol. 11, pp. 189-206, Mar 1987.

[Tai89] L.-S. F. Yu-Chong Tai, Richard S. Muller, "IC-processed micro-motors: design, technology, and testing," in *Micro Electro MEchanical Systems, 1989, proceedings, An Investigation of Micro Strctures, Sensors, Actuators, Machines and Robots. IEEE*, 1989, pp. 1-6.

[Tan13] Tang, J., Green, S. R., & Gianchandani, Y. B. (2013). "Miniature Wireless Magnetoelastic Resonant Motor With Frequency Selectable Bidirectional Rotation," *Journal of microelectromechanical systems*, 22(3), 730-738.

[Tan14] Tang, J., Green, S. R., & Gianchandani, Y. B. (2014). "Scalable, high-performance magnetoelastic tags using frame-suspended hexagonal resonators," *Journal of Micromechanics and Microengineering,* (Accepted).

[Tan08] E. L. Tan, B. D. Pereles, B. Horton, R. Shao, M. Zourob, and K. G. Ong, "Implantable Biosensors for Real-time Strain and Pressure Monitoring," *Sensors*, vol. 8, pp. 6396-6406, Oct 2008.

[Uch98] K. Uchino, "Piezoelectric ultrasonic motors: overview," *Smart Mater. Struct,* vol. 7, pp. 273-285, 1998.

[Uen10] T. Ueno, Z. G. Zhang, and T. Higuchi, "Translatory and Bending Micro Magnetostrictive Actuator using Iron-Gallium Alloys (Galfenol): A New Actuation Approach for Microrobots," *Advanced Robotics,* vol. 24, pp. 1423-1440, 2010.

[Vis13] A. Viswanath, S. R. Green, J. Kosel, and Y. B. Gianchandani, "Metglas-Elgiloy bi-layer, stent cell resonators for wireless monitoring of viscosity and mass loading," *Journal of Micromechanics and Microengineering*, vol. 23, pp. 025010-025019, Feb 2013.

[Waj08] D. Wajchman, K. C. Liu, J. Friend, and L. Yeo, "An ultrasonic piezoelectric motor utilizing axial-torsional coupling in a pretwisted non-circular cross-sectioned prismatic beam," *Ieee Transactions on Ultrasonics Ferroelectrics and Frequency Control,* vol. 55, pp. 832-840, Apr 2008.

[Wan07] L. Wang, "Vibration Energy Harvesting by Magnetostrictive Material for Powering Wireless Sensors," PhD. Thesis, 2007.

[Wat09] B. Watson, J. Friend, and L. Yeo, "Piezoelectric ultrasonic micro/milli-scale actuators," *Sensors and Actuators a-Physical,* vol. 152, pp. 219-233, Jun 18 2009.

[Wat10] B. Watson, J. Friend, and L. Yeo, "Modelling and testing of a piezoelectric ultrasonic micro-motor suitable for in vivo micro-robotic applications," *IEEE/AMSE Journal of Micromechanics and Microengineering,* vol. 20, Nov 2010.

[Yad98] Yazdi, N., Ayazi, F., & Najafi, K. (1998). Micromachined inertial sensors. *Proceedings of the IEEE*, 86(8), 1640-1659.

[Zen02] K. F. Zeng, K. G. Ong, C. Mungle, and C. A. Grimes, "Time domain characterization of oscillating sensors: Application of frequency counting to resonance frequency determination," *Review of Scientific Instruments*, vol. 73, pp. 4375-4380, Dec 2002.

[Zha08] Zhang, W.-M., Meng, G., Chen, D., Zhou, J.-B., & Chen, J.-Y. (2008). Nonlinear dynamics of a rub-impact micro-rotor system with scale-dependent friction model. Journal of Sound and Vibration, 309(3), 756-777.

[Zho09] N. J. Zhou, C. C. Blatchley, and C. C. Ibeh, "Design and construction of a novel rotary magnetostrictive motor," *Journal of Applied Physics,* vol. 105, Apr 1 2009.